Università degli Studi di Catania

Dottorato di Ricerca in Fisica – XXIII ciclo

LORENZO NERI

Time Resolved Single Photon Imaging Sensor with Single Photon Avalanche Diode

PhD Thesis

PhD Coordinator:
Prof. Francesco Riggi

Tutor:
Prof. Francesco Musumeci
INFN-LNS Tutor:
Dott. Salvatore Tudisco

Per diletto cerco i perché della Fisica,
Per fortuna ho trovato i perché della mia vita,
Valeria ed Alessio.

Contents

Introduction

The main topic of this work is the study of a new optical sensor with performances that will extend capability of new physical investigation techniques. Extreme detection efficiency was bring to the single photon sensibility, arriving time measurement was achieved with subnanosecond precision and the spatial recognition was obtained with two-dimensional integrated device. Maximum frame rate achievable is the single photon detection and no break is needed for device readout process.

These characteristics make the sensor, that we have studied, very attractive in several techniques which represent the state of the art of analysis methods, in solid Physics, Biology, and Astronomy. Fluorescence Lifetime Imaging Microscopy (FLIM)[1] is a functional imaging methodology that can provide information, not only concerning the localization of specific fluorophores, but also about the local fluorophores environment. It may be implemented in scanning confocal or multi-photon microscopes, or in wide-field microscopes and endoscopes. When applied to tissue autofluorescence, it reveals intrinsic excellent contrast between different types and states of the tissue. Nanosecond time domain, imaging, and extremely low light emission rate of environments investigated with this technique are exactly the scope of our sensor. Actually this technique is made with a single pixel sensor and to obtain an imaging a scanning procedure was used, with our sensor the imaging is a native characteristics that enable faster and more compact new setups. Many other investigation techniques, need same features, and for each of them our sensor is able to allow a step forward. Time Correlated Single Photon Counting (TCSPC)[2] is the base of FLIM but also many others exciting analysis technique like Dynamic Light Scattering analysis (DLS)[3], by which, for example, it is possible to determine dimension and

shape of particle in suspension and the interaction with the solvent[4]. Time precision reached with our device make also possible the implementation of 3D camera[5] in which the third dimension comes from the registration of the light reflection delay. High frame rate achievable with our imaging sensor enable fast transient analysis like Particle Imaging Velocimetry (PIV)[6] and Adaptive Optics (AO) [7], used in optical ground-based astronomy and space surveillance, to enable real time aberrations corrections, introduced by the atmospheric turbulence.

Our time resolved single photon imaging sensor is based on silicon semiconductor technology. Beyond the detection performance it takes advantages from many features that are intrinsic of the technology. First of all, is insensitive to magnetic field, requires a low voltage source and a low power source, benefits from miniaturization technology, is robust and shockproof, benefits from low cost fabrication process, and last but not least is at the same time sensible to the single photon and not damageable by any extremely high light intensity.

The research work performed and reported in this thesis has been absorbing and exciting, because all the aspects of the sensor developing have been studied.

In chapter 1 we have studied the physical characteristics, the sensing features and the noise suffering of the elementary sensing device of our sensor, the Single Photon Avalanche Diode (SPAD)[8]. We have continued, in chapter 2, the study of the single device by developing an electric characterization procedure and a electric simulation, studying different signal extraction techniques and testing two-dimensional electric configuration. Pushed by the objective to extend the counting range of the passive quenched SPAD, we have developed, in chapter 3, a simulation code and dedicated experimental measurement setups, to study the dynamic properties of sensor. Dead Time, detection efficiency, noise, and afterpulse, was studied to predict and correct their counting distortion. In the chapter 4 we explain one of the most relevant result obtained in this work, we was able to extend the dead time correction know in Literature over the steady state analysis to the time dependent source. The relevance of the obtained results, already published on “Sensors” journal[9], has been that they can be applied to all the device that are subjected to dead time and not only to the SPAD

devices. In the last chapter we have dealt with the high performance imaging topic, we have shown our personal solution in the two-dimensional SPAD configuration, we have described the imaging extraction procedure, and finally examined the peculiarity and the limits of our approach.

1. SPAD Device

The Single Photon Avalanche Diode (SPAD)[10] is the new generation of Geiger-Muller (G-M) detectors developed in semiconductor technology for photon counting measurement. This device enables the highest possible light sensitivity, that means the single photon sensitivity, the precise measure of the light time distribution also for very fast pulse and the possibility to achieve the correlation analysis of photons arrival time. In the last years many applications look to these features and SPAD development reach high level performance. Many products were already commercialized, and many applications were considered affordable for future SPAD technology. The imaging sensor studied in this PhD work is based on SPAD and in particular we used devices fabricated in Catania by the local STMicroelectronics R&D center. The aim of this chapter is an overview of SPAD device working principles, performance and technical characteristics, especially taking in account aspects concerning imaging sensor design. A deeper analysis of SPAD electric characteristics and features related to the imaging detector will be presented in the next chapter 2.

1.1 Junction Design and Avalanche Process

When a photon is absorbed inside a semiconductor an electron-hole pair is generated. If the photon is adsorbed inside a depletion region in which an electric field is present an electric field the electron and the hole drift according to their electric charge. This is the working principle of the photo-diodes, in which a big amount of photons are translated in an electric signal. To detect less pho-

tons, and at the extreme a single photon, a multiplication process should be activated. This is simply achievable in the semiconductor device increasing the applied electric field. If enough energy is provided to the free charges, the impact ionization can be enabled, and the electrons and the holes can extract other charges from the atoms of the material, multiplying their total number until a macroscopic electric signal is obtained. The impact ionization probability is strongly dependent from the electric filed inside the semiconductor, so can be finely and easily regulated with the voltage modulation. With such prescription high detection efficiency devices can be realized, the Avalanche Photon Diode (APD) and the Single Photon Avalanche Diode (SPAD). A specified junction design of the first type is the Separated Adsorption and Multiplication APD (SAM APD) shaped with a large depletion region followed by a multiplication region (Figure 1-1). This design is focused to reach high efficiency, due to the large adsorption region, and to a fine selection of the multiplication factor in the p doped region, in which there is generated the high electric field. Electric field trend is pointed out in the Figure 1-1. With this device it is possible to detect quite low photon flux because of the limited multiplication factor. The single photon detection is difficult, because of the large statistical fluctuation on the multiplication process.

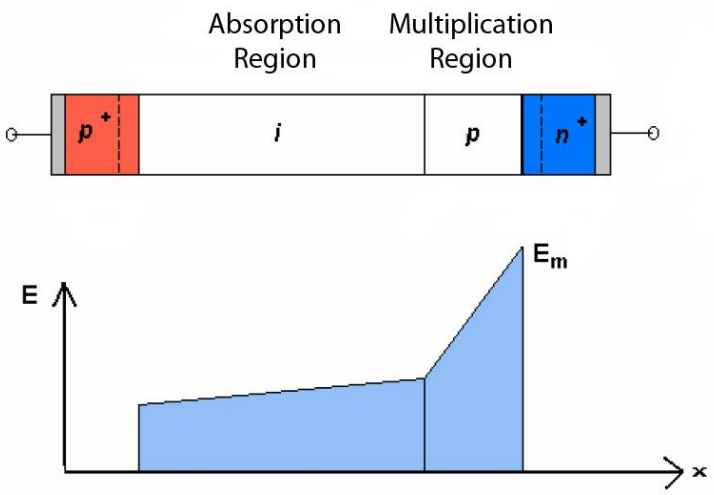

Figure 1-1: Junction scheme of SAM APD device and electric field generated inside the junction.

Typical multiplication factor ranges from hundreds to thousands of charges for each adsorbed photon. The produced signal follows the shape of the impinging photon flux.

The SPAD device is designed with an high doped p^+ n^+ junction, operating with a voltage 10% or 20% greater than the impact ionization potential. The junction SPAD design requires a special attention to prevent the early breakdown that could occur at the edge of the junction. In this region the peak effect generates an inhomogeneous electric field with peak values that make easier the generation of high noise rate production. The solution is to surround the depletion region with a n doped region to confine homogeneously the electric field (Figure 1-2).

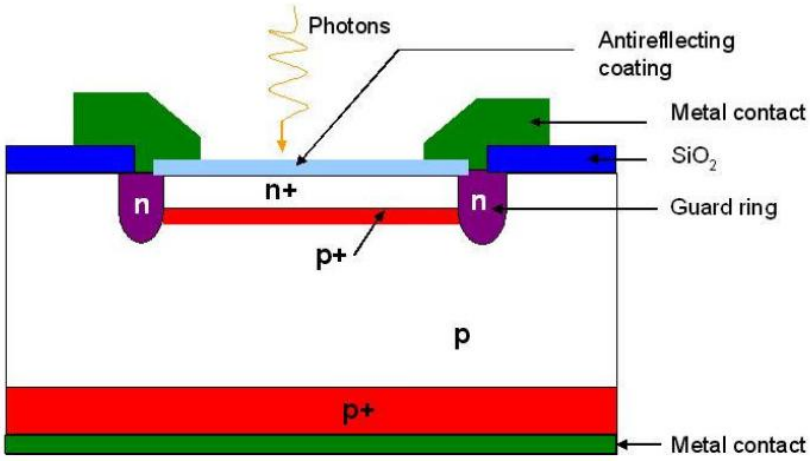

Figure 1-2: Junction scheme of SPAD device.

In SPAD device the adsorption area and the multiplication region are the same, in correspondence of the depletion region n^+ p^+. The sensitivity reach the single photon detection threshold with the overvoltage. The rapidity of impact ionization process produce a rapid growth of an electric signal that can be used as time information of the single photon adsorption event. Typically subnanosecond accuracy has been reached.

1.2 Voltage Supply and I-V Characteristic

The junction design used for the SPAD device (Figure 1-2) can be also used in APD mode by modulating the power source. The impact ionization multiplication factor, modulated by the applied voltage, varies with the shape, as shown in Figure 1-3. The impinging photon flux generates holes and electrons that, multiplied inside the junction, generate the current value showed in Figure 1-3. In the first part of the inverse polarization region, used for the photodiodes, the multiplication factor is zero and big amount of photon must be collected to produce an electric signal. Starting from a value called V_{APD} the single pair produced by photon is multiplied along its trip, the generated charge amount is collected by anode and cathode metal contacts. After the breakdown voltage V_B value the impact ionization probability guarantee that each charge that flows through the junction generates others charge. Each charge before the end of its trip produces a charge of opposite sign that must cross the whole junction in the opposite direction, and so it is subjected to another impact ionization, producing an endless process. This is the self-sustaining avalanche process that is active until the applied voltage is over the breakdown value V_B.

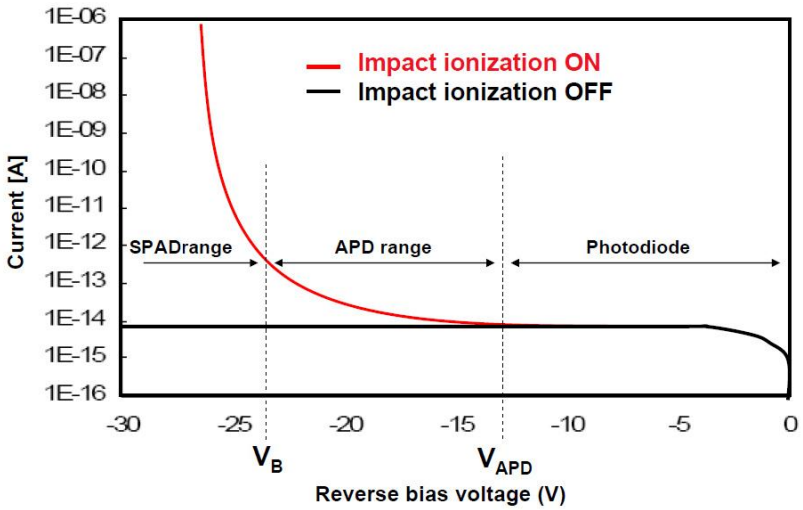

Figure 1-3: Typical multiplication regions of inverse polarized junction.

The SPAD device purpose is the single photon counting. By operating over the breakdown voltage the detection of a photon generates a self sustaining avalanche. In order to avoid the thermal junction destruction and to enable the following events detection it is necessary to lower the applied voltage after the generation of the signal, with the scope of quenching the avalanche, and, after that, recover the voltage to the initial state. This cycle is represented in the Figure 1-4 where A is the overvoltage condition without the avalanche, B is the current flowing point in the avalanche state, and C is the quenching of the avalanche state. This operating condition is called Geiger mode[11] because is the same of the Geiger-Muller counter device.

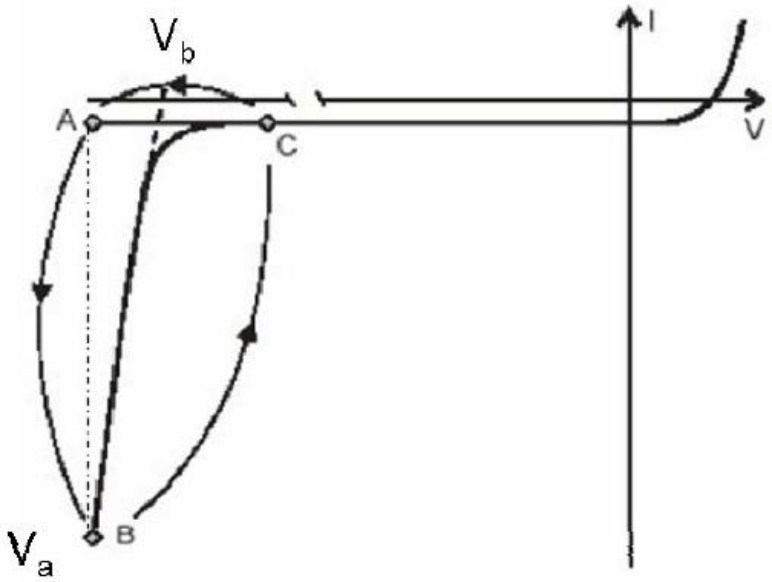

Figure 1-4: I-V characteristic of SPAD device operating in a Geiger mode.

1.3 Quenching Systems

There are two strategy for the quenching of SPAD, the use of a Passive Quenching Circuit (PQC)[12] or an Active Quenching Circuit (AQC)[13]. The PQC uses only one big resistor, while for AQC there are many possible approaches and also hybrid configuration with passive quenching and active reset.

In this presentation of quenching features we point the attention on PQC because in our imaging application we have bet on the advantages of using only one resistor quenching circuit. The feature used by the PQC (Figure 1-6A) is the voltage drop on a resistor crossed by a current. When the avalanche current flow across a big resistor, typically few hundred of kΩ (R_L in Figure 1-6A), the voltage applied to the diode decreases (voltage dropt, V_d in Figure 1-5). Accordingly the multiplication factor decreases and the outgoing current also decreases exponentially. If the voltage decreasing the multiplication factor becomes less than the self-sustaining value, the impact ionization becomes a non sure event and the avalanche quenching becomes probable.

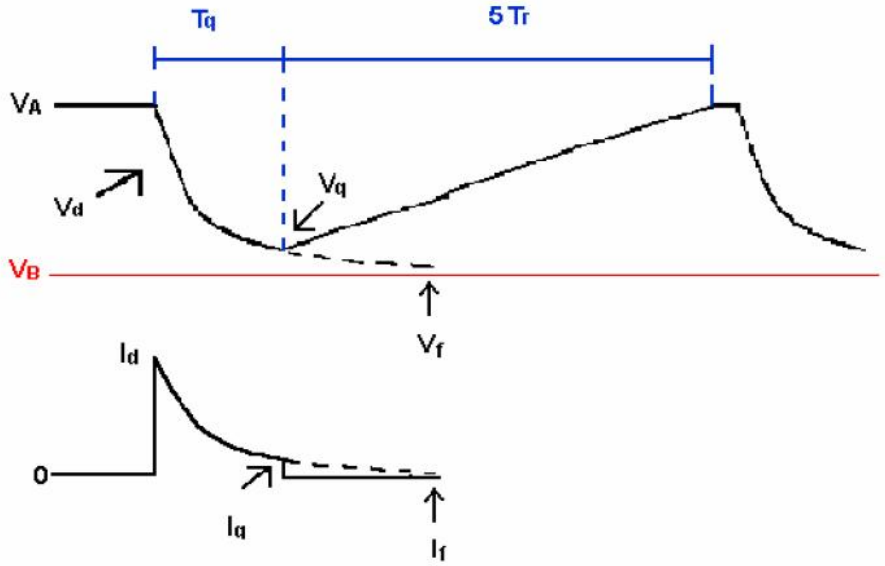

Figure 1-5: Voltage oscillation and current production during photon detection of SPAD device with PQC.

After the quenching of the avalanche the diode is brought back to a non conductive state. Starting from this point the diode and the stray capacitance (C_S in Figure 1-6B) were recharged with a charge that flows across the quenching resistor and the voltage is slowly restored to the initial value. The circuital scheme of the SPAD device was described by Cova[12] and reported in Figure 1-6B. Detailed electric analysis of the SPAD device will be discussed in chapter 3.

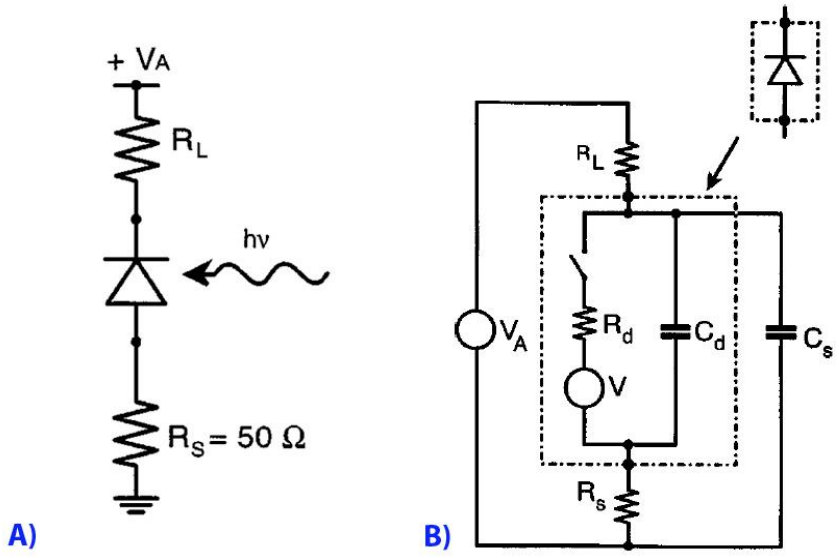

Figure 1-6: A) Passive Quenching Circuit. B) PQC SPAD equivalent circuit.

The basic idea of the AQC was simply to sense the rise of the avalanche pulse and reach back on the SPAD, forcing, with a controlled bias-voltage source, the quenching and the reset transitions in a short time. The fast transition was achieved to reduced losses in photon counting. Typical time reached by AQC was about 40 ns. However, the faster is the performance pursued, the higher is the impact of afterpulse effect[15], which will be discussed in the next section, which has typical time constant of hundred of nanosecond.

1.4 Afterpulse

The defects in the semiconductor material or the damages caused by fabrication process (ion implantation, diffusion, etc.) insert energetic levels inside the band structure of the semiconductor. Due to their low population, below the saturation, the levels located in the center of the gap act as trapping centers[16], that during the avalanche process collect electrons. Unfortunately the lifetime of these energetic levels cannot be regulated, typical values are from some tens to hundreds of nanosecond. If an electron is released when the SPAD biases vol-

tage is over the breakdown value an avalanche is triggered and a noise event is generated. The biggest disadvantage of such type of noise is the time correlation with real events. In a device made to enable correlation analysis all the sources of correlated noise should be reduced as possible.

In AQC devices the rapid replacement of the initial voltage state enables the detection of most part of the released electrons. So in AQC devices the amount of trapped electrons must be minimized, and this is done with the reduction of the avalanche charge that flows during the detection pulse. Afterpulses that characterize fast AQC device are typical more than 10%. It is also unavoidable that on increasing the AQC rapidity the detected afterpulse rate exponentially increases[14].

In devices with PQC the time needed to recover the initial voltage is of the order of microseconds or less and the afterpulse probability is very low. Even if a big amount of charges is produced during the avalanche, and some of them are trapped, the largest number is released during a non sensitive time, without producing any effects on the SPAD count.

In our device we have used PQC configuration with low afterpulse production, but due to the relevance of correlated noise into a correlation detector we developed a detailed afterpulse analysis described in section 3.5. Our SPAD characterization is focused on the realization of a imaging device, so the photon rate dependence has been deeply studied. We found that afterpulse counts decrease on increasing the photon rate. In the experimental data shown in Figure 1-7 the maximum afterpulse probability is around 3,5% before 8 Kcps and afterwards decreases until reach zero in correspondence to 50 Kcps. This reduction is generated by the increase of the number of true events that trigger the diode before the afterpulse events generation.

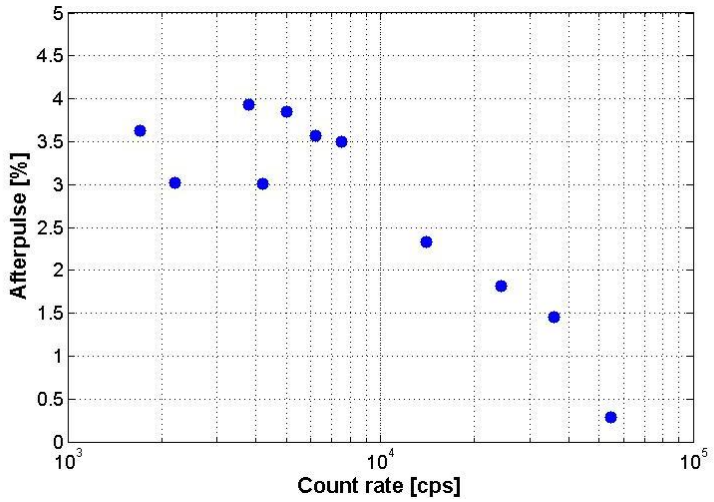

Figure 1-7: Afterpulse probability vs impinging photon count rate.

A further parameter that influences the measured afterpulse count, for SPAD device in PQC configuration, is the threshold level. For this system the afterpulse is generated during all the recharge state, even if the only pulses that exceed the threshold value are counted by the acquisition system. The histogram in Figure 1-8 shows the second pulse correlation in dark condition, measured by a digital oscilloscope. The histogram reports the delay between the first event and the following events that overcome the threshold level, like in real acquisition system. With a trigger level of -1,9 mV the histogram starts from 600 ns, while can be easily seen that the generation of new signals starts before. So, on changing the trigger level, the amount of collected second signals changes. Due to the dark condition, the total amount of collected delays are caused not only by afterpulse, but they are mixed with the dark noise production. In fact dark noise production follows the Poissonian distribution, and the delay between events shows an exponential distribution with a time constant more close to the afterpulse distribution. Inside the “Measure” box of the digital oscilloscope Figure 1-8 the mean of the P2:edge measurement shows a value of 1.09 , from this value 9% of second pulse inside the nine following microseconds can be deduced, and this is not only the afterpulse contribute, but the sum of afterpulse and the second random Poissonian dark noise.

1.4 Afterpulse

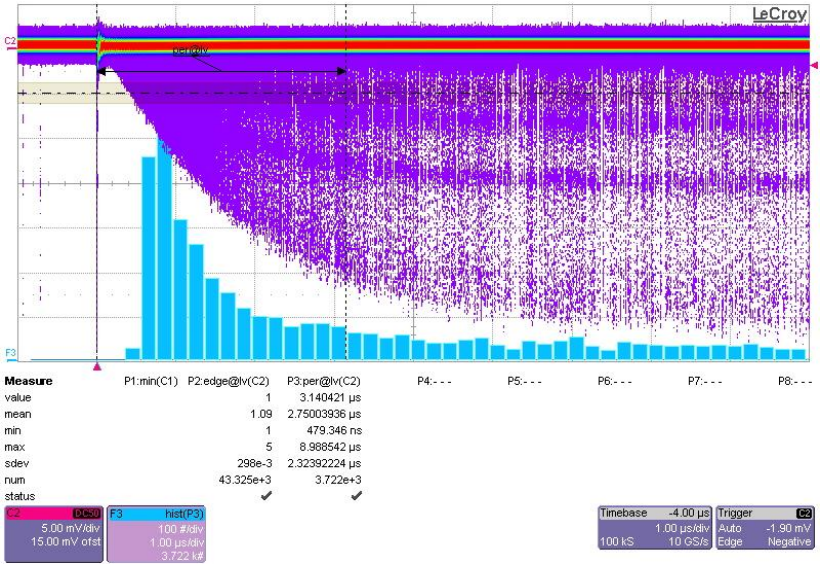

Figure 1-8: Digital Oscilloscope image in persistent mode with afterpulse measurement mode.

In conclusion, on increasing the threshold level, that means an increase of sensor dead time (DT), we obtain a desirable reduction in afterpulse measurement, but also a loss of true events. So the selection of the good threshold level should be taken into account the recharge process and the afterpulse production.

Another important parameter that modifies the afterpulse production is the temperature of the diode. Usually, to reduce the thermal noise of silicon device the temperature is lowered: usually a temperature of -20°C is considered in high sensitivity CCD camera. In Figure 1-9 the time distribution of the afterpulse probability is shown for three different temperature, 25°C, 20°C and 15°C. The insert of Figure 1-9 shows that the slope of the afterpulse probability linearly decreases on decreasing the temperature. Taking into account that the temperature variation is of only 10°C, the slope trend clearly shows that at -20°C the SPAD cannot be used because with such lower temperature the largest amount of afterpulse overcome the dead time of the device. Due to this consideration the selection of the SPAD working temperature must be chosen taking in account afterpulse and noise thermal characteristics.

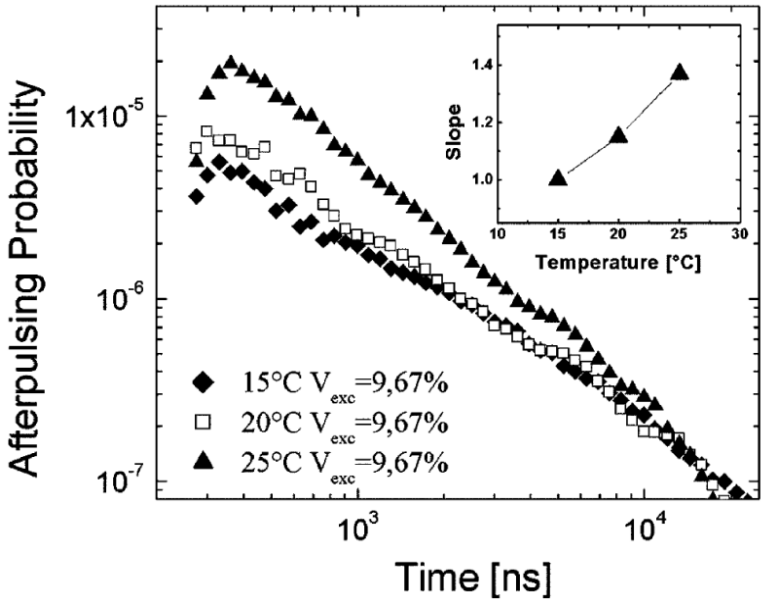

Figure 1-9: Afterpulse time distribution for three different diode temperatures.

1.5 Recharge and Dead Time

In all counting device after the detection of an event it follows a time in which the device is not able to generate another count, this is called Dead Time (DT). There are two elementary idealized models of DT, named paralyzable (P-DT) and non paralyzable (NP-DT). In the P-DT case all events occurring during the DT are not registered, but are able to prolong the period during which the detector is not able to reveal further signals. In the NP-DT case, any event arriving during the DT is neither registered nor has any influence on the device. In the real equipments parallel or series combinations of these two kinds of DT can be found.

For SPAD with AQC the DT is a fixed interval in which the impinging photons are not collected nor produce any effects. The duration of this interval is well defined with the circuital design of the AQC system. In PQC SPAD the DT is a combination of the two DT types, and the incoming events can generate effects even if they don’t generate counts.

The avalanche process is a statistic process, the height of produced signal is strongly dependent from the overvoltage value, but it is also subjected to an intrinsic random fluctuation of the avalanche generation process. During the recharge of the diode the overvoltage grows according to a classical exponential trend of a resistor-capacitor recharge process. The amplitude of produced signal, that is linearly dependent from the overvoltage, follows this trend. According to the known shape of the recharge process, a fixed delay value necessary to obtain a signal that overcomes the threshold can be calculated. However the avalanche statistic fluctuation generates events that are detected earlier than predicted and loses events with time distant more than necessary. The fluctuation is not great compared with the total DT duration, but must be considered in the discussion. This is the reason of the first non zero value of the delay histogram in Figure 1-8. Another but more important effect of PQC SPAD is the production of non detected signals during the DT. In the Figure 1-8 it is clearly shown the high production rate of signals of amplitude lower than the threshold of the electronics. This signals do not produce counts but produces the restarting of the DT period, that means changes in the detection efficiency of the device. As described above the afterpulse losses inside the DT partially solve the problem of afterpulse phenomena, while the lost true events will be taken into account in the detailed DT analysis of chapter 3.

1.6 Dark Noise

In a SPAD device the primary noise source is the thermal assisted transition of an electron from the valence to the conduction band, that can be also seen like an hole production in the valence band. Both electron and hole can trigger an avalanche and so a signal can be produced, and unfortunately this signal cannot be distinguished from those produced by a photon. This noise is commonly called dark noise.

The electron and hole excitation mainly depends on the energy gap and on the temperature by the Arrhenius exponential factor $e^{\left(-\Delta E/KT\right)}$. So the working temperature dominates the transition rate, and precise working temperature con-

trol must be implemented in SPAD sensors. Lowering the temperature reduces the thermal noise, but like showed previously (section 1.4) the temperature can be reduced until the afterpulse production remains below an acceptable level. The transition is also dominated by the concentration of crystallographic defect, that inserts shallow levels inside the gap. Such levels enable a two step transition (Figure 1-10) that is more probable of direct transition. So crystallographic defect become the most important source of noise, and fabrication technique should be addressed to reduce defect implantation.

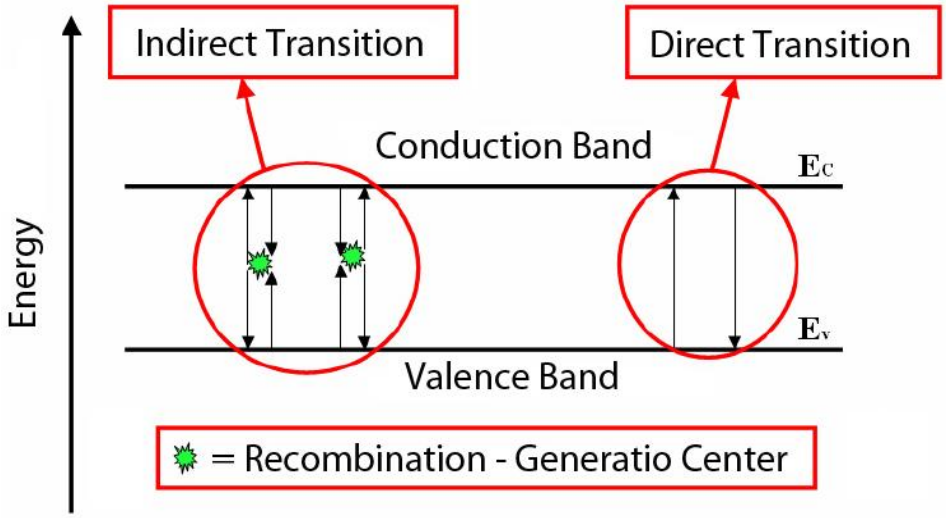

Figure 1-10: Transition mechanisms of dark noise production.

It is important to note that the generation of a free pair inside the junction is a fundamental requirement for the noise production, as much as, the voltage applied to the diode. Without enough voltage a free pair cannot be transformed into an avalanche and no noise signal is produced. So in the first part of the recharge process the lower voltage state inhibits the noise production. The overvoltage represents an avalanche efficiency that convert a single free pair into an avalanche. If the free pair comes from a thermal excitation we have a noise event, while if the pair comes from a photon adsorption we have a detection event. So the photon detection efficiency and the noise rate production are two strongly connected phenomena.

As it will be described in section 5.1 there are two main approaches to design imaging device with SPAD technology, the first is the use of the smallest number of fabrication process optimized for SPAD device performances, the second is the use of CMOS technology that offers the possibility to merge SPAD design and complex electronics circuit facilities. Many performances can be increased with a dedicated technology development, first of all the dark count production that, as showed, is extremely dependent from the number and the type of the processes used in the fabrication. Our time resolved single photon imaging device approach is based on simplified SPAD fabrication. To use the higher performance enabled by this approach, all the needed acquisition electronic is designed outside the sensitive device.

1.7 Secondary Photons

During the avalanche process each ionization impact causes high deceleration in electron drift, so the Bremsstrahlung process enables a secondary photons production inside the junction. Due to the high photon sensitivity of SPAD device the diffusion of these secondary photons must be controlled, and especially in array configuration. This photons production is contextual to the avalanche process so inside the diode don't introduce delayed pulse as in the case of trapping phenomena. However the travelling photons outside the junction can externally reflected and can generate delayed afterpulses if they are reflected back to the diode. In the device fabrication an antireflection coating layer is often added to prevent the photons emission outside the semiconductor device (Figure 1-2). Inside the STMicroelectronics fabrication process two antireflective layer were implemented, one made with silicon oxide and the other with silicon nitride. Before of the deposition of these thin films the photons production is used, as fabrication check, to identify the avalanche spread along the diode surface. Figure 1-11 shows the images obtained by an Emission Microscope (EM), when different reverse currents flow through an avalanching junction. The images concern one of the diodes of the 10×10 SPAD array that will be discussed later in the chapter 5. The array was kept in dark condition, while the junction of the pixel

(1,1) was forced above breakdown at different excess biases, biasing the first anode row and cathode column. As it can be seen from the Figure 1-11, the breakdown is spatially uniform over all the active area, so excluding the possibility to have an edge breakdown fabrication defect. The different photons production for the two overvoltage values represent the different amount of avalanche charge produced.

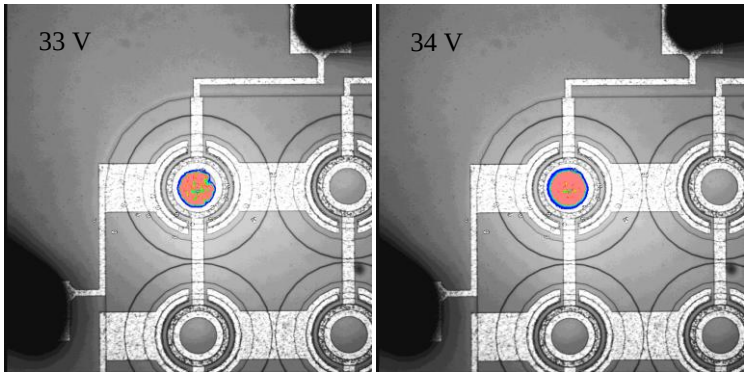

Figure 1-11: Emission microscope pictures showing the avalanche turn-on in a pixel of 10×10 SPAD array at increasing overvoltage. Red means high, green lower, and blue lowest emission region.

1.8 Cross Talk

The downside of the high detection sensitivity of SPAD device is the cross talk between diode in array configuration. Actually the SPAD devices have a photon detection sensitivity of about 30% in the visible range, and 100% efficiency for free electron that travels in the biased junction. Two types of cross talk can occur between SPADs in array configuration, the optical and electric cross talk. For imaging application (chapter 5) or in Silicon Photon Multipliers application (SiPM)[17]-[18], many diodes have been putted the nearest possible to maximize the fill factor and the detection efficiency. On the other hand cross talk probability grows with SPAD density. Cross talk as afterpulse is a correlated noise, afterpulse is a time correlated while cross talk is a spatial correlated noise. In the imaging application the cross talk noise reduces the resolution with an out-of focus effect. Also in SiPM configuration, that do not require any spatial

resolution, cross talk correlation activates neighboring pixels causing the degradation in the numerical determination of fired SPADs, so reducing the whole energy resolution of the device.

The optical cross talk is activated by the emission of secondary photons, that can travel along the silicon bulk, transparent to the optical wavelength, and cross another diode that is triggering a correlated avalanche (Figure 1-12). The time delay between the two produced signals is less than the measurable one and induced signals cannot be distinguished from the generated one.

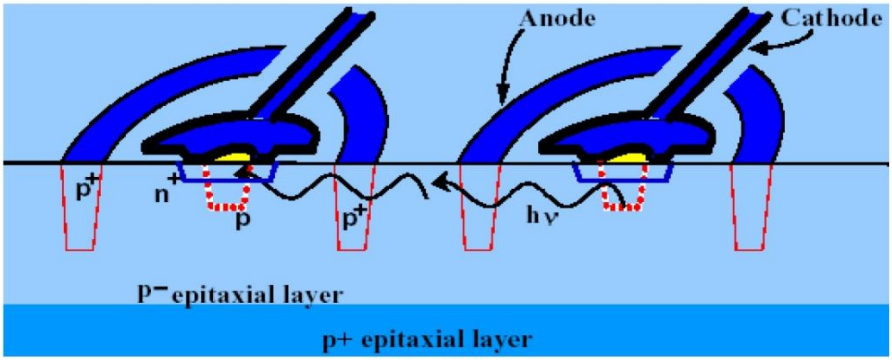

Figure 1-12: Optical cross talk between SPAD diode in array configuration.

A further contribute to the optical cross talk was found[19] in the indirect optical pat (Figure 1-13) enabled by the optical reflection by the back part of the device.

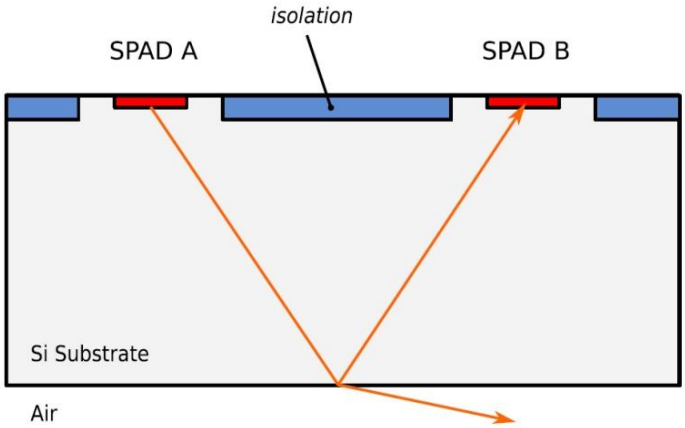

Figure 1-13: Optical indirect crosstalk assisted by back reflection.

The electric cross talk is activated by the electron current that travels, during the avalanche, along all the anode metallization of the device. In a matrix configuration the anode is shared between many diodes and the current flows near each diode junctions (see Figure 1-14).

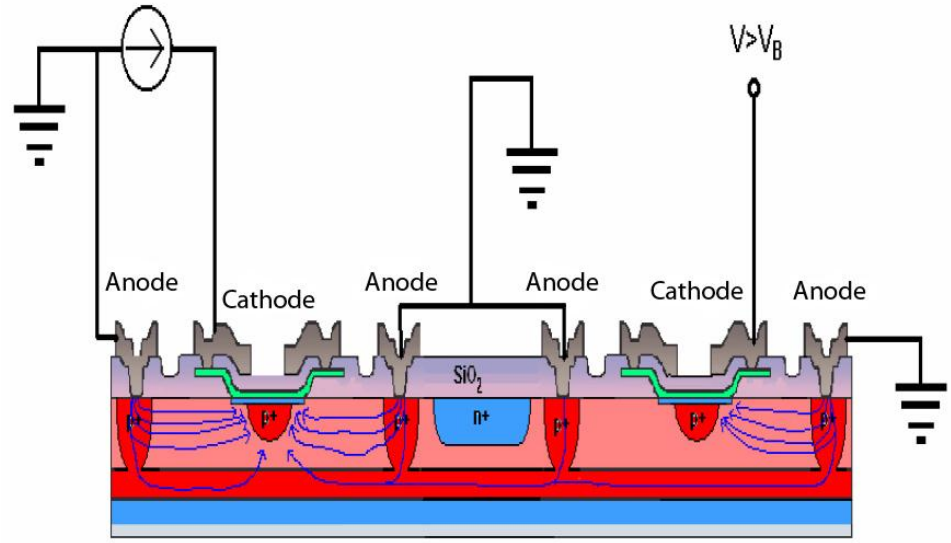

Figure 1-14: Electrical cross talk.

The possibility that an electron can be collected by the biased cathode of another diode is very small, but, due to the high number of electrons, and the high detection efficiency of the other diodes, the electrical cross talk possibility can be significant. In addition the efforts in order to increase the fill factor, reducing the space between diodes, bring to a relevant optical and electric cross talk.

In order to study the reduction of the optical and electrical cross-talk contribution, arrays that are optically and electrically isolated by deep thin trench technology have been already designed and fabricated in Catania R&D group of STMicroelectronics. The developed trench process starts with a vertical etch 10 μm deep and 1 μm large and a subsequent oxide deposition for complete electrical isolation. Then the process continues with tungsten filling, to avoid optical cross-talk, and ends with planarization. The optical trench is showed in the left and right boundary of the Figure 1-15.

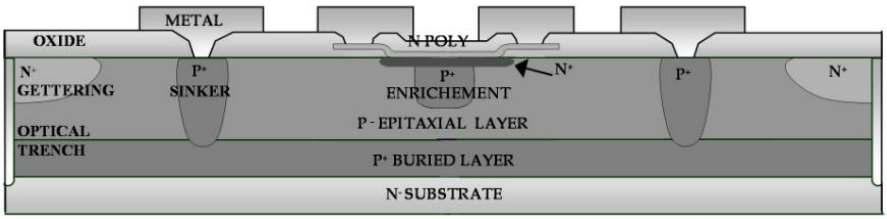

Figure 1-15: Schematic cross-section STMicroelectronics SPAD single pixel.

1.9 Photon Detection Efficiency

Silicon band gap is 1,12 eV. This energy corresponds to a photon with a wavelength of 1100 nm. This is one of the boundary in the wavelength domain of the photons that can be detected by silicon device, SPAD included. The photon detection efficiency is modulated in wavelength by the absorption coefficient of light in silicon, and also by depends the junction dimension, the overvoltage value and the diode temperature. The photon detection efficiency (PDE) of a SPAD device is given by the probability that a photon crosses the first part of the semiconductor device without being adsorbed, multiplied by the adsorption probability inside the active region. The adsorption probability in a layer of thickness *dx* at depth *x* is:

$P(x)dx = \exp(-\alpha x)\cdot \alpha dx$	1-1

where α is the absorption coefficient. In silicon this parameter varies with the photon wavelength as shown in Figure 1-16.

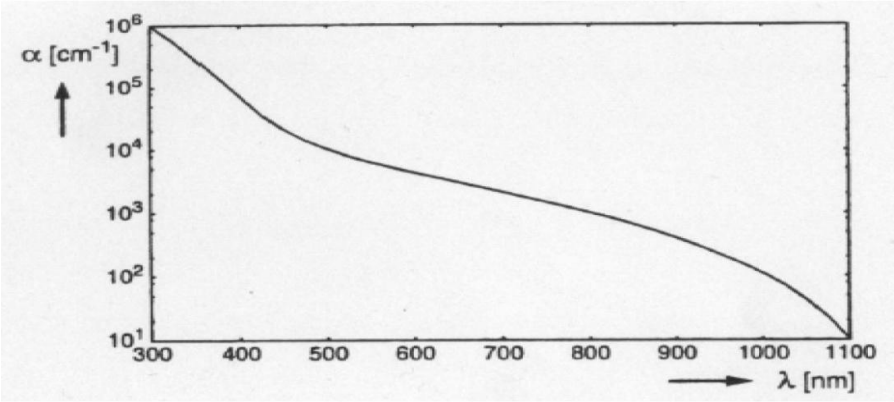

Figure 1-16: Adsorption coefficient of Silicon versus photon wave length.

The resultant PDE (Figure 1-17) takes in account that, for high energy photons, the adsorption coefficient is so big that a photon is adsorbed before the junction active region, while, for low energy photons, the probability to travel without adsorption in depth of the active region grows. The other parameters that affects the PDE of the device are not sensitive to the photon wavelength, but give only a quantitative contribute. As a result of the foregoing the thickness of the active region (the depletion region) is an important efficiency parameter. Increasing the applied voltage increases the probability to start the avalanche process and so the detection probability. Figure 1-17 shows the PDE of a SPAD device measured[17] for different photon wavelengths and for different overvoltage values. On increasing the overvoltage more than 20% the PDE do not increase linearly but reach a saturation level in which the avalanche process becomes certain and a further increase do not produce any detection improvements. The PDE also shows a little dependence correlated to the working temperature of the device because of the little temperature dependence of the semiconductor bang gap, that was reduced increasing with the increase of the temperature.

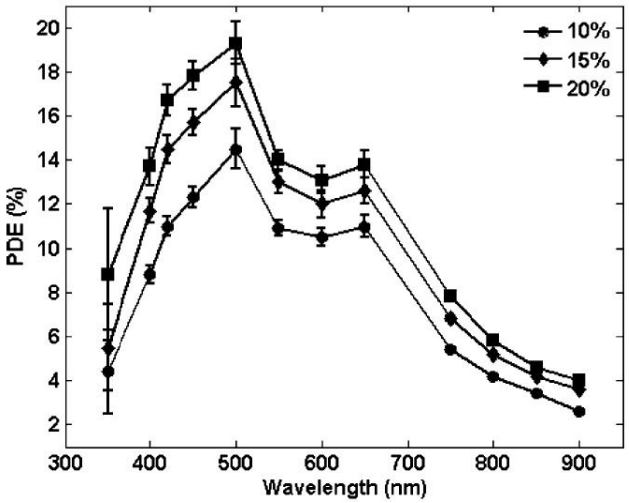

Figure 1-17: Photon Detection Efficiency of SPAD device, for different wave length and different overvoltage values.

2. SPAD Electric Simulation

The study of SPAD electric characteristics is fundamental to design two-dimensional array and its readout systems. In our work we develop a new readout approach that minimize the number of readout channels. We need to understand the influence of diode electric characteristics on the shaping of the output signal, the realization of two readout signals for each SPAD, and the cross influence between the diodes in the two-dimensional array configuration.

2.1 Electric SPAD Model

The SPAD electric model was deeply studied by Franco Cova[12], to develop fast active quenching circuit technology. We start from what published by Cova, shown in Figure 2-1A, to design a code for the SPAD electric simulation (Figure 2-1B). The PSpice[20] software suite was used. The simplest SPAD working configuration, the Passive Quenching Circuit (PQC), was used for the electric characteristics of diode electric components. With such basic configuration we are able to compare simulation and measurement and extract the influence of each electric components of the diode, that represent the electric aspects of the diode.

The charge separation inside the junction during the inverse polarization was simulated with the charge accumulated inside the capacitor C_d, where “d” means diode, the resistor R_d represents the junction semiconductor resistivity during the

avalanche process, and the breakdown voltage source V, with same polarity direction of the external power source, represents the voltage loss that do not take effect on the conduction mechanism. The avalanche process is equivalent to the "on" state of a switch, triggered by the photon adsorption, while the "off" state is before the adsorption and after the quenching of the avalanche. Single switch configuration used by Cova needs a complex code programming of a new PSpice switch components. To simplify the programming we selected, inside the PSpice library packs, two switches shown in Figure 2-1B, one that closes and the other opens the circuit. Both switches can be programmed with the time when their transition must occur. The others electric elements required for this configuration are the stray capacitance C_s, the quenching resistor R_L, the applied voltage V_A, and the sensing resistor R_s.

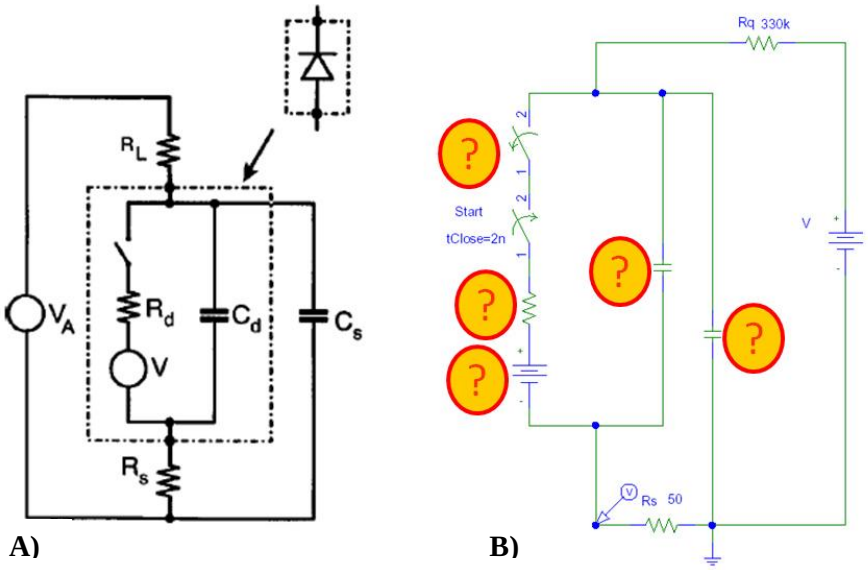

Figure 2-1: Electric SPAD model: A) proposed by Cova; B) used for our simulation inside PSpice programming suite.

While the value of the external quenching resistor, the applied voltage and the equivalent resistance of the readout electronic are well known, others values of the diode's components and the stray capacitance must be evaluated. In Figure 2-1B there are many question marks as the number of unknown value para-

meters. The transition time of the first switch, that closes the circuit, is not an important parameter because this time represents the photon adsorption, namely the zero time reference, and can be freely chosen. Differently the time transition parameter of the second switch, that represents the end of the avalanche quenching process, must be estimated. This parameter is connected to the end of the output signal and to the start of the recharge process.

Using the electric simulation program we can reproduce the output signal of the system, but, more importantly, we can understand how the SPAD circuit works, which are the reciprocal influences of its components, and then how the readout system can be designed to achieve our requirements.

When avalanche process closes the first switch three loops are closed, each one is shown in the Figure 2-2 with a different image. The three closed circuit share the left branch of the diode, composed by the two switches, the diode resistor and the breakdown voltage supply. The more external loop, Figure 2-2A, is composed by the common branch, the quenching resistor, the external voltage source, and the sensing resistor. Due to the high resistivity of this closed circuit the current that flows in correspondence of the avalanche start is some micro Ampere, and the signal that is produced in the sensing resistor is negligible. Also the diode internal loop (Figure 2-2C), that do not include the sensing resistor, is not the cause of the output signal. The source of the output signal is the loop that includes the stray capacitance (Figure 2-2B). When the avalanche closes the circuit the capacitance is discharged and a signal is produced across the sensing resistor. In this occasion the stray capacitance is not an unwanted effect but a fundamental element for the signal production. An important thing to underline is that the sensing loop (B) have the same characteristics of the diode internal loop (C). The total resistivity of the two loops are practically the same, because the internal resistor is some thousand of ohm as order of magnitude and the sensing resistor is 50 ohm. The two capacitance are also of the same order of magnitude. This similarities means that with such sensing configuration we are able to evaluate the current pulse shape that flows inside the diode.

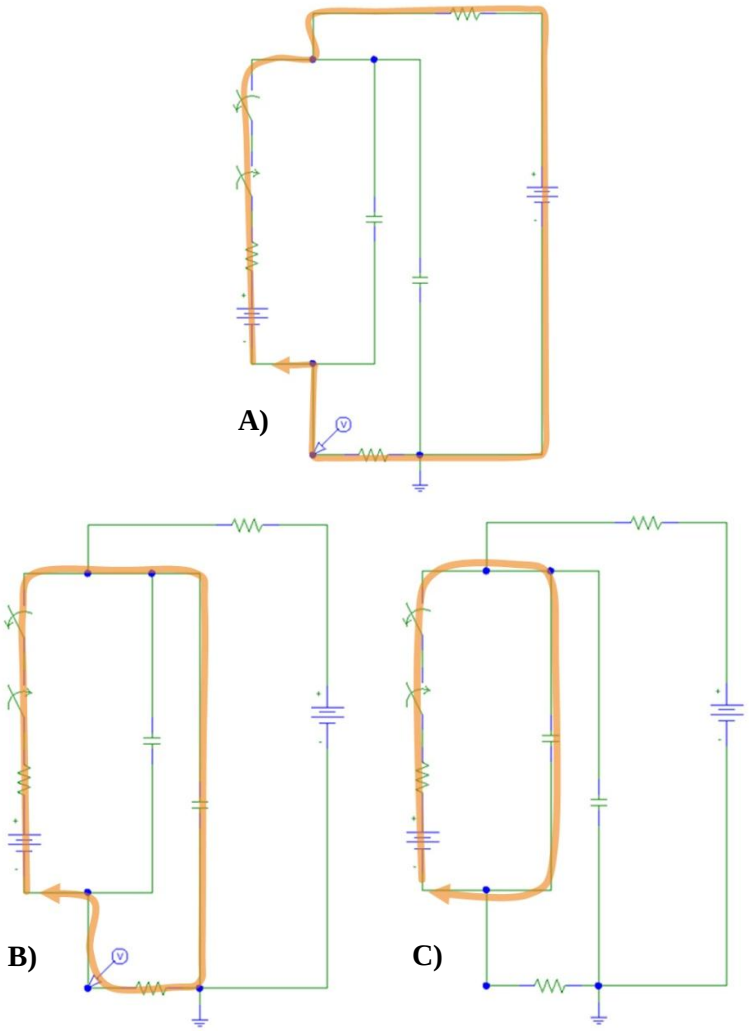

Figure 2-2: The three circuits closed during the avalanche conductive state: A) external circuit with voltage source and quenching resistor; B) circuit activated by the stray capacitance; C) circuit inside the SPAD diode.

After this quantitative analysis of the PQC SPAD circuit we proceed to a calibration procedure that make we able to know the electric parameter of our real device. The results will be used in the simulation of real environment and to design the new readout strategy for two- dimensional array configuration.

2.2 Calibration Measurements

The experimental configuration used for the measurement of diode electric characteristics is exactly what reported in Figure 2-1B. The sensing resistor is a digital oscilloscope with input impedance of 50 ohm. The choice of digital oscilloscope has been done for the multitude of measurement that can be simply done in real time and with statistic features (mean, standard deviation, numbers of events, etc.).

The first performed measurement was the total charge produced at different power source values. The voltage integrated along the time divided by the sensing resistor value gives the total charge of the system.

$$\frac{Area[V \cdot s]}{50[\Omega]} = [A \cdot s] = Q[Coulomb] \qquad 2\text{-}1$$

The Figure 2-3 shows that, as expected, the total accumulated charge linearly increases with the applied voltage. The equation that describe the system is:

$$Q = C_{tot} * (V - V_B) \qquad 2\text{-}2$$

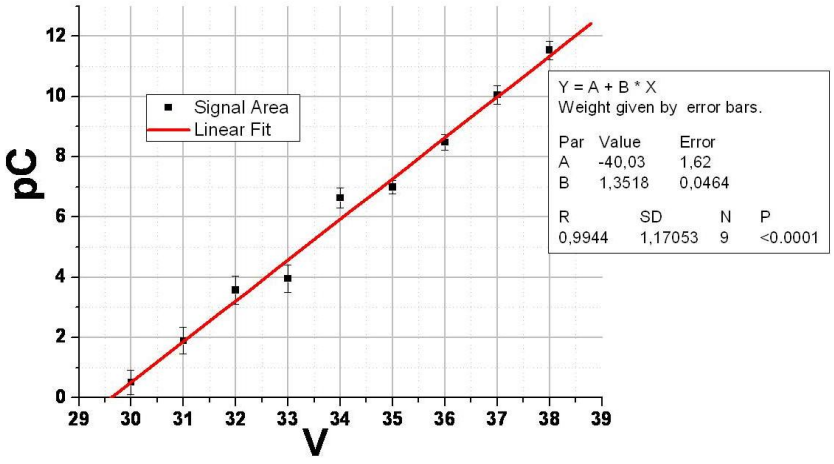

Figure 2-3: Charge pulse versus power voltage.

From the linear fit of experimental data we can obtain total capacitance of the system and the breakdown voltage of the diode. In the equation used for the fit Y is the total charge Q, B is the total capacitance of the system C_{tot}, and A is

the product of C_{tot} and the breakdown value sign inverted. We can obtain:

$$B = C_{tot} = 1{,}35 \pm 0{,}05[pF]$$
$$-A/B = V_B = 29{,}6 \pm 1{,}6[V] \qquad 2\text{-}3$$

The second step in the calibration procedure was the internal resistance determination. In the Figure 2-4 the quenching part of a measured signal was selected. The exponential equation shown inside the box of Figure 2-4 was used to extract the decay time constant of the closed circuit of Figure 2-2B. Using the total capacitance value of 2-3 it is possible to extract the internal resistance of the diode.

$$P3 = T = R_d * C_{tot} \qquad 2\text{-}4$$

Even if we know the sensing resistor value we can neglect this contribute because it is two order of magnitude smaller than the diode resistance and we are not sensitive to a so small value, that is inside in the experimental error.

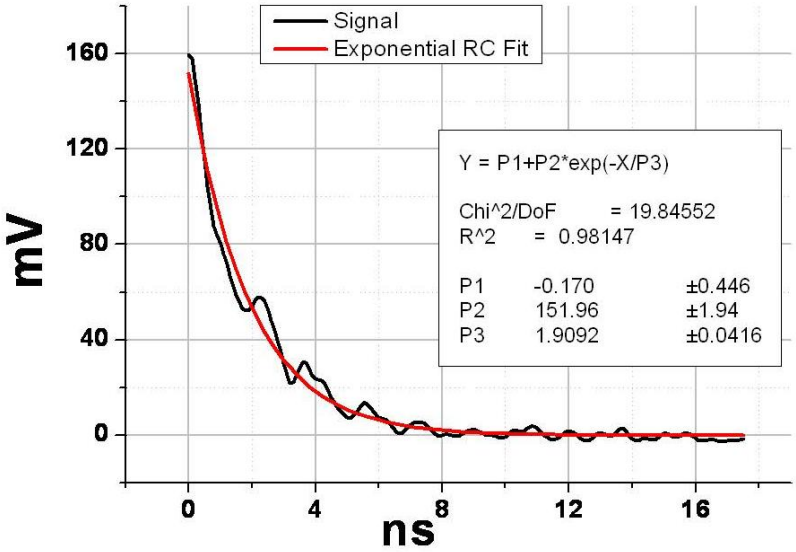

Figure 2-4: Fit of pulse quenching shape.

The trend of the diode resistance, measured for various applied voltages, is noteworthy as shown in Figure 2-5. It appears that, for overvoltage values lower than 15% of the breakdown voltage, the junction is not fully activated and the

resistance is greater than the constant value reached after 34 Volt. Starting from this consideration the internal diode resistance value can be calculated as the average of the last four points of Figure 2-5, being the result:

$$R_d = T / C_{tot} = 1{,}42 \pm 0{,}07[K\Omega] \qquad 2\text{-}5$$

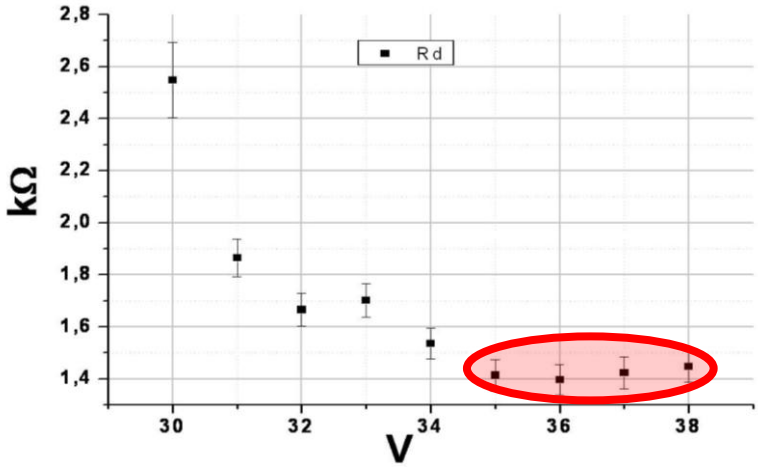

Figure 2-5: Measured diode internal resistance at various power voltages.

To evaluate the stray and diode contribute to the total capacitance we use the equation proposed by Cova in [12]:

$$V_s \cong V_E \frac{R_s}{R_d\left(1+\frac{C_d}{C_s}\right)} \qquad 2\text{-}6$$

This equation allows to calculate the maximum voltage amplitude of output signal V_s as function of diode and sensing resistors, stray and diode capacitances, and overvoltage vales V_E=V-V_B. From Eq. 2-6, and by approximating the capacitance configuration like a parallel connection, that means by neglecting the sensing resistor contribution, we can evaluate the equation of the stray capacitance:

$$C_s \cong \frac{V_s}{V_E}\frac{R_d}{R_s}C_{tot} \qquad 2\text{-}7$$

These equations show that the output maximum signal V_s is linearly dependent from applied overvoltage V_E. This dependence is clearly shown in Figure

2-6. With the fit of experimental data plotted in Figure 2-6 we estimate the ratio V_s/V_E. Due to the fact that the threshold for the production of an output signal is V_E equal to V_b, the intersection with the horizontal axis is the breakdown voltage value.

$$B = V_s / V_E = 29{,}7 \pm 1{,}5$$
$$-A/B = V_B = 30 \pm 2[V] \qquad 2\text{-}8$$

Even if the error in both measurement of the breakdown voltage shows a big uncertainty, the difference between the two values is four time smaller than the lowest measurement error.

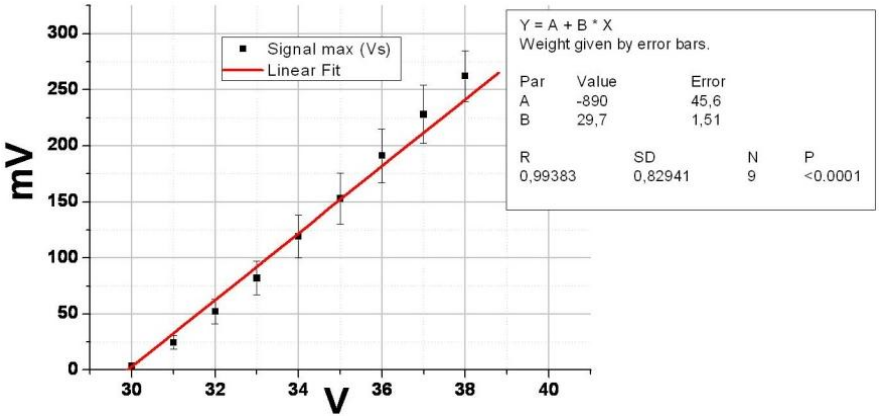

Figure 2-6: Pulse amplitude versus power voltage.

Using Eq. 2-8 into Eq. 2-7 we obtain the stray and diode capacitance values:

$$C_d = 0{,}21 \pm 0{,}09[pF]$$
$$C_s = 1{,}14 \pm 0{,}09[pF] \qquad 2\text{-}9$$

The last unknown parameter of the system is the quenching process duration, represented by the time interval between the two transition of the two switch in Figure 2-1. This parameter do not have any influence on the signal production, but only achieves the truncation of the signal when it is practically zero, and triggers the start of the recharge of the system. So this value will be evaluated after the simulation of the output electric signal, pointing the time in which the current decreases below the latching current[12], when the overvoltage cannot ensure the avalanche process (section 1.3).

2.3 PQC with Ground on Cathode

The PQC readout configuration is made with a sensing resistor on one side of the diode and the quenching resistor on the other side. The ground is commonly pointed on the sensing resistor, to obtain signal on a base level equal to zero. Repeating the calibration procedure with the inverse configuration, with the quenching resistor on anode and sensing resistor on cathode, we obtain different results that justify the different configuration shown in Figure 2-7. The reason of these differences is intrinsic of stray capacitance definition. Named the capacitance characteristic of a point to ground. In correspondence of the anode and the cathode of the diode we must consider two points that show capacitance characteristic toward the ground. On changing the ground configuration the stray capacitance connections and the capacitances configuration and values change, because the ground is moved to another position and, because the layers materials to ground change.

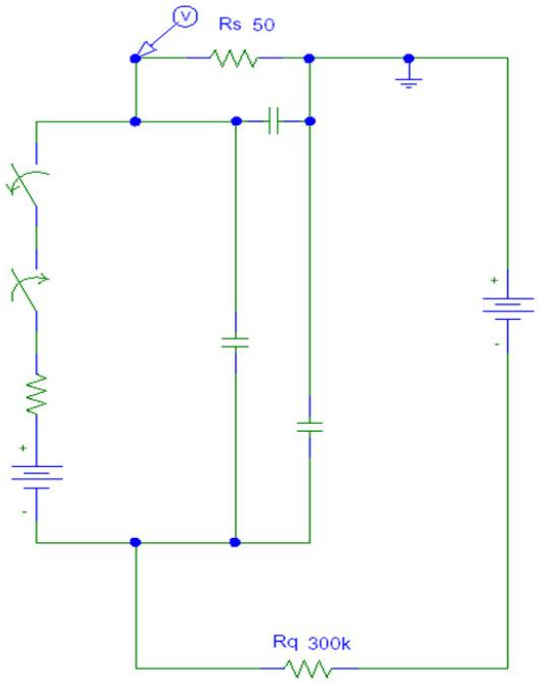

Figure 2-7: SPAD passive quenching configuration with ground on cathode side and full capacitance configuration.

Due to the small magnitude of the capacitance connected in series with the sensing resistor, it do not imply substantial signal modification and is not considered in the simulation, as reported in circuital scheme of Figure 2-1. In passive quenching configuration only the stray capacitance due to the junction semiconductor layer must be considered in the simulation. In conclusion the stray capacitances that must be considered in the simulation of the two passive quenching circuit configuration, of Figure 2-1 and Figure 2-7, are of different values and are located in different positions. To find the exact value of the inverse configuration the calibration procedure should be repeated for the new configuration.

The second result of stray capacitance configuration is that not all the stray capacitances of the system contributes to the signal production. This second result is enforced by the measurement shown in Figure 2-8 containing the fit of the system recharge trend (in red). The growing amplitude trend, that represent the voltage recharge shape, was fitted with an exponential trend. The time constant of the shape is related to the known resistivity of loop C of Figure 2-2 and the total capacitance of the system. The value evaluated with this fit is a bit larger than the total stray capacitance measured in the previous configurations.

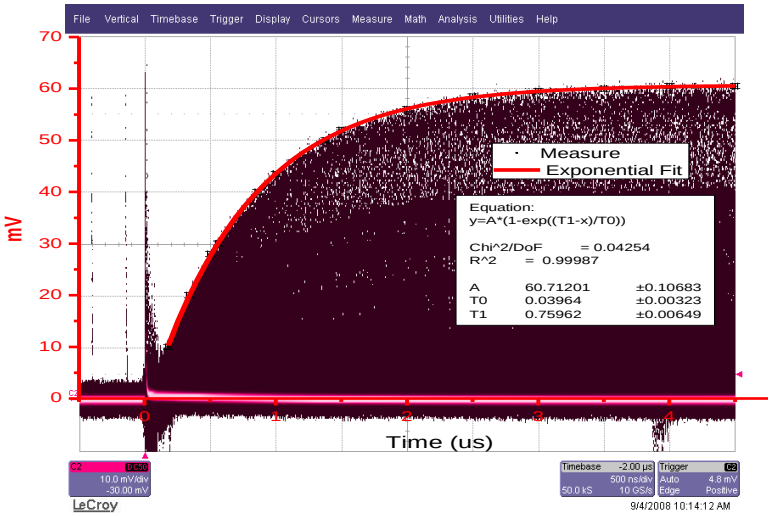

Figure 2-8: Voltage recovery of the PQC SPAD system made with a digital oscilloscope in persistent mode. The maximum voltage amplitude of the produced signals represents the recharge trend.

2.4 Comparison Between Measured and Simulated Signal

Using the configuration of Figure 2-1 and the calibration results we are able to calculate the signal production. The comparison between the measured signal and the calculated one, by PSpice, is presented in Figure 2-9. While the amplitude and time decaying are in perfect agreement, the growth of the simulated signal is faster than the measured one, due to the time performance of the digital oscilloscope used to sample the signal. The bandwidth of the oscilloscope is 1GHz and the shown rise time is exactly one nanosecond, that is the maximum oscilloscope performance. Using a faster oscilloscope the mismatch will be reduced. However the good agreement shows the validity of the electric SPAD model proposed and the goodness of the calibration procedure[21].

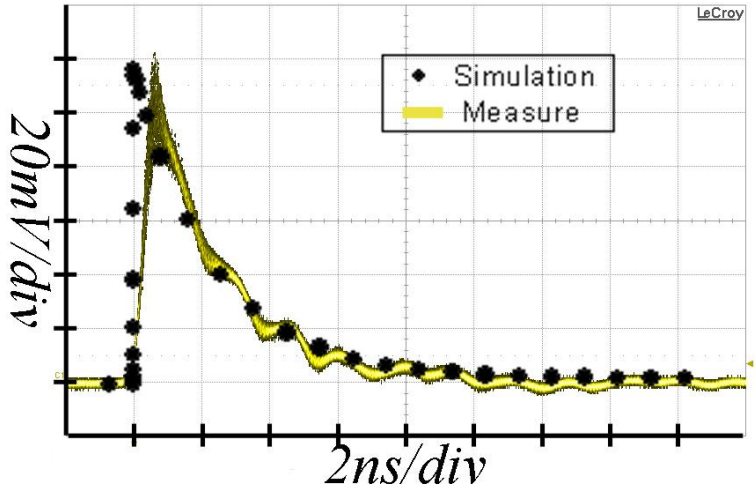

Figure 2-9: Comparison between measured and calculated pulse shape.

The characterization procedure developed and the explanation of the SPAD equivalent circuit for various configuration put us in the condition to design new approaches for the SPAD readout and for the two-dimensional matrix configuration, and also to specify the manufacturing objectives that can improve the performances of our application. In the analysis performed in chapter 5 we will underline the need of signals with fast rise time to improve timing performance,

with convenient amplitude to avoid the use of external amplification circuits, and with fast signal extinction in order to insert, inside a shared readout channel, a big number of produced signals and so a big number of SPAD devices.

2.5 SPAD Double Readout Configuration

As will be shown in the chapter 5, our readout strategy for two-dimensional imaging SPAD array needs two electric signals for each diode[22]. In the device used in this work the two signal are extracted one from the anode and the other from the cathode, as shown in Figure 2-10. The impedance of the front-end electronics is 50 ohm, so to reproduce their behavior inside PSpice simulation only a 50 ohm resistor is needed. The anode front-end is represented by the resistor R-Anode located between anode and ground, while the cathode front-end is represented from the resistor R-Cathode connected to the cathode of the diode by the 5 pF a capacitor C-Decoupling.

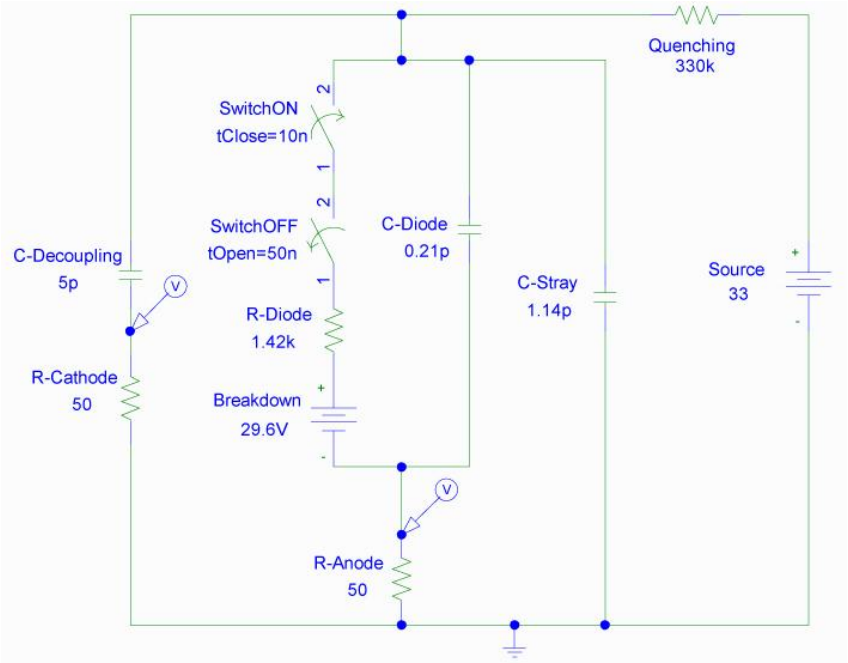

Figure 2-10: Cathode readout with voltage decoupling.

2.5 SPAD Double Readout Configuration

The advantage of a simulation program is not only to test many configurations without losing time and without building real circuit, but, first of all, it is the ability to see how the circuit works collecting information that hardly can be extracted by a real device, and in addition with measurements that do not produce any changes in the circuit, feature that is impossible to obtain in a real circuit. Many simulation steps have been done to arrive to the final result presented in Figure 2-10, which takes into account the diode characterization, the availability of real electric component, and the virtual measurements done during the simulation.

An interesting virtual measurement of the system is the current inside the diode. In the Figure 2-10 the closing time of the "on" switch is 10 ns, which simulates the photon adsorption. In Figure 2-11 this time represents the start of the current inside the diode. The switch closing rapidity can be chosen as one wants and, due to the high rapidity of the avalanche process, the faster value was chosen. When the switch is closed the discharge of the capacitances starts and the current value exponentially decreases. When the current decreases below, typically, 0.1 mA, the avalanche multiplication process reaches a small value and the self sustaining process is no longer guaranteed. This is the time value to be used inside the off switch of Figure 2-10 to stop the avalanche. In the current shape this causes the current reset to zero value.

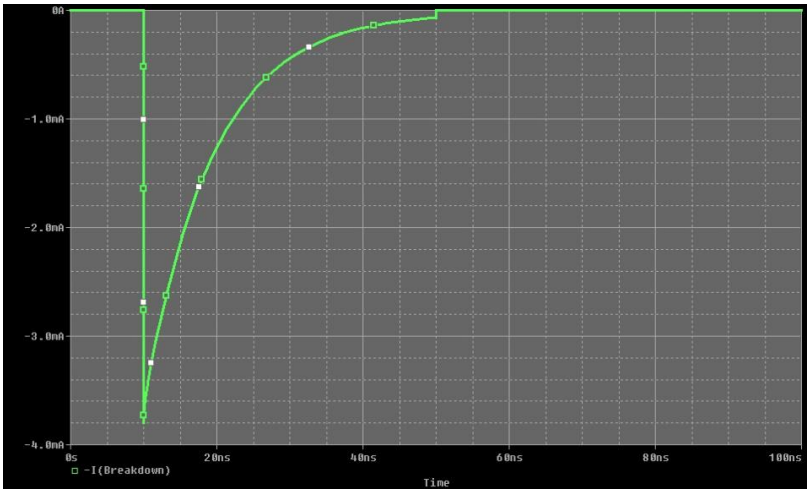

Figure 2-11: Current flowing inside the diode.

The anode readout configuration and the meaning of the signal produced was already shown in the diode characterization. The cathode readout can be done in different way. The system necessary for our imaging sensor must minimize the used components and the produced interferences. The performed simulated tests have shown that the use of a very small capacitor is the simplest way to obtain a cathode readout circuit. Choosing a capacitance we obtain an open circuit that do not perform any substantial variation in the current trip. The capacitance acts as a voltage decoupling that brings the background level of the produced signal from the applied voltage, typically 34 Volt, to ground level. The smallest commercial capacitance was chosen to reduce the increase of charge accumulation, that means a slower signal and a delayed recharge of the system. The produced signal is the derivative of the voltage shape in correspondence of the cathode. The calculated voltage shape in correspondence of the cathode is reported in Figure 2-12, while the produced signal after the voltage decoupling is reported in Figure 2-13 together with the anode produced signal.

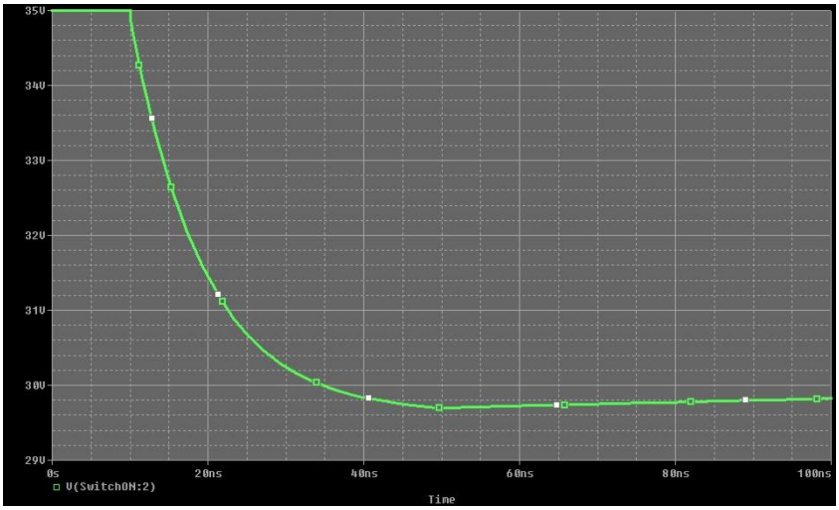

Figure 2-12: Cathode voltage during the avalanche pulse.

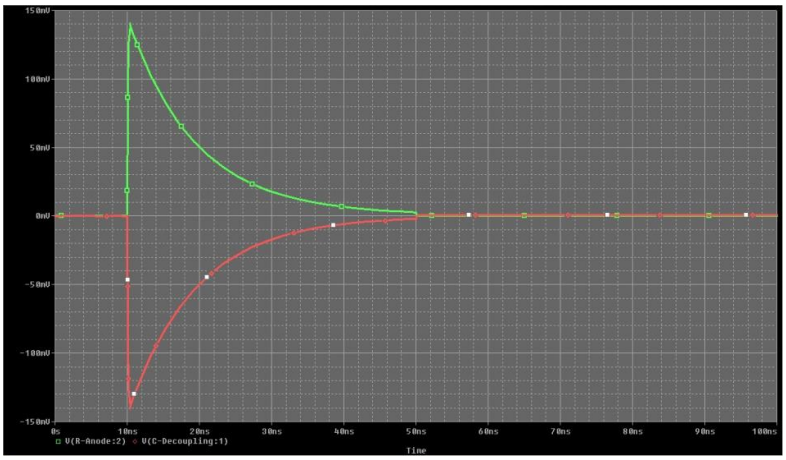

Figure 2-13: Anode and cathode signals calculated with the simulation.

The sensor dead time can be also evaluated by measuring the recharge of the system. Changing the time scale of the Figure 2-12 it is possible to see the voltage recharge (Figure 2-14). The time scale of the produced signal is tens of ns while the recharge is in the µs scale. As shown in the diode characterization, the signal amplitude is linearly proportional to the applied voltage. So the recharge measurement is also important because represents the height of the signal produced as function of the time delay from the previous signal, as reported in Figure 2-8.

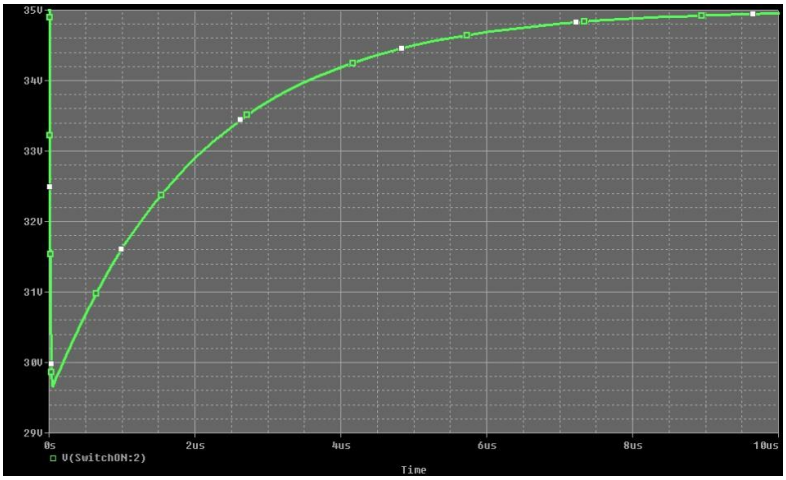

Figure 2-14: Diode recharge, voltage shape in correspondence of the cathode.

2.6 Array Configuration

Our two-dimensional array approach for imaging application well be deeply described in chapter 5. In this chapter we want to show some electric properties of our configuration. In the simulation we have paid attention on a reduced two-dimensional design of our device. A configuration with 6 diodes was simulated, configured in a two-dimensional array of three rows and two columns. In the Figure 2-15 the spatial position of the six SPADs is not designed to show the real spatial position of the diodes, but there is underlined the electric configuration of the system. The six diodes were positioned along a straight line, on the top of the design there are two cathode line, while on the bottom there are three anode line. Each cathode line connects together the cathode of the three diode. Each group represents a column of the two-dimensional SPAD array. The cathode lines connect the diodes to the power source through the shared quenching resistors, and bring the signal to the decoupling capacitances. The two quenching resistors for the two columns are Rq1 and Rq2, while the two capacitances C1 and C2 together with the two resistor Rs1 and Rs2 represent the cathode readout channels. Near this two readout component the two stray capacitance Cs can be seen. In the bottom part of the design the three anode lines connect the two diode of each of the three rows. Inside each anode line there are three resistors, starting from the right, the sensing resistor Rs, the underpass resistors Ra, and the bulk resistors Rb. The bulk resistor connects the three lines but, due to its high value, its influence is negligible. The underpass resistor is a fabrication problem that will be discussed in the section 5.3. The first diode of the anode line is directly connected to the anode sensing resistor, the second diode is connected by the underpass resistor, the third diode, not shown in this reduced array configuration, will be connected through two underpass resistor, and so on. Each underpass resistor causes a signal amplitude reduction that introduce a limit in the maximum number of diode in the same line. This limit will be deleted when the fabrication process will go to the next technology step.

2.6 Array Configuration

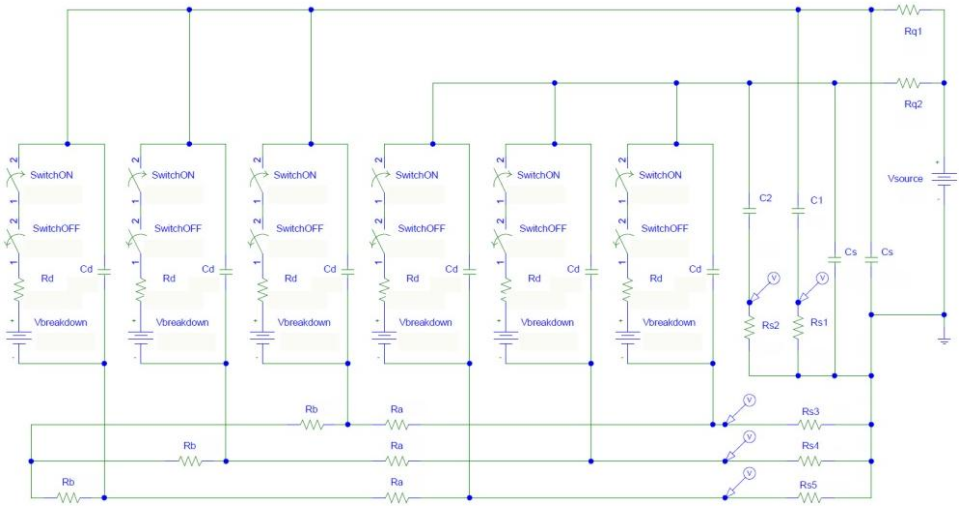

Figure 2-15: Electric schema of 3x2 two-dimensional SPAD array.

The proposed array simulation do not intend to calculate all the parasitic electric component that are located inside a real device. Only the measurement of real device can disclose the result of such complex interaction. However the proposed simulation, that takes into account the main characteristic of the electric configuration, is able to show and to make understandable an unexpected effects that we encountered in real device, the inverse electric cross talk. In correspondence of an anode signal produced by the adsorption of a photon a time correlated signal was produced in the others anode readout channel. The amplitude of the subordinate signal is one order of magnitude lower and is of the opposite sign, which is useful to discriminate it. For this reason readout channel has been chosen to select only the signal produced with the right sign. In the electronic chain the anode real signal is positive, was inverted by an amplification with amplifier factor -1 and is read by a Constant Fraction Discriminator sensible only to negative signal. In the Figure 2-16 there is shown the measurement of two anode channels after the amplification stage. The first channel (yellow) shows a little positive signal in correspondence of a true negative signal of the second channel (magenta). After few time the inverse situation occur, true signal on the first channel and false signal on the second channel. The simulation makes we

able to understand that this electric coupling is due to the capacity of the quiet diodes. The electric signal propagation is the same of that used for the cathode readout system. The junction capacity of the diodes connected each other by the same cathode contact, carries out the same effect of the decoupling capacity of the cathode readout system. So an inverse signal is produced on the other anode sensing resistor.

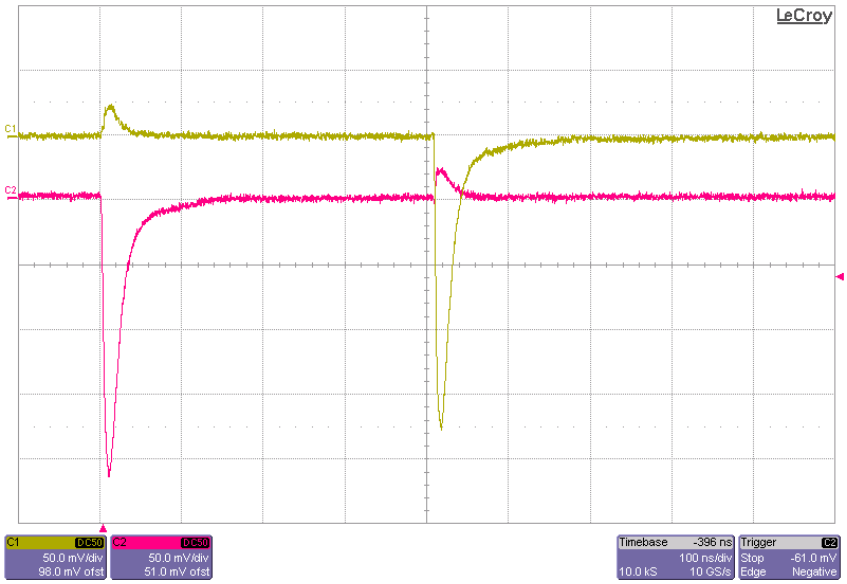

Figure 2-16: Simulated propagation of two signals inside the same anode metallization, and reflected signal on other anode channel.

2.7 Prototype: Binary Indexing Readout

In designing an imaging device two requirements must be fulfilled. The first is the spatial recognition of the fired pixel. The second is to increase the number of matrix elements with the smallest possible increase of necessary readout channels. Our imaging approach described in section 5.2 is an innovative solution for indexing a square matrix with n^2 elements, with $2n$ readout channel. As result of the collected experience in the electric design of simulated circuit we have produced another solution for the spatial recognition of the diode position.

Coupling the diodes with a different number of readout channels we obtain a binary word that identify the position of the diode. In Figure 2-17 we show a scheme for the reading of seven diode with only three readout channel. The readout scheme used is the same used for the cathode, already proposed in section 2.5, a coupling capacitor connected to a sensing resistor. The difference is that each diode is connected to a different set of sensing resistor. Starting from the right, the first three diodes are connected to only one resistor, the first diode to the first resistor, the second to the second and so on. Each of the three next diodes are connected to two sensing resistors, the first is not connected to the first resistor but is connected to the second and the third ones, the second diode is not connected to the second readout channel, and the third diode is not connected to the third readout channel.

In the simulation scheme we have decided to produce seven photon adsorptions, one for each of the seven diodes separated by 20 ns each other. The signal produced by this configuration is shown in Figure 2-18. The three colours used to emphasize the three readout channel of Figure 2-17 are also used to plot the three readout signals shown in Figure 2-18. The figure is clear for the first three produced signals, because each readout channel registers only one diode. The following three events are registered by two readout channels at the same time, so in the figure we obtain the pile up of two signals for each fired diode. Depending on the printing order one colour is superimposed to the others. However the symbols coupled to the colour mark make visible the concurrent production of signals. The last signal is reported by all three readout channel, and the concurrence of the three symbols can be seen.

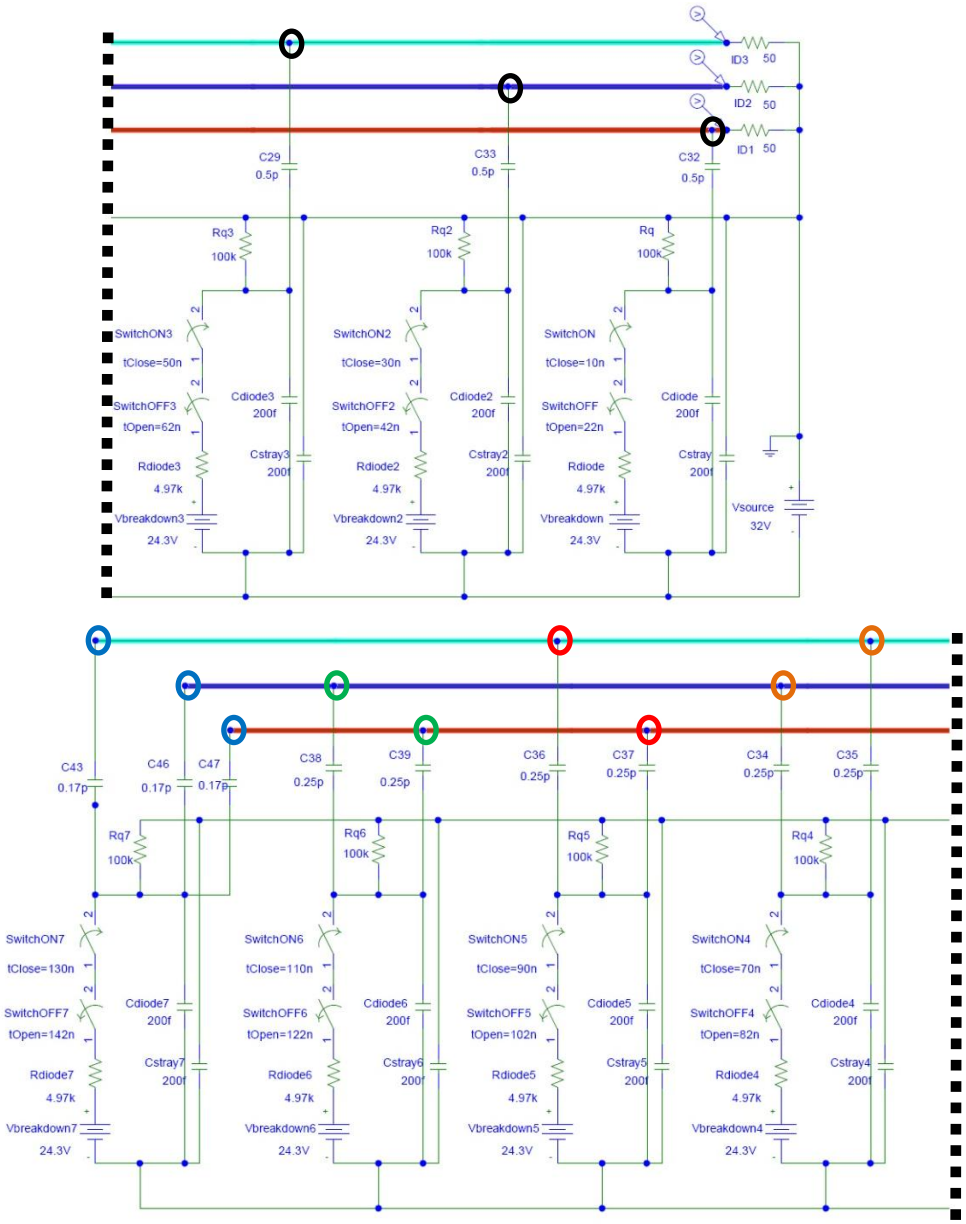

Figure 2-17: Row configuration with triple channel readout system for binary addressing for seven diodes.

The difference in the signal amplitude is caused by the different values chosen

for the capacitor. We decided to preserve the time characteristic of the seven diodes, so we decided to fix the total charge connected to each diode. The signal amplitude is proportional to the capacitance value. So if the diode is connected to only one readout channel only one capacitance is necessary, and the value is equal to the total capacitance available for one diode. If the signal must be produced on two channels the total available capacitance must be shared for the two capacitances. In the last diode, where three signals are necessary, this value must be divided by three. In practice the amplitude of the signal produced is the same but it must be divided between the number of involved channels.

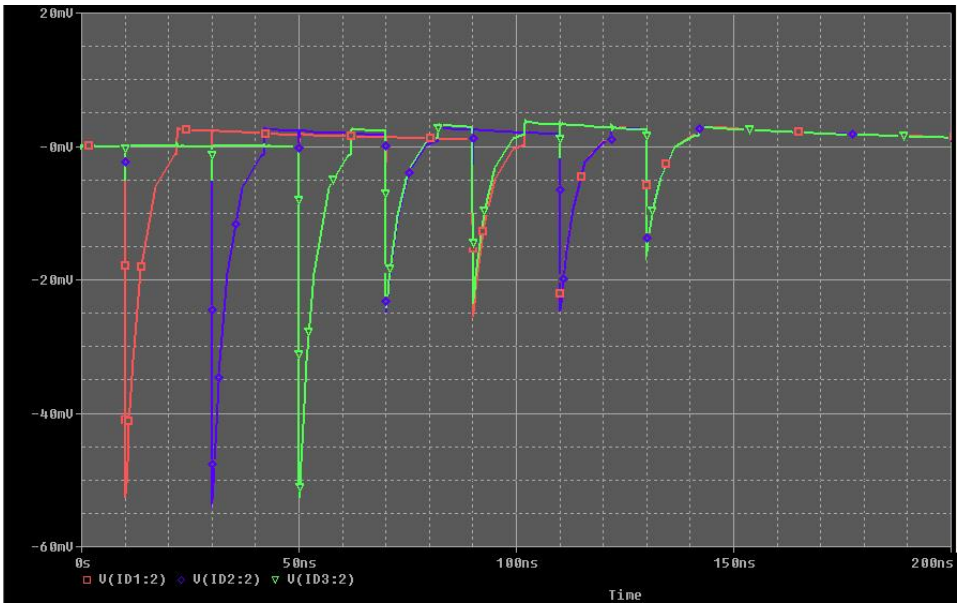

Figure 2-18: Signal produced in the binary indexing of seven diode into three readout channels.

In passive quenching circuit configuration of SPAD devices the signal amplitude cannot be used to recognize the diode position, because this parameter is not fixed, but changes according to the recharge state of the diode. Instead, for SPAD with active quenching system the amplitude of the signal is fixed and can be statically selected to identify the position of diode that shares the same readout channel. Adding together this two features, the binary indexing and the amplitude recognition, we can multiply the number of diode per readout channel

and increase the imaging definition with a little increase of the device complexity.

This two new approaches for array readout result from the simulation approach and are not yet tested, but they can represent future device implementations.

3. SPAD Counting Correction

Since many years our research group is developing a Single Photon Avalanche Diode suitable for time resolved single photon imaging techniques[10][22][23][24].

In this chapter we describe how we developed a simulation code for the statistical behavior of the SPAD. This code reproduces the behavior of the device under different illumination sources, taking into account its dead time and its noise production.

We study the signal generation process and the DT mechanisms of the device. We start from the G-M studies present in Literature, and also analyze some effects, lacking in G-M counter, that should be introduced in the analysis of semiconductor device as afterpulse, reduced PDE and noise production.

We have used simulation code and dedicated experimental setup to verify each obtained results.

3.1 Simulation Technique

In the last years the simulation has became an important step of research process. The main impulse to this process is coming from the rapid growth of personal workstation computational performances, from new friendly access to large computational facilities, like INFN-GRID projects[25][26], and from the evolution of software dedicated to the simulation, like Matlab, PSpice, which we

used in this PhD work, or Comsol-Multiphysics, Opera, etc. All scientific areas take advantages from simulation, Physics, Chemistry, Engineering, Medicine, and, consequently, all innovation technology processes. The ability to predict the behavior of a mixture of well know effects, and vice versa, the ability to search combination of the fundamental rules that generates a well know effect, push the simulation process between the inductive and the deductive scientific research methods.

In the next subsections we show the simulation technique that we have developed to verify results in SPAD dead time analysis (section 3.3) and to study the dead time effects on a sensor subjected to time dependent sources (chapter 4).

3.1.1 Light Source Simulation

The typical application for our counting device is the detection (time, position) of photons inside an acquisition time window. For statistic significance many time windows are acquired, and all data are merged into an histogram of the photon arriving times. Typical investigated light source is produced by a system excited by a rapid energy pulse that decades with a delayed light emission. By synchronizing the acquisition time window and the exciting pulse we obtain an histogram that shows the decaying trend.

The first step for the SPAD simulation is the developing of the photon source inside the time window. Starting from the simplest instance we will show how to produce a constant photon rate. After that we will add the step needed for the simulation of time modulated light sources.

Using a Poisson distribution we can decide how many photons to put inside each acquisition time window. The equation that describe the Poisson distribution is:

$$f(k) = \frac{\lambda^k e^{-\lambda}}{k!} \qquad 3\text{-}1$$

Where f is the probability to have k events, and λ the mean expected value. In Matlab we use the function *poissrnd()* that is a random numbers generator that

follows the Poisson distribution.

Few example of Poisson distribution, used for our simulation, are presented in the Figure 3-1, for different photon rate λ.

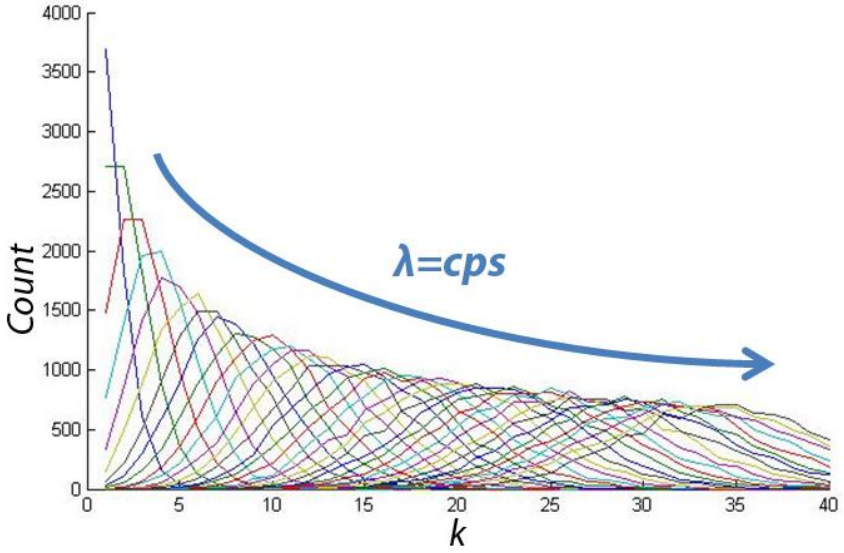

Figure 3-1 Many Poisson distribution increasing the mean value of incident photons.

The positions of the *k* photons, inside the time window, is randomly chosen using the function *rand()*; this function is a random number generator in the interval from zero to one, that, multiplied for the window time extension, generates random position inside the interval of interest. The simulation outputs is the flat distribution of photons shown in Figure 3-2 at various count rates.

In the analysis of the produced events is useful to consider the Time Interval Density Distribution (TID) which, for a constant rate, produces a simple exponential function. We have implemented this function in the Matlab simulation code to compare experimental results and simulation predictions. The output of this function calculated on the data shown in Figure 3-2 is shown in Figure 3-3.

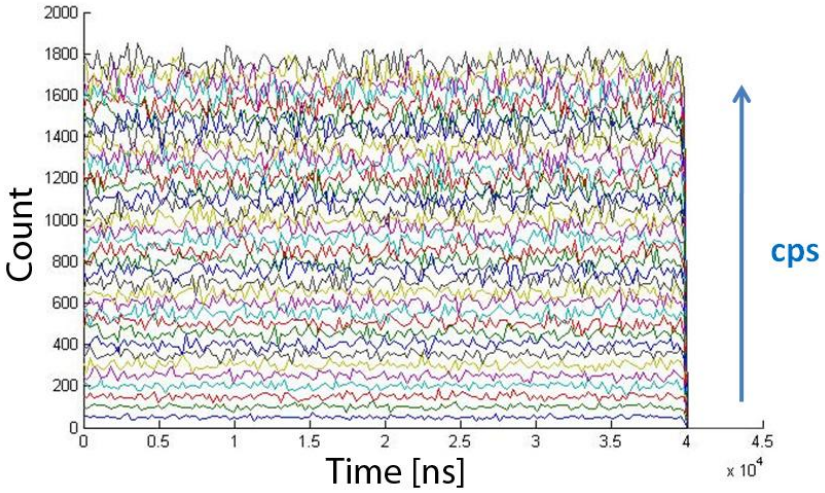

Figure 3-2: Histograms of the photon arriving times on increasing the mean value of the incident photon rate.

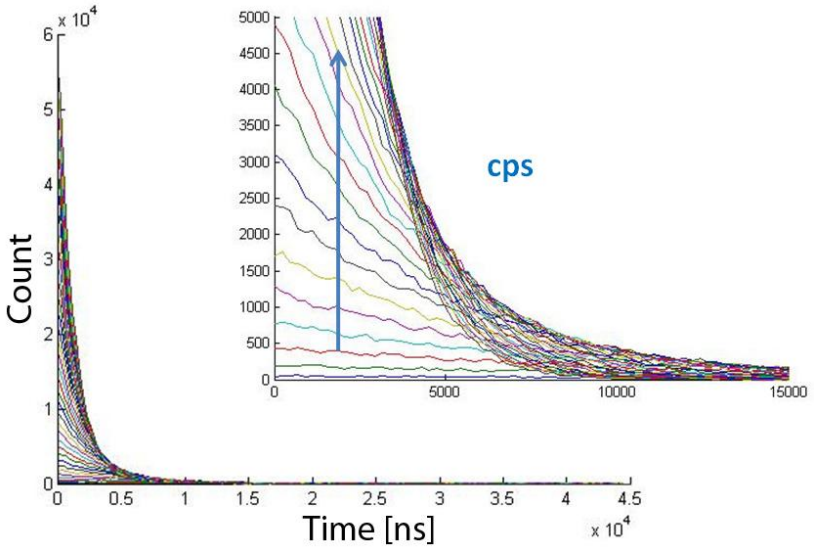

Figure 3-3: Time Interval Density Distribution calculated on simulated photons rate shown in Figure 3-2.

For the simulation of a time dependent photon source we have used the shape of the wished light source as a weight function. The first step to do is the normalization of the shape to the range from zero to one, being one the maxi-

mum desired photon rate and zero the no-light state. The result is the light weight function. After that, for each photon we generate a random time position, and a weight number randomly chosen in the range from zero to one. Comparing the two weight, if the photon weight is lower than the light weight function in the time position of the photon, the photon is considered, otherwise it is discharged. In such a way the photon time distribution follows the wished time distribution. The result is shown in Figure 3-4 where in red there is the desired light shape and in blue there are the photon counts. The accord is an obvious result due to the procedure we followed, and it will growth on increasing the total number of photons simulated.

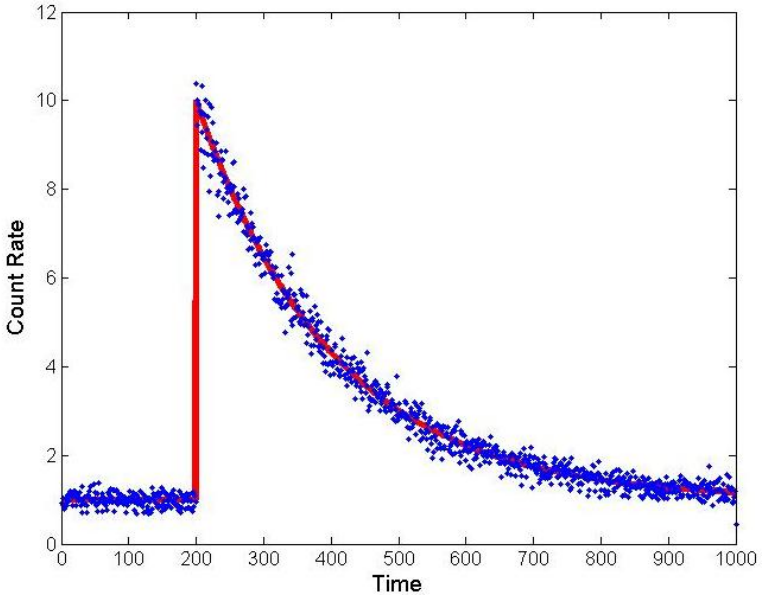

Figure 3-4: Simulation of time dependent photon sources; line: desiderate shape; dots: simulated photon count rate.

3.1.2 Dead Time Simulation

Dead Time simulation means to take in consideration the DT rules and, inside each simulated time window, to distinguish the detected photons from the lost ones. The first rule for the DT is that all events that arrive inside a DT period are considered lost and do not increase the counted rate produced by the

sensor. As described in the section 1.5 there are two elementary type of DT the P-DT and the NP-DT. Each of them add a new rule in the DT behaviour. The rule introduced by the P-DT is that the events that arrive inside the P-DT causes the restart of a new DT period. While the rule of NP-DT is that the events do not cause the restart of the DT. To show how our simulation works we consider the hybrid-DT case, in which the produced DT period is composed by a sequence of the two elementary DT types. In the Figure 3-5[31] a photons sequence and the produced DT periods are taken into account. The simulation starts taking into account the first photon and marks the following time interval as a DT period. In this case the DT period is composed by a first NP-DT (streaked rectangle) followed by a P-DT (rectangle with dots). The second photon arrives inside a NP-DT and is not detected nor new DT period is marked. The third and fourth photons arrive out of the previous DT periods and are detected, and their DT periods are marked. The fifth photon arrives in a P-DT, and, even if it is not considered as detected, a new DT period starts from its position. The same procedure is followed for all sequent photons of all simulated windows. The same simulation strategy can be used for any device with any type of DT. This DT simulation procedure can also be used in constant and in time dependent environment. In the Figure 3-5 the counted photons are marked with a arrows, lost photons that do not produce any DT are marked with a arrow and a square, and lost photons that prolong the DT period are marked with a arrow and a circle.

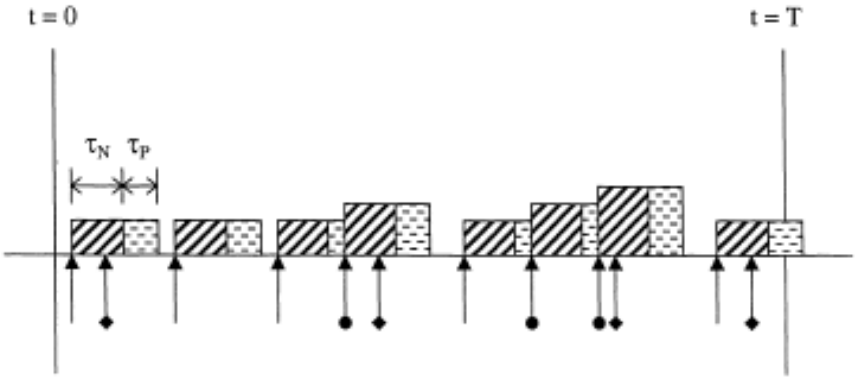

Figure 3-5: DT rules behaviour on acquisition time window.

These simulation results, especially in the application on a time dependent source (chapter 4), show that simple rules, applied to a simulation program, make comprehensive complex behavior. The plus valence of the simulation is the complete transparency of all calculated data. While, in an experimental setup, is not possible to identify the real DT extension and the number of lost photon, in simulation process all data are visible and all consideration, on that data, are possible. Only with such ability we was able to obtain the results that will be shown in chapter 4 and published in[9]. It is obvious that the consideration coming out from a simulation process are restricted to the chosen model, which could be not accurate as expected. For that reason we always compared simulation results with experimental data.

3.1.3 Noise Simulation

The noise is an important characteristic of all counting device. Introducing the noise into the simulation, we obtain another example of the benefits of the transparency feature of the simulation procedure. In such case we can distinguish noise from photon counts, that in a real experimental setup cannot be distinguished.

The first step of the simulation is to select the constant rate values of photon and noise that we want to simulate. We use the same procedure described for light in section 3.1.1 to obtain two time windows, one for the noise counts and the other for the photons (Figure 3-6).

In section 3.4 we will show that in SPAD device we can consider the noise production neglected during the NP-DT. We have translated this rule by developing a simulation algorithm that preserve the noise count rate out the NP-DT intervals.

The noise window is used to find the time distance between random noise counts, and to preserve the noise count rate. A correct placement of noise events in the photon window is the objective of noise simulation. The result we want to obtain is an output window where, without considering the NP-DT extension, the time separation between noise events is the same as in the noise window. To

do that, starting from the beginning of the photon window, we have measured the time free from NP-DT. When the time position of the first noise is achieved, the first noise count is inserted into the output window, and, starting from that point, a new NP-DT period is placed. In such a way the first noise count collected by the sensor was simulated. If a photon is captured inside this NP-DT it will be considered lost and its DT production is deleted. Going on, whenever a time interval, free from NP-DT, is measured equal to the time distance to the next noise count, another noise count is inserted.

For reason of clarity we shown in Figure 3-6 a real example with the measurement of such intervals. In the noise window we encounter the first noise count at three Time Units (TU). The first photon, of the photon window, is at two TU, so in the output window the first count will be the photon. After inserting the NP-DT produced by the photon, we can measure three TU free from NP-DT only after five TU. In this point we can insert the first noise count. The second photon is captured by the NP-DT produced by the noise count so it becomes a lost photon. Going on with such procedure we can insert the fourth photon, and the second noise is inserted after thirteen TU from the beginning of the output window.

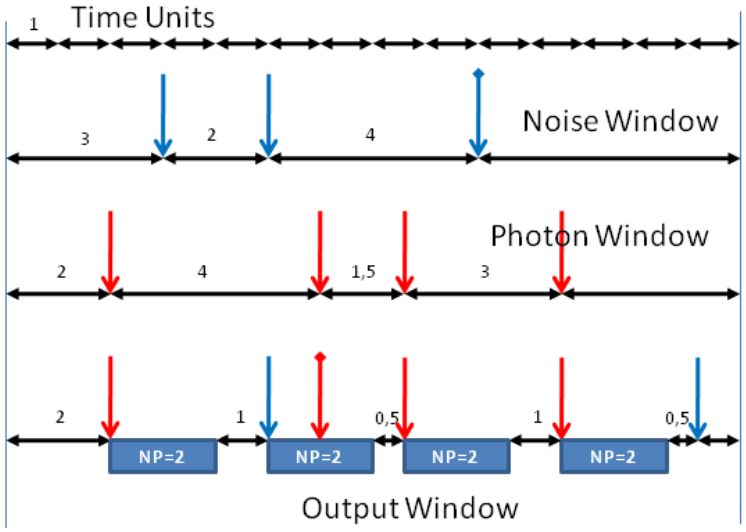

Figure 3-6: Combination of noise time window and photon time window to obtain the output response of the simulated sensor.

In absence of noise, the third photon of the photon window, of Figure 3-6, must be considered a lost photon, because the distance from the previous photon is smaller than the NP-DT extension. Instead, after the introduction of the noise counts, the NP-DT, produced by the first noise count, deletes the second photon and the third photon is detected. This is a clear example of how the noise introduce changes in the photon measured rate.

Spreading the noise window in the time free from NP-DT, some of the noise counts exit from the simulated output window, and will be not considered. This means that the noise count rate production becomes lower than the one measured in absence of light and decreases with the increasing of incoming photon rate. A numerical evaluation of this process will be described in section 3.4.

To complete the simulation of SPAD device we must add the production of the P-DT as shown in section 3.1.2 and finally distinguish detected events from lost events. The feature of simulation is that we are able to evaluate the number of detected and lost events for both photons and noise.

3.2 Counting Correction

In all counting systems noise and DT losses should be taken into account to evaluate the real amount of events from the measured ones[27]. The DT generates distortions in the high rate working regime while the noise generates distortion in the low rate working regime. SPAD device suffers from both noise production, due to the thermal generation (section 1.6), and DT losses, due to the recharge of the system (section 1.5). We have already said (section 1.2) that the SPAD counting characteristics are closest to that of Geiger-Muller device. Also the DT process is quite similar. The noise effect is different because is an intrinsic phenomena of the SPAD device and is not due to an external source of counts, like in the case of G-M device. The SPAD is also affected by the afterpulse phenomenon and, during the recharge process, by the variation of the photon detection efficiency (PDE). All these phenomena not only limit the maximum measurable count rate but also imply a correction in the low count rate regime. Each of this aspect will be detailed studied in the next sections.

3.2.1 Dead Time Correction In Geiger-Muller Device

All photon-counting systems show a DT period that affects the measured counting distribution. Generally speaking, the greater difference between the true count rate and the measured count rate is due to the DT losses. So the effects of DT on counting distributions in single-channel detectors have been extensively studied.

Since 1940 many works have been published about the DT of the Geiger-Muller counter, used in nuclear physics[28]. To extend the maximum counting rate of the device, many models were developed and applied to the DT correction [29] [30].

As shown in section 1.5, there are two type of DT, the paralyzable (P-DT) and the non-paralyzable (NP-DT) one. In this two simple case there are two different relations between the real counting rate *n* and the measured one *m*. In the case of a P-DT of τ_p time extension, the relation is:

$$m = n \cdot \exp(-n \cdot \tau_p) \qquad 3\text{-}2$$

While in the case of NP-DT of extension τ_{np} is:

$$m = \frac{n}{1 + n \cdot \tau_{np}} \qquad 3\text{-}3$$

In real devices there are many sources of DT, and they can act in series[32] or in parallel[29]. In G-M counter there are two DT sources acting in series[31], the first is the time duration of the signal (NP-DT τ_{np}), and the second is the recharge time needed to produce a signal with amplitude greater than the discriminator level (P-DT τ_p). The effect of this DTs combination can be described with the formula of the hybrid model [31]:

$$m = \frac{n \cdot \exp(-n \cdot \tau_p)}{1 + n \cdot \tau_{np}} \qquad 3\text{-}4$$

We found that this equation can be also used for SPAD detector provided that all the differences between these two devices have to be considered.

3.3 SPAD Dead Time Configuration

In the G-M device the recharge process starts immediately after the signal end[12]. In SPAD device the DT extends up to the start time of the recharge process, when the avalanche process stops[12]. For our SPAD device, using a digital oscilloscope in persistent mode, we have estimated that the recharge starts after 170ns. In Figure 3-7 it is possible to see that the smallest second signals, after the trigger signal, start after a delay of approximately 170ns, marked with a vertical broken line in Figure 3-7. After that time the height of the produced signals starts to grow proportionally to the recharge of the system, described in section 1.5.

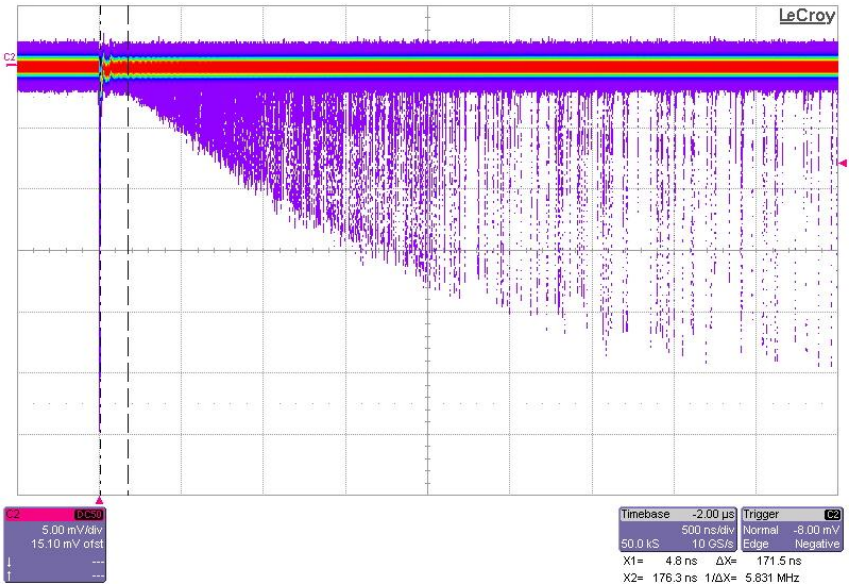

Figure 3-7: Digital oscilloscope image in persistent mode, first part of the diode recharge, delay after which it is possible to see the first small signals.

In the G-M counter the non paralyzable DT is followed by a P-DT due to the recharge process. In the SPAD device we must consider not only the P-DT due to the recharge process but also the variation of the Photon Detection Efficiency (PDE) and the afterpulse.

The PDE of the SPAD is proportional to the overvoltage applied to the diode (section 1.9)[12], because the avalanche generation process depends on the

overvoltage value. During the recharge process, too low overvoltage values correspond to decreased detection efficiencies. So the corresponding time interval can be considered like a NP-DT, because the lost photon doesn't restart the recharge process. The DT caused by the reduced PDE and the DT caused by the recharge process start simultaneously, after the quenching of the avalanche process. During the period in which the two types of DT coexist the system cannot be described with two DT in parallel as in[29], because in SPAD device the PDE varies during the recharge process, and the generalized Muller equation cannot be used.

To solve such complex DT configuration all SPAD's DT sources must be considered in their interactions. There is a NP-DT, due to the signal duration and to the avalanche quenching time (170ns), followed by two DTs in parallel, one due to the recharge process and the other due to the reduced PDE. The recharge process DT is paralyzable and much longer than the other one. The reduced PDE DT is non paralyzable and the weight of this process vary during the recharge process. Figure 3-8A represents this DT configuration.

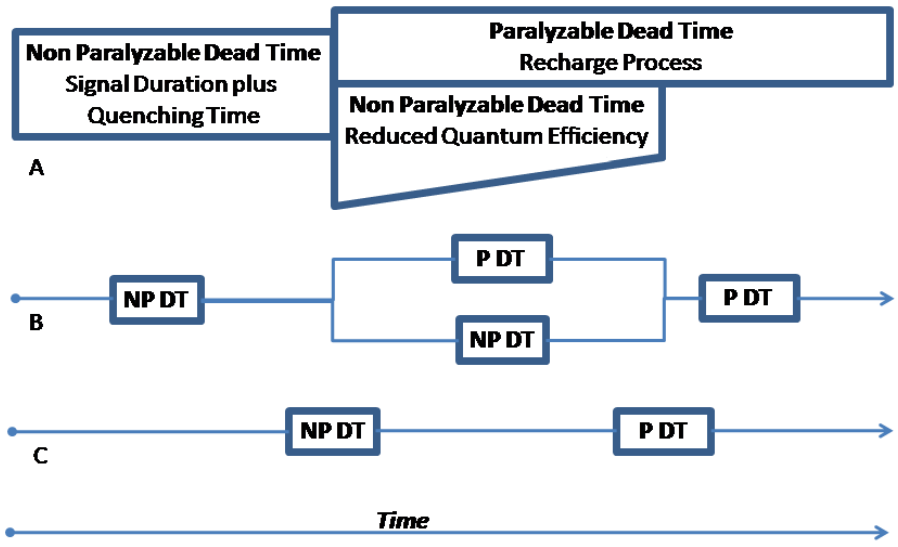

Figure 3-8: DT configuration of SPAD. A) real. B) circuit schema C) simplified schema used for the DT correction.

To simplify the DT configuration we took the variation of PDE at the extremes and assumed that the parallel circuit can be described with a series of DT. The first NP-DT is generated by the predominance of reduced PDE process over the recharge process, and the second P-DT is generated by the quick death of reduced PDE process. Joining together the DTs of the same type we obtain a simple two DT series circuit of Figure 3-8C.

This reduced SPAD DT configuration is similar to that of G-M counter, a series of a NP-DT followed by a P-DT, but the causes of this configuration is different: the first DT is due to the sum of quenching process and reduced PDE, the second DT is due to the recharge process that exceed the reduced PDE duration.

3.4 SPAD Noise Correction

SPAD devices are affected by a non negligible thermal noise generation process, typically few Kcps. Especially at low rate regime the accurate determination of the noise part of the total output counts must be well known. The thermal noise generation is characterized by a strong dependence on the overvoltage applied to the junction. So, during the recharge process, the noise generation efficiency is less than it should be normally and grows according to the recharge process. Increasing the photon count rate increases the time in which the device is in a recharge state. Then an increasing of the photon count rate should correspond to a decreasing of the time available for the noise production and, consequently, the measured noise count rate decreases.

To simplify the problem, we assume that the recharge dependence of the noise production is strong, and we suggest two distinct behaviors, the first, in correspondence of the NP-DT, in which the noise is inhibited, and the second where the noise is enabled. By using Montecarlo simulation and experimental analysis we have obtained two results:

1. In the response equation of hybrid model (Eq. 3-4) the true incoming rate *n* is substituted with true incoming photon rate *p* plus the noise production *d*:

$$m = \frac{(p+d)\cdot \exp(-(p+d)\cdot \tau_p)}{1+(p+d)\cdot \tau_{np}} \qquad 3\text{-}5$$

2. It is necessary to distinguish the noise rate *d* from the dark rate d_o, where dark rate is the measured noise rate in absence of light:

$$d_0 = \frac{d * \exp(-d * \tau_p)}{1 + d * \tau_{np}} \qquad 3\text{-}6$$

To obtain the real photon rate *p*, we should subtract the dark count *d* from the true signal rate *n*. This allows to evaluate the noise production at every photon count rate. The result is that it is possible to neglect the noise production in low count regime, reducing the indetermination from the dark noise value to its square root (the variance). So the variance of the dark count now identifies the lowest measurable value of the true incident photons rate. Because the variance is the square root of the count rate, in a device with 1kcps dark count rate the minimum true photon rate measurable is around 50cps. This allows to extend the minimum measurable rate value of more than one order of magnitude.

3.4.1 Simulation Validation

We found in simulation an useful approach to better understand the behavior of a SPAD device (section 3.1). The simulation allows to clearly distinguish the counts coming from noise, and that produced by photons, the counted events and the lost events, as shown in Figure 3-9. Starting from Eq. 3-5, describing the total measured rate, it is possible to split the contribute of photons:

$$m_p = \frac{p \cdot \exp(-(p+d) \cdot \tau_p)}{1 + (p+d) \cdot \tau_{np}} \qquad 3\text{-}7$$

from the contribute of the noise:

$$m_d = \frac{d \cdot \exp(-(p+d) \cdot \tau_p)}{1 + (p+d) \cdot \tau_{np}} \qquad 3\text{-}8$$

In Figure 3-9 it is clear the accord between the data predicted by Eqs. 3-5, 3-7 and 3-8, and the simulated data.

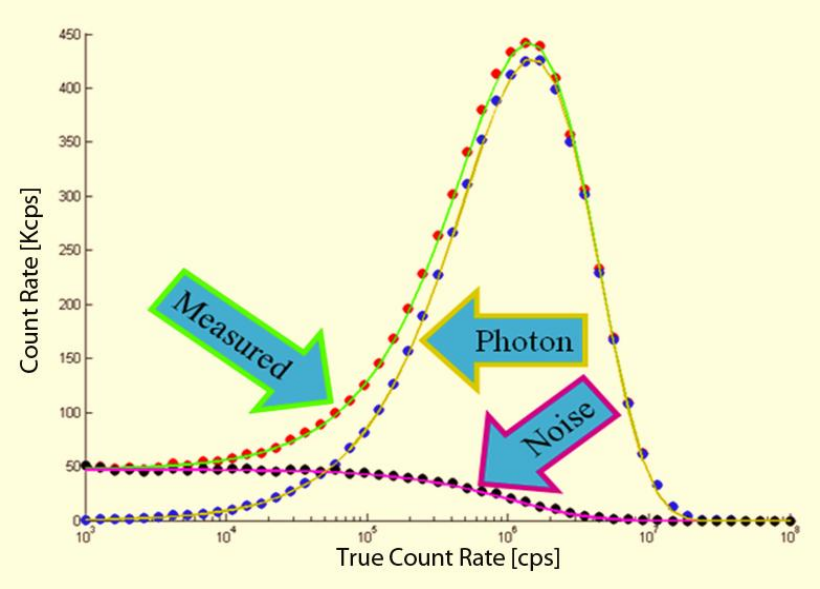

Figure 3-9: Lines, prediction of measured count rate (Eqs. 3-5, 3-7 and 3-8); dots, simulated data.

3.4.2 Experimental Validation

The simulated results, with the distinction between noise and photons counts, can't be simply obtained in an experimental setup. We used our 10×10 SPAD imaging sensor[23] with a special illumination source, to obtain data comparable to the simulation prediction. We used a black surface with two hole, backlit by a Light Emission Diode (LED). The power of the LED is controlled to obtain a constant light source with selectable intensity. For the SPAD matrix we used one passive quenching system connected to each column, and twenty readout system, one for each row and column.

The diodes of the same column share the overvoltage and the recharge DT. Each column can be assimilated to one big diode with ten spatially separated active depletion regions. As shown in Figure 3-10 in correspondence of column 8 only one diode is enlighten, and we can distinguish the photon signals originated by that diode from the signals produced by the noise in the other part of the column 8 (Figure 3-10). Like in Figure 3-9, in Figure 3-10 we can distinguish the

total measured data, the photon and the noise contributions. The shape of these quantities is in accordance to what shown in Figure 3-9. The green area is the total measured rate of column eight decreased by the noise of the nine non-enlightened diodes. This represents the photon count rate, but should be remind that it includes the noise production of the enlightened diode. Nevertheless, the noise count rate production of the enlightened diode is the same of the other nine diodes.

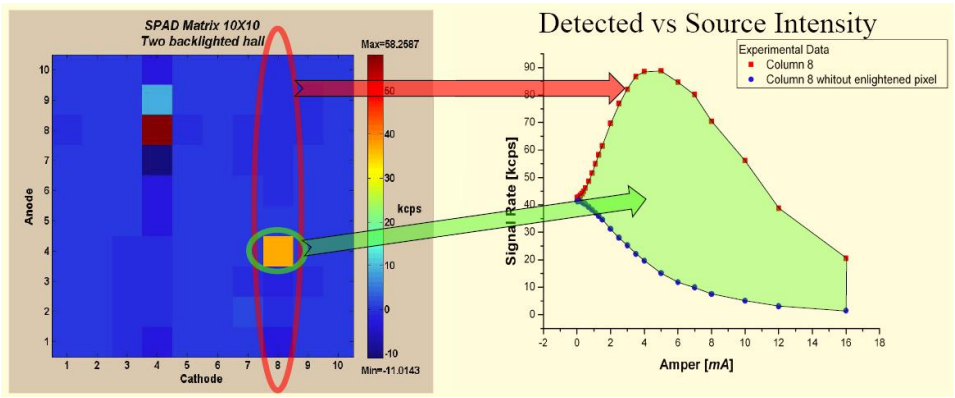

Figure 3-10: Left, Time Resolved Single Photon Imaging of two light spot; Right, in red measured rate of the whole column eight, in blue measured rate of non enlightened column eight, green area represent photon measured rate.

3.5 Afterpulse

In SPAD device the afterpulse is caused by local crystallographic defects that insert deep energy levels inside the gap. Such levels can capture charge carriers during the avalanche process and release them with considerable delay. These charges can trigger the NP-DT process or increase the output signal rate of the device.

To evaluate the photon rate dependence of this process we have mixed two photon sources, a pulsed laser and a constant light source. The laser signal can be detected if previous signal is distant in time more than a DT interval. The laser generates a high and tight peak of counts, followed by a DT interval during which noise and constant light source cannot trigger an event (Figure 3-11). Af-

ter this time interval, in absence of the afterpulse, the count rate should quickly return to the previous constant value. The afterpulse causes an increase of the count rate followed by an exponential decay trend. After 6 μs the afterpulse phenomenon is completely concluded and a plateau, due to the constant signals source, follows. On increasing the rate of constant light source the total measured afterpulse linearly decreases from a 4% value in dark condition to a non measurable value at 55kcps (section 1.4). As a consequence the Eq. 3-5 should be multiply by a linear function of the incident rate that represents the afterpulse modulation process. Due to the fact that the correction weight is at most 4%, and it occurs only in low working regime, this function was not deeply studied.

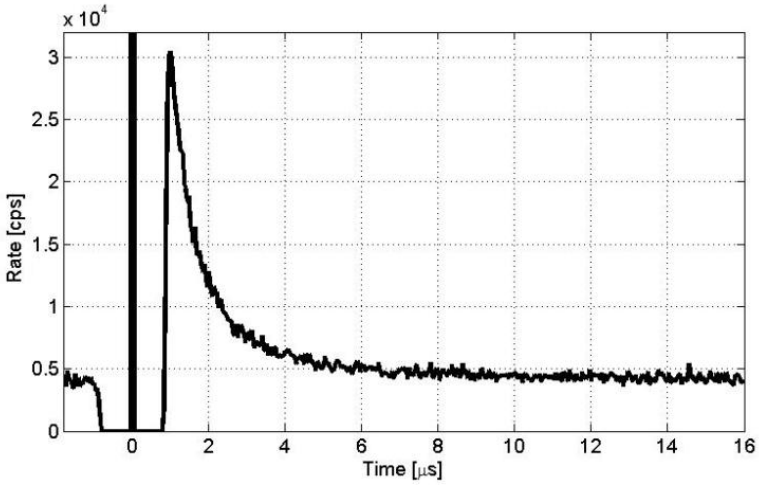

Figure 3-11: Measurement of afterpulse correlated with a laser pulse embed in a constant light background source.

3.6 SPAD Dead Time Correction

The measured signal rate versus the real incident photon flux is shown in Figure 3-12. We found that the proposed Eq. 3-5 of the hybrid model fits with good precision our experimental data along more than four order of magnitude. This is a validation of SPAD DT analysis discussed in section 3.3. The validity of the proposed DT configuration is further confirmed in the analysis of the variance characteristics of the device reported in the section 3.7. The fit of experi-

mental data with Eq. 3-5 gives a DT composed by a NP-DT of τ_{np}=660±20ns and a P-DT of τ_p=310±10ns.

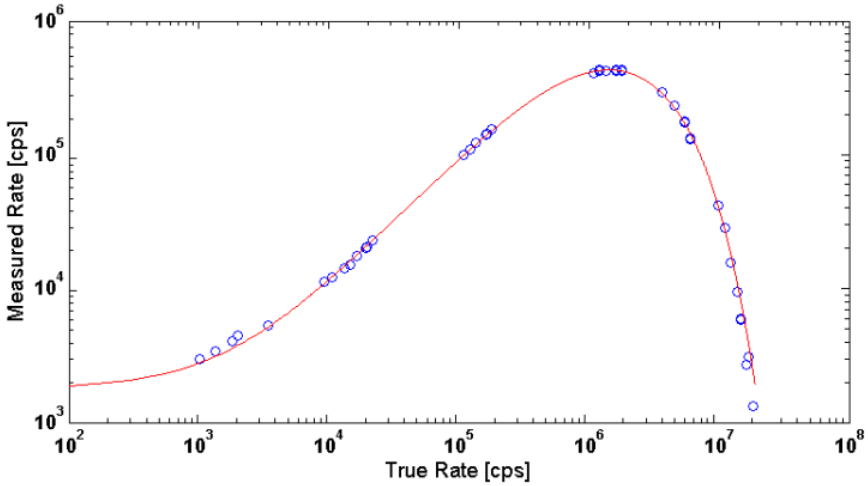

Figure 3-12: Relation between true and observed counting rates; circle, experimental data; line, hybrid model fitting.

The Figure 3-12 shows that the Eq. 3-5 cannot be simply inverted because it is not a monotone function. In order to eliminate the ambiguity we have analyzed the Time Interval Density distribution (TID).

The Poisson theory predicts that in absence of DT, the TID is a simple exponential distribution. In presence of DT the TID distribution is subjected to a cut-off between t=0 and t=DT, during which the signals are inhibited. After the DT cut-off, in presence of non paralyzable DT, the distribution follows the exponential distribution while, in presence of a paralyzable DT, there is a plateau for a time equal to the DT[33]. In the hybrid model, the theory[33] describes a modification of the P-DT plateau. We have measured the TID shape changes at all the true counting rates. Some of the results, approximately one per order of magnitude of the counting rate, are shown in Figure 3-13. The changes in the trends turn out to be useful in eliminating the ambiguity in the inversion of Eq. 3-5, allowing to evaluate the true photon rate from the measured one.

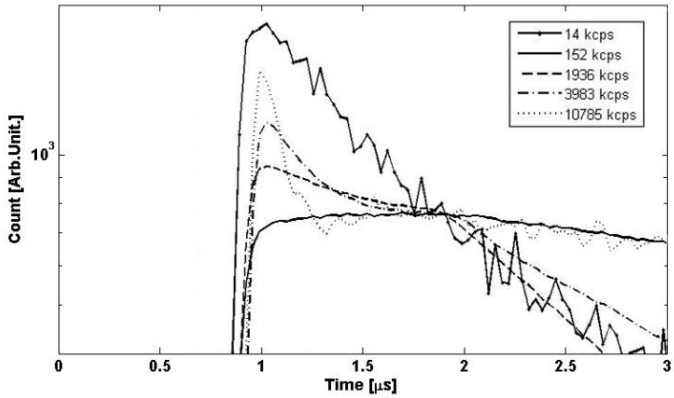

Figure 3-13: Time Interval Density distribution measured at various true count rates (approximately one per order of magnitude).

In order to evaluate the accord between the measured data and the expected data, the plot of the ratio of this two quantities is reported in Figure 3-14. Theoretical predictions have been calculated both using the hybrid model correction, and the simplest correction method of the dark count (d_0) subtraction. The dispersion of experimental data, in the low count rate regime, is due to the fluctuation of the temperature of the SPAD device and of the power supply of the light source. This fluctuation is greater than the afterpulse effect that is not considered in this circumstance.

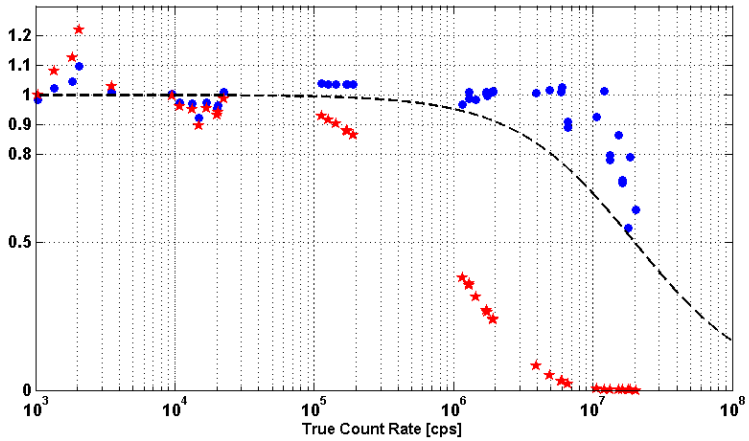

Figure 3-14: Calculated Counting Rate/True Counting Rate (ratio) vs True Counting Rate; circle, hybrid model correction; stars, dark count subtraction correction; dashed line, theoretical behaviour of SPAD with 50ns of Active Quenching.

3.7 Variance-to-Mean Ratio

For a perfect detector, without DT effects, the Poisson variance-to-mean ratio is a straight line at *y*=1. The introduction of the DT causes a decreasing of variance. This variance reduction depends on the measurement duration, and after a time three order of magnitude greater than the total DT of the system, the depletion reaches the asymptotic minimum value[33]. The relation between the variance and the count rate depends from the DT characteristics. According to [33] the asymptotic expression of the variance of hybrid model for equilibrium process is:

$$\chi_1 \equiv \rho\tau_1;\ \chi_2 \equiv \rho\tau_2;\ \lambda \equiv \frac{1}{1+\chi_1};\ g \equiv e^{-\rho(\tau_2-\tau_1)};\ \mu_{ne} \equiv \rho\lambda g;$$
$$\sigma^2 \cong \mu_{ne} t\left(1 - 2\lambda g\chi_2 + \lambda^2 g\chi_1^2\right) + \qquad (3\text{-}9)$$
$$+\frac{1}{6}\lambda^2 g^2\left(\lambda^2\chi_1^4 - 2\lambda\chi_1^3 - 6\lambda\chi_1^2\chi_2 + 6\chi_2^2\right)$$

Where τ_1 is the NP-DT, τ_2 is the sum of the two DT, *t* the time duration of the measure and ρ is the count rate.

In this frame we have compared the measured variance of our experimental data with the one predicted in the case of hybrid model. More precisely in the experimental data analysis we split the time acquisition in one hundred intervals, for each interval we calculated the output counting rate, and finally the mean and variance. Theoretical predictions have been calculated from Eq. 3-9 using, for τ_1 and τ_2 parameters, the values extracted in section 3.6.

Results are reported in Figure 3-15. It appears that the variance-to-mean ratio obtained accords very well with the theoretical predictions.

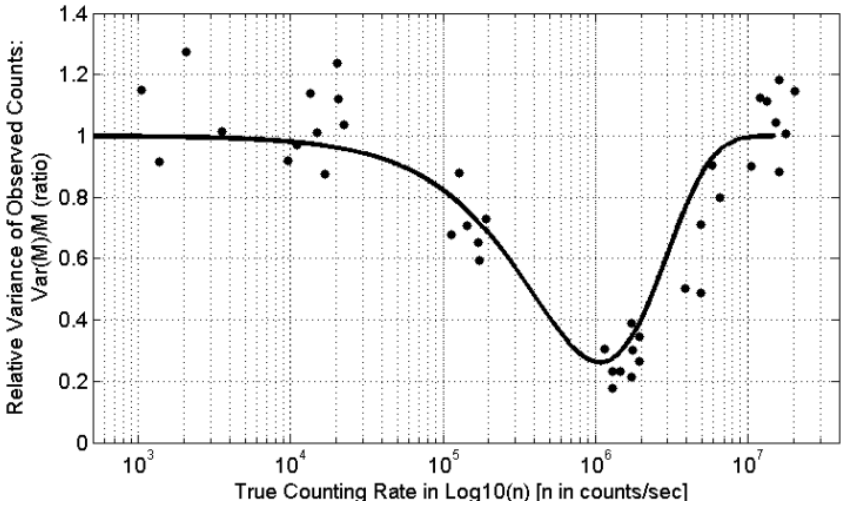

Figure 3-15: Variance-to-mean ratio comparison between experimental data (dot) and hybrid model variance theory Eq. 3-9 (line).

3.8 Comparison Between Passive and Active Quenching

To use the SPAD as counter two approaches can be followed, one is the use of passive quenched electronics with the data analysis shown in this chapter; the other one is the use of various active quenched electronics setup[12] to reduce the DT of the device. Generally speaking active quenching is a complex circuit that generates a short NP-DT which increases the count rate response of the device. To compare these two approaches, the best performance of commercial device (τ_{np}=50ns) was theoretically calculated according to Eq. 3-3 and shown in Figure 3-14. It appears that with active quenching device 10% of the signal is lost at a rate of $2.3*10^6$ cps while using our passive quenching device (total DT 970ns) with hybrid model correction the same losses are achieved at a rate of 10^7 cps. It is worth to note that the correction technique used for passive quenched device do not give appreciable advantage if applied to the case of active quenched device because this device shows only a NP-DT behavior, and the NP-DT response curve goes rapidly to a saturation level[30]. The comparison shows that the counting performance of this two approaches is approximately the same.

To choose which approach is better for a specific application we should evaluate the advantages and disadvantages of both approaches.

3.9 APD : Configuration without dead time

This chapter is focused on the dead time characteristics of SPAD device, and especially on the characteristics of passive quenching circuit configuration, that is subjected to a long dead time. Active quenching configuration, that produces a short and fixed dead time, has been also taken into account, but there is another configuration for the use of SPAD device introduced in chapter 1, the Avalanche Photon Diode configuration (APD). Such configuration can be named a “no dead time configuration”, it is useful for very high intensity source, provides real time information of light source time shape, and can be used for fast signals.

A SPAD device can be used in APD configuration simply reducing the voltage power source and removing the quenching resistor from the classical PQC configuration, as shown in the circuital scheme of Figure 3-16.

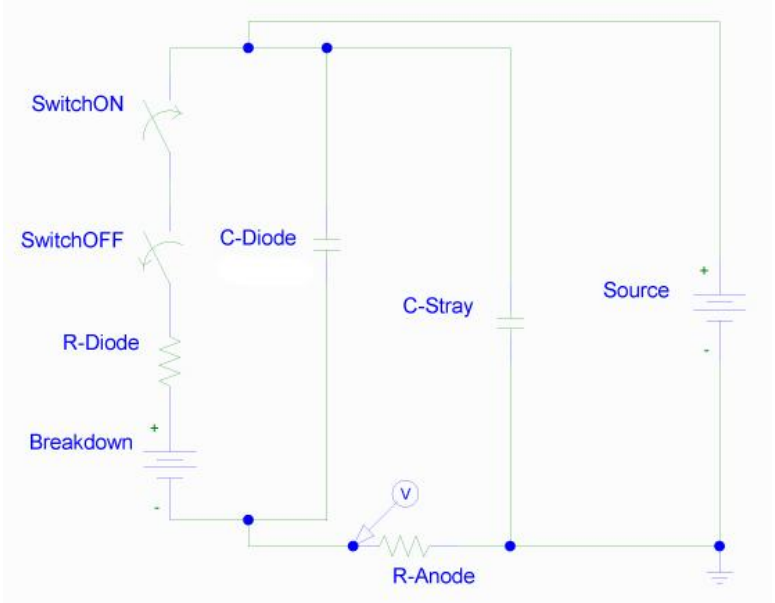

Figure 3-16: APD electric configuration for SPAD device.

3.9 APD : Configuration without dead time

On reducing the applied voltage below the breakdown value the avalanche multiplication factor goes below the self sustaining value, and each avalanche produced by the adsorption of a photon reaches only a multiplication finite factor. The result is a small output signal that is subject to high statistical fluctuations. If the incoming photon rate reaches a high value the sum of all small signals reaches a significant value and the detector produces a proportional detectable signal, with reduced statistical fluctuation.

To test the APD capability we used a light emission diode powered by a constant voltage of approximately -1 Volt and modulated in the light emission by the voltage pulse shown in Figure 3-17 with yellow line. The sign of applied voltage is due to the ground level chosen for the electric configuration, and do not means an inverse diode polarization. It is obvious that for the light production the diode is powered in direct polarization. The output signal coming from the APD configuration, reported in Figure 3-17 with magenta line, shows a thick succession of rapid signals, which are the output of each produced avalanche.

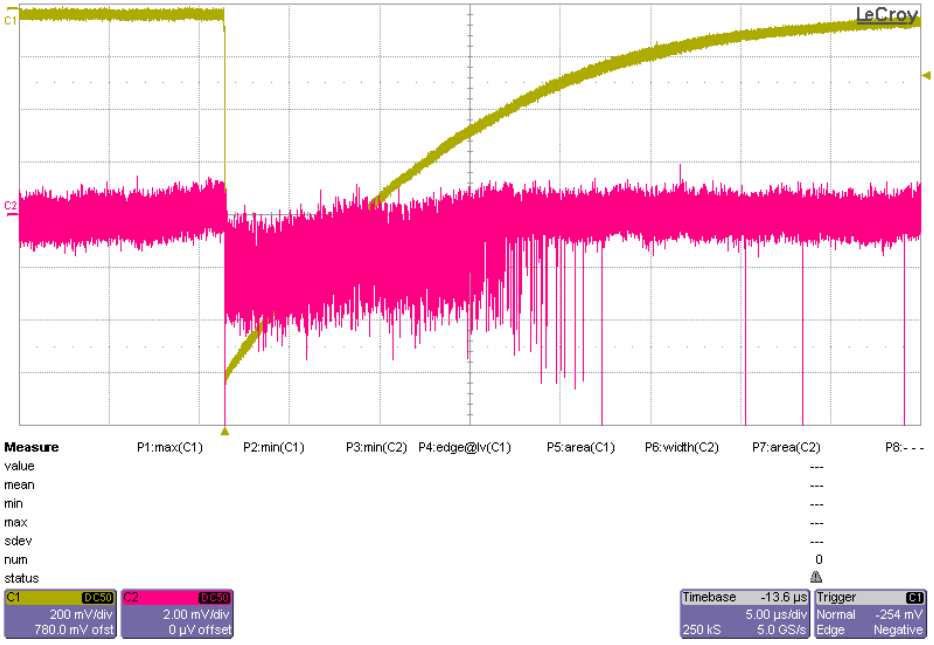

Figure 3-17: APD response subjected to high photon rate.

To extract from APD signal the real photon source shape we need to use a re-binning function. The oscilloscope makes a signal sampling with 20GHz sampling rate, so to obtain a good statistics we must reduce this sampling rate to few MHz. The result is shown in Figure 3-18. The integration is needed to obtain a macroscopic signal and to reduce the signal statistical fluctuation. Increasing the number of impinging photons increases the rapidity of the signal sampling. The MHz obtained time precision is an high value compared with the other photon sensors. Such device is also promising because is not subject to an overheating and cannot be damaged with too high photon rate. For our experimental test we do not perform a quantitative analysis but we can evaluate a rate of few thousand of avalanche in less than a tenth of microsecond, so the incoming photon rate is of the order of 10^{11} cps. Good accordance has been found comparing the re-binned APD signal and the modulating power pulse reported in Figure 3-18. The small mismatch, starting from 17 μs, is caused by the threshold level of the light emission diode. In fact the photon production is linearly dependent on the applied voltage until it overcomes the direct threshold voltage value, below this value the photon emission is zero. This is what occurs at 15 μs, the light drastically decreases, and the APD device follows this trend.

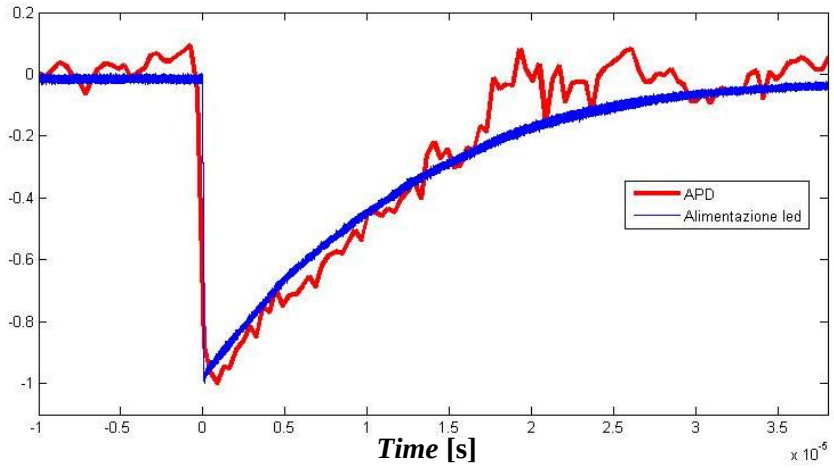

Figure 3-18: APD measurement of high intensity modulated light source.

3.10 Results

The scope of this PhD work is a imaging counting device based on SPAD technology. In this chapter counting characteristics of the SPAD device has been deeply analyzed. A correction technique has been developed for low and high rate working regimes. A simulation procedure and a dedicated experimental setup have been built up to verify all our results. We have been able to discriminate the low rate photon signals from afterpulse and noise production and, moreover, to overcome the saturation effect due to the DT losses.

We have developed the equation of the noise count rate vs. incoming photon rate, supported by simulation and experimental data. We have marked the difference between dark rate and noise count rate, and introduced the noise rate inside the hybrid DT equation used for SPAD devices.

We have been able to evaluate the real amount of incident photon rate up to 10^7 cps using a passive quenched device with 0.97 μs total DT. This has increased the maximum measurable rate value of more than two order of magnitude. In this way the passive quenched SPAD achieves the same performance of the active quenched one, showing that relatively complex data analysis and complex device implementation are comparable solutions for light measurement.

The active quenching strategy needs the development of a dedicated circuit that increases the fabrication complexity. This aspect, in a multiple devices configuration, as a two-dimensional imaging device, involves the decreasing of the fill factor, and the development of a readout strategy able to read the huge number of signals coming out from each diode.

The characteristic of the passive quenching strategy shown in this chapter is the simplest electric implementation: only a resistor per diode is needed. The data correction does not require an intensive computing operation and occurs only at high rates. Moreover in the array implementation the feel factor is not limited due to the simple electronics used. The DT losses of passive quenching strategy is negligible at low photon rate regime, while at high rate regime becomes an advantage because only a little part of the incident photons are translated into the signal that should be acquired, without overloading the external readout elec-

tronics. In any case using the shown correction technique we can evaluate the exact number of incident photons.

Disadvantages of this approach are the error in the determination and in the fluctuation of the DT parameters ($\tau_{np,}$ τ_p). However this error affects the final results with an error of few percent only at high rates regime. Another disadvantage is that this correction technique is not able to follow rapid changes in the photon flux; to solve this problem we began a more general study on the DT influence on the detection of non steady state sources. The obtained results are shown in the next chapter 4. We have chosen to separate these two chapters in order to underline that the generalization of the DT equations (chapter 4) can be applied to all devices subjected to any type of DT, while this chapter is focused only on SPAD devices.

4. Generalization of DT Equations for Time Dependent Sources

In this chapter we introduce the new equations for paralyzable, non paralyzable and hybrid DT models, valid for any time dependent source. We show how such new equations include the equations already used for constant rate sources, and how it's possible to correct DT losses in the case of time dependent sources. Montecarlo simulations has been performed to compare the equations behavior with the predictions of the three DT models and excellent accordance has been found. We also obtain good results in the experimental validation of the new hybrid DT equation. Passive quenched SPAD device has been chosen as a device affected by hybrid DT losses and active quenched SPAD with 50ns P-DT has been used as DT losses free device.

This results, deduced and verified for SPAD device, can be used for all the devices that suffer DT losses. For that reason we will focus, this chapter, not only on SPAD applications, but also on equation deduction, meaning, verification, and on the extension to other type of DTs.

4.1 Literature Time Dependent Approaches

The DT can be due or to the sensor device or to the electronics of the readout system. Theoretical studies of the DT behavior are often used to infer the real amount of count rate from the measured one[27]. The greater part of Literature has studied the DT influence on stationary sources[28], that is when the intensity variations of the source occurs in time interval order of magnitude longer than the DT of the counter device.

Some studies have analyzed short-lived time dependent source[34][35] but have been limited to the case of a well know shape dependency, for example in the case of decaying source with a single decay constant λ as:

$$n(t)dt = (b + s_0 e^{-\lambda t})dt \qquad 4\text{-}1$$

where n is the time dependent event rate, b is the constant background rate, s_0 is the starting pulse rate. Nevertheless there are many different types of source and many cases in which such sources are mixed together in a non-predetermined way or have a non-predetermined shape. The relevance of this problem motivates the developing of complex electronic systems for DT compensation, as reported in [36], but such complex solutions cannot be used in any condition.

With our theoretical approach it is possible to evaluate the DT losses only by using a data analysis process, apart from the time dependence of the source, and without the necessity of developing complex electronic systems. In this chapter we present three new equations that describe the time dependent effect of paralyzable, non paralyzable, and hybrid model DTs, and the accord of the equations predictions with simulations and experimental data.

4.2 New Dead Time Equations

4.2.1 Non Paralyzable Dead Time

As said, the signals that arrive during the NP-DT interval after a detected signal are lost. So in the case of NP-DT the total inactive time of the sensor can

be calculated by multiplying the measured count rate *m* and the DT extension τ_{np}. The losses count rate are the real incident rate *n* in the total inactive time. So in this case the measured count rate is related to the real incident rate by the equation:

$$m = n \cdot (1 - m \cdot \tau_{np}) \qquad 4\text{-}2$$

that can be rewritten as:

$$m = \frac{n}{1 + n \cdot \tau_{np}} \qquad 4\text{-}3$$

Eq. 4-3 is the commonly used equation to describe the NP-DT regime. This equation is valid for constant rate sources, while in the case of time dependent sources the count rate *m* and *n* are functions of the time. Starting from this consideration we determine an equation valid for a time dependent count rates.

We divide the total time in intervals of duration Δ and consider the average rate in each interval so obtaining two series of values m_i and n_i. With this time division the duration τ_{np} turns into a number T_{np} of intervals. For example, if it is τ_{np}=500ns and the interval duration Δ=10ns, then T_{np}=50. Since the NP-DT losses are due to the measured counts in the previous DT interval (τ_{np}), to evaluate the measured rate in the *i-th* interval we sum the contribute of all the previous T_{np} measured rate values. Due to the finite duration of the *i-th* interval we must also consider the DT losses inside the same interval. The count rate at the end of the interval suffers of the losses due to the previous rate measured inside the same interval, whereas the rate at the first part of the interval are not influenced by the following part of the interval. So, evaluating the average losses produced inside the interval, we obtain that the *i-th* interval must be considered like a source of DT losses, but half weighted. Applying these considerations to Eq. 4-2 we obtain:

$$m_i = n_i \cdot \left(1 - \left[\sum_{t=i-T_{np}}^{i-1} m_t + \frac{m_i}{2} \right] \cdot \Delta \right) \qquad 4\text{-}4$$

A deeper analysis of this equation allows to solve the problem of hybrid DT model. Inside the Eq. 4-4 we can separate the lost rate due to the NP-DT L^{np}

from the original true rate *n*, being:

$$m_i = n_i - L_i^{np} \Rightarrow L_i^{np} = n_i \cdot \left[\sum_{t=i-T_{np}}^{i-1} m_t + \frac{m_i}{2} \right] \cdot \Delta \qquad 4\text{-}5$$

The quantity L^{np} is characteristic of the DT type (*np*) and varies with the time position of the *i-th* interval. Eq. 4-5 shows that the lost rate is the incoming true rate multiplied by the probability of a measured event in the previous τ_{np} time interval.

4.2.2 Paralyzable Dead Time

Using the exponential distribution of time intervals between Poissonian random events occurring at a constant rate *n*, it is possible to show that the relation between measured rate and true rate in the case of P-DT is:

$$m = n \cdot \exp(-n \cdot \tau_p) \qquad 4\text{-}6$$

In the case of time dependent count rate the two values of the true rate *n* appearing in Eq. 4-6 are different: the first one represents the true actual rate, the latter represents the true rate in the previous time intervals, source of DT losses. Taking into account the contribute of all previous T_p intervals, and half weighting the *i-th* interval as in the case of NP-DT previously analyzed, we obtain the equation:

$$m_i = n_i \cdot \exp\left(-\left[\sum_{t=i-T_p}^{i-1} n_t + \frac{n_i}{2} \right] \cdot \Delta \right) \qquad 4\text{-}7$$

Where T_p is the number of intervals contained in τ_p.

As before, we can separate the lost rate due to the P-DT L^p from the original true rate *n*:

$$m_i = n_i - L_i^p \Rightarrow L_i^p = n_i \cdot \left(1 - \exp\left(-\left[\sum_{t=i-T_p}^{i-1} n_t + \frac{n_i}{2} \right] \cdot \Delta \right) \right) \qquad 4\text{-}8$$

4.2.3 Hybrid Dead Time

In the hybrid model, introduced by Lee and Gardner[31], the DT configuration is a combination of P-DT and NP-DT. In constant regime the relation between true and observed count rates for the this model is:

$$m = \frac{n \cdot \exp(-n \cdot \tau_p)}{1 + n \cdot \tau_{np}} \qquad 4\text{-}9$$

A detailed description and the derivation of this equation can be found in Ref. [31].

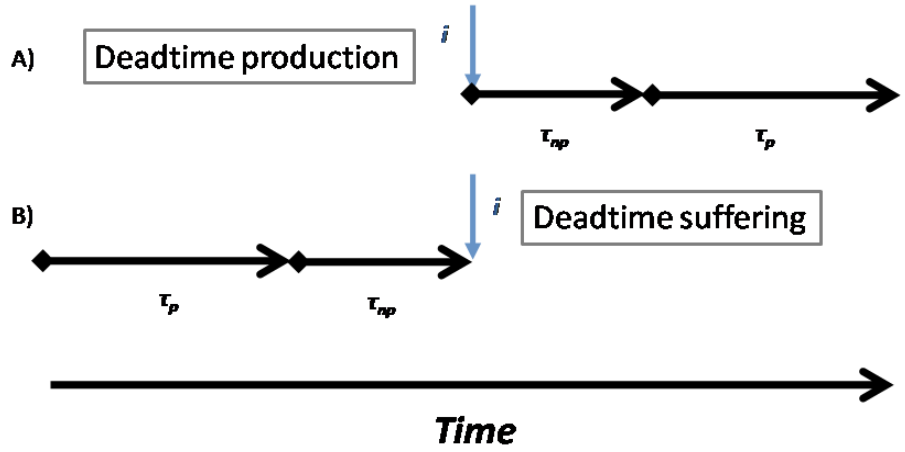

Figure 4-1: A) Structure of the two DT produced in a hybrid DT model; B) Time intervals rate that produces losses into the following *i-th* instant and type of DT losses actuated.

The count that arrives at the *i-th* interval generates a NP-DT followed by a P-DT, as shown in Figure 3-1A. The two DT durations could be different.

In the time dependent count rate, we must consider which previous intervals produce losses into the *i-th* interval and the type of the actuated DT losses. Due to the sequence of produced DTs reported in Figure 3-1B, the rates located inside the interval τ_p produce P-DT losses, while the rates located inside the interval τ_{np} produce NP-DT losses. Once identified the type losses produced by each previous interval we can write the equation for hybrid model valid for time dependent sources, starting from Eqs. 4-5 and 4-8:

$$m_i = n_i - {}^{*}L_i^p - L_i^{np} = n_i - n_i \cdot \left(1 - \exp\left(-\left[\sum_{t=i-T_{np}-T_p}^{i-T_{np}-1} n_t\right] \cdot \Delta\right)\right) - n_i \cdot \left[\sum_{t=i-T_{np}}^{i-1} m_t + \frac{m_i}{2}\right] \cdot \Delta$$

4-10

Note that the *i-th* interval generates NP-DT losses, so it must be considered only in the non paralyzable part of the equation. The symbol "*" indicates that last *i-th* term of Eq. 4-8 is not considered.

4.2.4 Relation Between Non Steady-State and Steady-State Equations

The non steady-state equation must be valid also in the steady-state, therefore imposing the steady-state condition in the Eqs. 4-4, 4-7 and 4-10 we must obtain the Eqs. 4-2, 4-6 and 4-9 respectively.

In fact, in steady-state conditions, m_i and n_i are constant series so their sum becomes the constant value multiplied by the number of repetitions and this multiplication factor times the time interval Δ gives the DT extension of the steady-state equation, τ_{np} or τ_p. Moreover the size of the time interval (Δ) can be chosen as short as possible, so, using the time precision of the readout system, the losses produced inside the *i-th* interval should not be considered, because we cannot distinguish the first part of the interval from the second part of the interval. So, vanished the reason that introduce this term, vanishes the term.

For the sake of clarity the mathematical steps that give Eq. 6-9, starting from Eq. 4-10, are shown below:

$$m_i = n_i - n_i \cdot \left(1 - \exp\left(-\left[\sum_{t=i-T_{np}-T_p}^{i-T_{np}-1} n_t\right] \cdot \Delta\right)\right) - n_i \cdot \left[\sum_{t=i-T_{np}}^{i-1} m_t + \frac{m_i}{2}\right] \cdot \Delta \Rightarrow$$

$$m = n - n + n \cdot \exp(-n \cdot \tau_p) - n \cdot m \cdot \tau_{np} \Rightarrow$$

$$m = \frac{n \cdot \exp(-n \cdot \tau_p)}{(1 + n \cdot \tau_{np})}$$

4-11

4.3 Montecarlo Simulations

As described in section 3.1, a Matlab code has been performed to simulate the behavior of the three DT types. We found that, in this simulation approach, a sharp increase of the illumination from zero to a constant value, gives valuable information about the DT losses and the equation validity (Figure 4-2). The predictions of the three proposed equations (Eqs. 4-2, 4-5 and 4-8) have been compared with the results of the simulation.

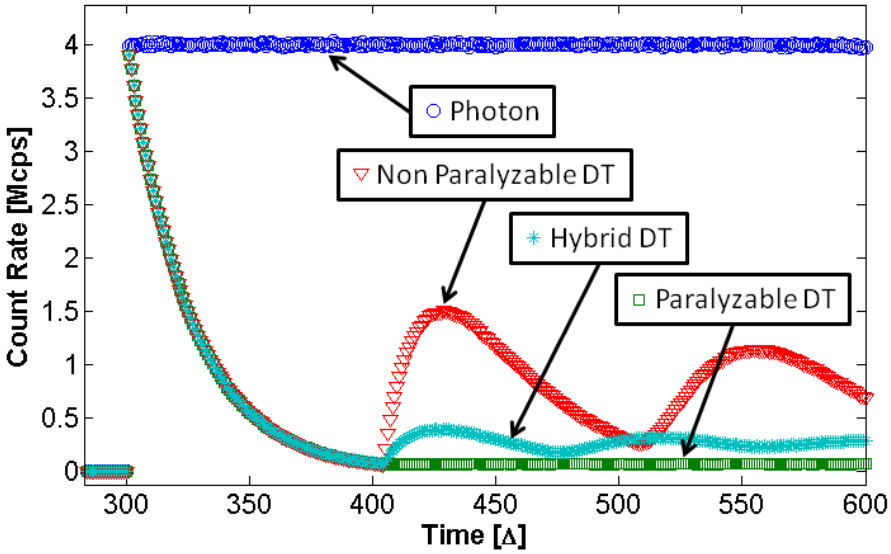

Figure 4-2: Histograms of rate vs. time; blue circle, simulated photon source rate; dark green square, P-DT model simulation; red triangle, NP-DT model simulation; cyan asterisk, hybrid DT model simulation.

We have chosen that the illumination value started with zero value and remained zero for a time interval longer than DT. In this way Eqs. 4-2, 4-5 and 4-8 can be calculated in an iterative mode ($i=t_o$, $i=t_o+1$, $i=t_o+2$,…), starting from the end of a zero illumination period, characterized by previous measured m_i and true rates n_i both equal to zero.

Montecarlo simulation uses the Poisson statistics to generate the source count distribution, and the DT laws to determine which counts are measured and which counts are lost (chapter 3). In the zero illumination zone no count is introduced. In the constant illumination region a Poisson distribution was used to ex-

tract the random values of photons that should arrive into the illumination time window. The time position of these photons was randomly chosen inside the illumination time window. The histogram of the simulated photon count rate is showed in Figure 4-2. For the three DT types simulated, the DT laws are used to determine the counted photons, the lost photons that arrive into DT, and the photons that produce or extend DT. As in the experimental setup, 10^6 acquisition windows have been simulated. The histograms of this three DT simulations are reported in Figure 4-2. The time unit of the simulation is the interval duration Δ=10 ns, the total DT extension has been chosen of 105 Δ for all three simulations.

In Figure 4-3 we show the agreement between the simulations and the data calculated with the Eqs. 4-2, 4-5 and 4-8. The confidence is better than expected, being deviation less than 0.2%. The trends predicted by the equation are not plotted in Figure 4-2 because they overlap the simulation data.

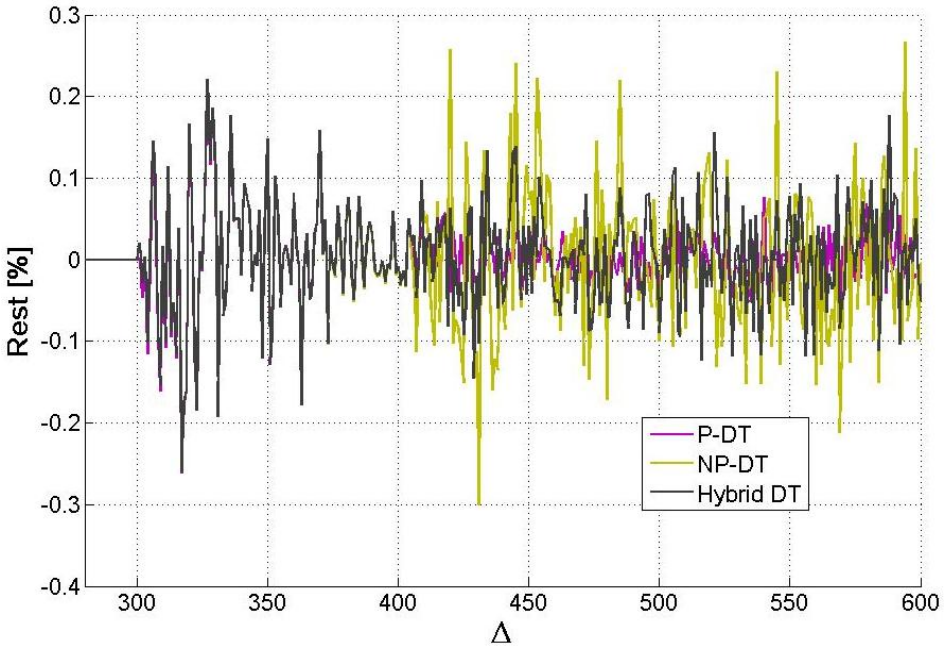

Figure 4-3: Mismatch between the prediction of the three Eqs. 4-2, 4-5, 4-8, and the three simulation results shown in Figure 4-2.

In the simulation, the first 300 Δ are defined without photons, after that the illumination source starts with a constant rate. In the following 105 Δ, corresponding to the total DT duration, the shape of the three DT types are the same, because in this period, independently from the type of the occurring active DT, only one photon can be detected. Therefore this first part of the histogram shows the arriving time position of the first photons. This exponential decaying trend represents the probability to have no photon in illumination condition. This probability drastically decreases on increasing the time. After a time equal to the total DT, the differences between the three type of DTs generate changes in the shape of the curves. The P-DT, that takes into account all lost counts, shows a constant output rate, due to the constant lost incoming rate. The NP-DT shows an increase of counts due to the end of the DT of the first measured count, not extended by the others photons. The hybrid model shows an intermediate behavior in comparison to the two fundamental DT types, according to the proportion of the DT components of hybrid model.

The P-DT reaches the steady-state value of Eq. 4-4 after the first DT period, while the other DT types need few DT periods to reach their steady-state values, predicted from Eq. 4-1 and 4-7. This is an important confirmation of the good quality of simulation.

4.4 Experimental Validation

4.4.1 Materials

The goal of our study is to extend the dynamic range of our imaging device developed by using SPAD technology[9], and, in particular, passive quenched SPAD. The diodes used have been previously described[37], the DT configuration is hybrid model like, the total DT is 970ns, 660ns NP-DT and 310ns P-DT. As a reference counter a commercial active quenching device with 50ns of NP-DT was used. As a matter of fact at the maximum rate used in our experimental setup this device can be considered free from losses.

We realized a modulated light source using a commercial Light Emitting Di-

ode (LED) powered by a pulse generator, model PB-4. The shape of the light source obtained is defined by an exponential grow, with a selectable characteristic time between 0.05μs and 10μs, and an exponential fall down with a selectable time between 0.5μs and 1ms. Both counter devices were contemporaneously enlighten by the same amount of light. The duration of the acquisition was 35μs and, to increase the statistics, about 10^6 run have been performed. The readout system has been designed to obtain an histogram of the measured count rate vs time, with a time bin of 10ns, even if the acquisition time precision is 0.1ns.

4.4.2 Validation

To test the features of the proposed new hybrid DT Eq. 4-8 we used a LED powered by a voltage which grows according to an exponential shape with a 0.05μs time constant, and that falls down with a 100μs time constant. The maximum photon rate that hit the detectors was about 500kcps. The test device was a passive quenched SPAD with a measured 970ns total hybrid DT[37]. In a constant illumination setup, at 500kcps of photon rate, this device would be affected by 35% of losses. Instead the active quenching SPAD device, with a DT of 50ns, at this rate can be considered free from losses, and it was used as reference counter.

Exposing the test device to a time dependent source we observed that the behavior changed with time. At the beginning the device was affected only by the negligible DT losses produced by the previous darkcount rate, 1kcps, so the measured rate was very close to real one. Immediately after the measured rate fell down for the DT losses produced by the first detected rate. When the DT losses production reached the maximum value, the measured rate continued with a slope different from that produced by the reference counter.

The Eq. 4-8 describe the relation between the true and the measured photon rates. Starting from the Eq. 4-8 it is possible to extract the equations of real count rate and measured count rate, as a functions of previous true and measured count rates:

$$n_i = \frac{m_i}{\exp\left(-\left[\sum_{t=i-T_{np}-T_p}^{i-T_{np}-1} n_t\right]\cdot\Delta\right)-\left[\sum_{t=i-T_{np}}^{i-1} m_t + \frac{m_i}{2}\right]\cdot\Delta} \qquad 4\text{-}12$$

$$m_i = \frac{n_i\cdot\left\{\exp\left(-\left[\sum_{t=i-T_{np}-T_p}^{i-T_{np}-1} n_t\right]\cdot\Delta\right)-\left[\sum_{t=i-T_{np}}^{i-1} m_t\right]\cdot\Delta\right\}}{(1+n_i\cdot\frac{\Delta}{2})} \qquad 4\text{-}13$$

Assuming that during the dark state the count losses can be neglected, it is possible to evaluate the real true rate from the measured one using the Eq. 4-12 and, vice versa, the measured rate from true one using the Eq. 4-13. In Figure 4-4 we compare the reference true rate with the predicted one using Eq. 4-10, and the measured rate affected by hybrid DT losses with the predicted one using the Eq. 4-13.

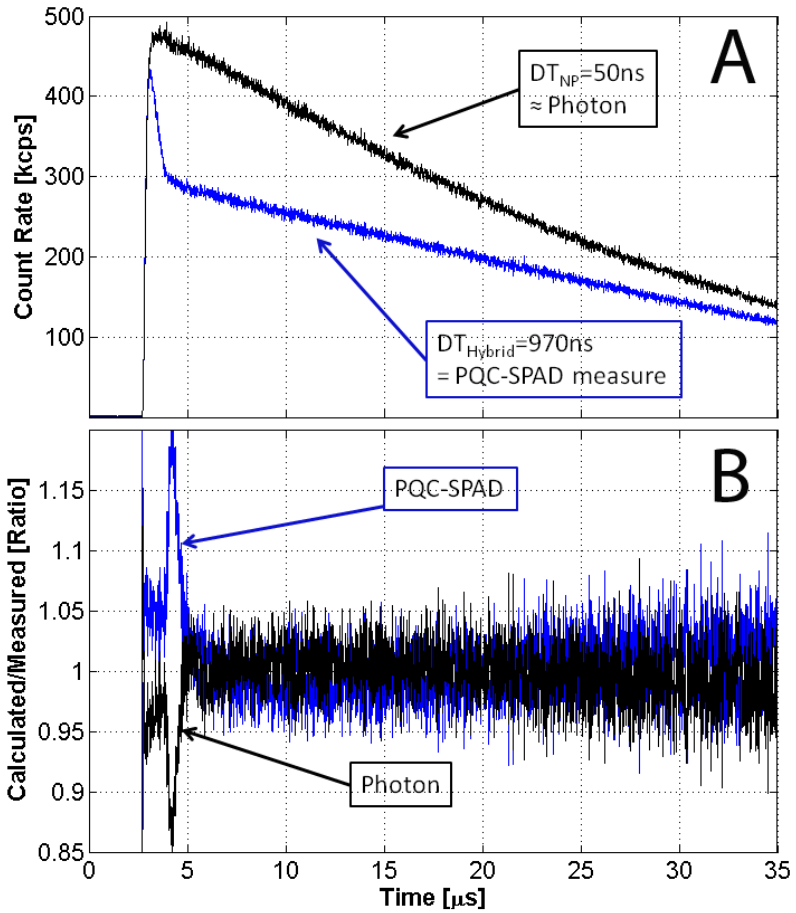

Figure 4-4: A: black, true count rate, measured with active quenched SPAD; blue, measured count rate that suffer Hybrid DT losses (passive quenched SPAD). B: Comparison between calculated rate and measured one; blue, calculated with Eq. 4-13; black, calculated with Eq. 4-12.

As Figure 4-4B shows, the difference between predicted and measured rate are in the first part of the light pulse because, due to the rapid change in the excitation rate, the device doesn't show exactly the hybrid DT behavior but something close. After a time twice the DT duration the predicted and the measured rates show a very good agreement, being deviation less than 5%.

4.5 Results

The presented new approach for evaluating DT losses shows how the two elementary DT types and their combination work with time dependent sources. The theoretical derivation, the completely accordance with the Montecarlo simulation, the inclusion of classic DT equation, and the experimental validation are a well-round presentation of this three new equations, that could be useful in all counting system devices and applications. Worth to note, our DT compensation technique requires only a simple data analysis process, regardless of the type of time dependent source and without the necessity of developing complex electronic systems.

Our theoretical approach can be also useful to deduce new equations for other series or parallel combinations of P-DT and NP-DT. The presented equation can be also used to predict the behavior of many devices in time dependent application, so allowing to select the most appropriate device.

In particular we plan to use this technique in the development of a new, time resolved, single-photon imaging sensor (TRIS), which uses passive quenched SPAD devices and shared readout channels for many diodes. Using a passive quenched SPAD device, instead of active quenched one, we increase the fill factor of the device and using the presented correction technique we take advantage from the DT losses that characterize this device. In fact, especially in scared readout configuration, the reduced measured rate due to the DT losses allows to not saturate the readout electronics.

5. SPAD Imaging Device

Since the introduction of solid-state optical sensors, the main trend has been an increase in pixel density at lower costs and higher miniaturization. Frame rate has been a concern until video rates could be achieved. Until recently, fast cameras have been relegated to niche markets in science and entertainment. However, as soon as higher-than-video speeds have been available, new previously unthinkable applications have emerged, like time resolved x-ray diffraction studies or Particle Imaging Velocimetry (PIV). The extreme limit of the high frame rate is the measurement of the arriving time of all impinging photons, this means extreme sensibility and extreme time precision. Especially in biological applications high sensibility became a requirement until the limit of single photon sensibility, for the analysis of little biological systems like cell membrane, Single Molecular Fluorophores for Cellular Imaging (SMFCI), night-vision, and natural biological fluorescence. Many physical information are obtained using Time Correlated Single Photon Counting (TCSPC) where the single photon and high time sensibility are the main constrains. Time sensibility became necessary also in coincidence analysis, like Positron Emission Tomography (PET), and in multiphoton microscopy. Light emission time distribution is also important for Fluorescence Lifetime Imaging Microscopy (FLIM), and 3D-camera became achievable measuring the light reflection delay with a precision of picoseconds[5].

The main objective of this PhD work is to study better solution to achieve sub nanosecond time precision and single photon sensibility in a low coast imaging device by using SPAD devices and the cross-wire readout schema. Our approach is study without focusing on a particular application but evaluating the top performance achievable to compare this performance with those of other dif-

ferent approaches and with the applications requirements.

5.1 State of Arts of Time Resolved and High Sensibility Approaches

In the technological evolution of fast cameras and high sensibilities cameras many strategy were chosen. Different approaches have shown different peculiarities, some of them start with a good time resolution and with some difficulties reach acceptable spatial resolution, others approaches start with single photon sensibility but with great difficulty rise a good fill factor, others system, finally, have high spatial resolution but bad sensibility and timing performance. Moreover the best performance of each approach and the total cost of the technique should be compared with each specific applications requirements and budget availability.

Charge-Coupled Device (CCD) technology is mature. In CCDs, photo-charges are accumulated into a capacitance, the charge associated with every pixel is then line-wise transferred to the exterior of the pixel array using elaborate mechanism. The main limitation for a sustained high frame rate in CCDs is the quick and continuous transfer of photo-charges across the entire pixel array. Analogue amplification, sample-and-hold (S/H), and analogue-to-digital (A/D) conversion may contribute further to slow CCDs down. The advantages of this technique are the good fill factor and the little size occupied by all the electronics needed. The disadvantages are the limit in the photon sensibility, and the high noise due to the thermal generation and to the charge transfer and conversion processes.

There are different high cost implementations of CCD camera that improve the achievable frame rate, one of them is the In Situ Storage Image Sensor (ISI) that is equipped with typically one hundred of in situ CCD memory elements, which enable 120 consecutive images with a frame rate up to one Mega frame per second. This technique is really amazing for some analysis, but do not represent a real high frame rate camera solution.

The Photon Multiplier Tube (PMT) is based on the photoelectric effect and

on a multiplication process achieved by in vacuum acceleration throw a sequence of dynode. This technique react high efficiency in the detection of the single photon and in the arriving time measurement, but encountered many problem in multi pixel implementation, because the assembly of many PMT into one single device is very inefficiency. In some extreme product it is possible to see PMT with a anode fragmentation for the detection of the impinging photon position, but the number of achievable pixels is less than ten.

The compact version of the PMT multiplication process, enabled by the research in science materials, is the Micro Channel Plate (MCP) technology, in which the micro channels act like the dynodes of the PMT. This technique can be used in many ways to implement a particle or a photon detector. The time resolved photon imaging can be obtained with a fast gated version of MCP coupled with a phosphor screen to convert the electron avalanche into photons collected by a CCD camera for the position identification. In the opposite direction it is possible to release the time precision, without implement a gated power source, to obtain a continuous CCD camera version with single photon sensibility, but with the low time precision of the phosphor screen used, and with the typical noise of the CCD.

As an alternative to PMTs and MCPs, researchers have studied solid-state photon counters based on avalanche photodiodes (SPADs). The same avalanche concept of PMTs MCPs this time act in the atomic scale with multiple impact ionization process. Silicon SPADs have recently attracted significant interest thanks to their relative simplicity and ease of fabrication. There are two main lines of research in silicon SPADs: one that advocates the use of highly optimized processes to boost performance and one that proposes to adapt SPAD design to existing processes to reduce cost and to maximize miniaturization. Both approaches have advantages and drawbacks. The first one has been chosen by our research group, because, in principle, is capable of best performance but need of a lot of work to find solutions to many problem. The second approach uses CMOS processes and is the one that can potentially enable shorter time-to-market using the maturity of CMOS technology.

In CMOS SPAD systems, the photocurrent of a diode, formed at a p-n junc-

tion, charges a parasitic capacitance. The resulting voltage is amplified, sampled, and A/D converted, stored, by in pixel electronics. The first limitation comes from the in pixel analysis approach that require the design of readout circuit between pixels, this drastically reduce the fill factor of the sensor. The other limitation comes from a non continuous sensitive approaches, that require a break for the sensor readout. There is not a single photon detection but a single frame detection with a single photon sensibility, that means the number of photons collected on each pixel and for each frame. As consequence the arriving time of each photon is not registered, because the time precision is limited to the time size of the frame. The other limitation is that is not possible to obtain a continuous photon acquisition without dead time between frames, because the time period spent for the data transmission. However the conventional cameras, based on CMOS SPAD, can reach today speed of a few thousand frames per second (fps) and enable big number of pixels in the same sensor, tacking place in a large number of demanding applications.

Our project born from the opportunity to made in collaboration with ST-Microelectronics a time resolved single photon imaging sensor able to satisfy the more restrictive needs of frontiers imaging research. The Catania R&D group of ST-Microelectronics own one of the best SPAD fabrication process with top performance actually available. Their approach, different from CMOS technology, enable to obtain high performance SPAD but limited possibility to include any type of read out circuit. Taking into account the capability of CMOS SPAD technology we moved towards objectives that are forbidden for this approach. The single photon sensibility is strengthen increasing the photon detection efficiency, with the increasing of fill factor, reducing the on-pixel readout circuit, and bringing out of the matrix the signal processing, taking care to preserve the sensor detection activity during the readout operations. The timing performance is not only an application requirement that with our sensor we want to satisfy, but is the most important requirement for the operation conditions of our sensor readout approach. So this feature has been stressed as much as possible. Our time precision is not the frame time length, but the arriving time of each photon captured by each pixel. Such big amount of information, obtained summing the

time and the spatial positions of each arriving photon, must be correctly extracted from the sensor without interrupt the photon detection activity. The technological solutions studied to solve this problem are among the main goals of this PhD work.

5.2 Innovation in Matrix Design

In the row lecture adopted by the CCD technology and by the CMOS SPAD device the big number of pixel are read in a scanning sequence that take into account one row at a time. There is a readout circuit per column, so the complexity increase with n, where n in the number of pixel for side of a square matrix. The reading time is not negligible and decrease the time in which the sensor is active. In each pixel of CMOS SPAD imaging device there are also some electronics circuits needed for the active quenching of the diode, the digital signal extraction, a counter, a memory element, and buffered readout circuit. This electronics drastically decrease the fill factor and increase the complexity of the matrix manufacturing.

Our approach bring out of the pixel all the readout circuits with the objectives to increase the fill factor, to simplify the matrix design and the fabrication procedure, and to remove the time needed for the scanning sequence of the matrix. In our approach the electronic elements inside each pixel are only one diode and one quenching resistor, the signals are extracted and analyzed out the matrix for each photon, without matrix dead time. With such requirement, for a square matrix of n^2 elements, the external readout circuits should be n^2. We found two solutions to jump the obstructive problem caused from a so rapid increase of complexity [22]: the avalanche signal is extracted from both side of the diode, the anode and the cathode; all electric anode contacts are shared with all diodes of the same row, and all electric cathode contacts are shared with all diodes of the same column. In such a way we obtain a matrix from which we can deduce the position of the diode hit by the photon, with complexity that grows as $2n$ instead of n^2. The name by which is commonly called this configuration is “cross-wire”. Hardware complexity is replaced with software complexity, in fact a re-

constructing algorithm was required to use the time correlation between row and column signal and to find the position of the stricken pixel.

The photon hits one of the SPAD of the matrix, generates two signals, one collected from the row contact and the other from the column contact: the promptly propagation of the signals gives the exact time and spatial information about the arrived photon. The Figure 5-1 shows the innovative electric pattern of the sensor. The matrix scheme is simplified to a square matrix of nine elements. The anode contact shared along the rows are blue, while the cathode contact shared along the columns are in red. The red circle identify the diode in the conductive state, and the yellow line the current flux. The signals produced in the readout channels (in this example ch=1 and ch=3) give the information needed for the reconstruction algorithm to identify time and position of the incoming photon.

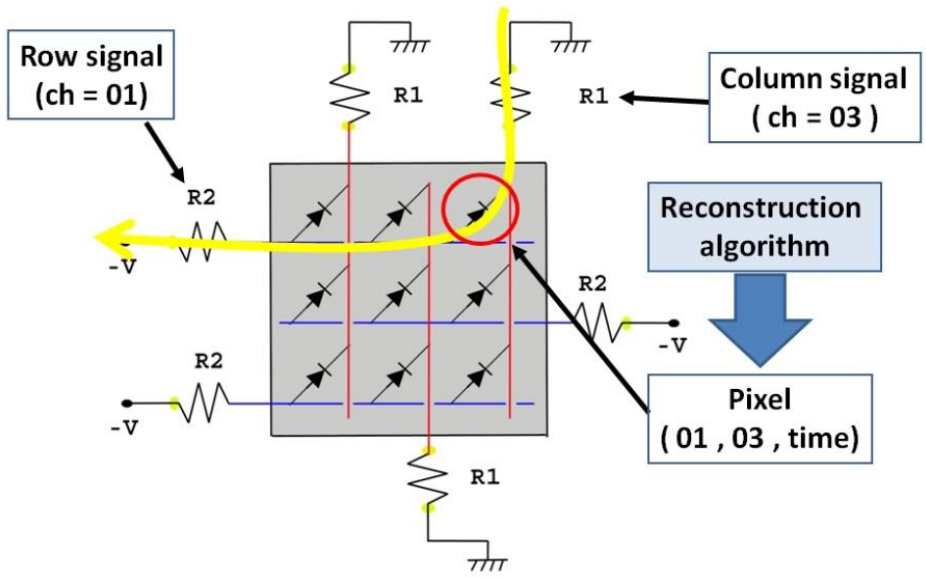

Figure 5-1: Simplified electric pattern of the SPAD-Matrix, shared row contact between anodes, and shared column contact between cathodes, hit SPAD generate signals in row=1 and in column=3, so it is in the position=(1,3) of the matrix.

5.3 SPAD Imaging Device Fabrication

During the collaboration between my INFN-LNS research group and STMicroelectronics Catania R&D team many prototype devices was produced. Many single SPADs and many two-dimensional array structures have been tested. A square matrix of one hundred elements was selected in order to develop the readout electronics and the software acquisition algorithm. Even if the fabrication process produce has improved the following products, in this chapter we describe the device used as a proof of our innovative SPAD imaging concept.

The vertical structure of the Single Photon Avalanche Diode used, fabricated by standard silicon planar technology at the STMicroelectronics Catania R&D clean room facility, is illustrated in Figure 5-2. The photodiode active area is defined by the metal ring used to contact the N^+ thin polysilicon layer doped with arsenic. A P^+ boron enrichment diffusion defines the high-electric field active region. The anode of the device is contacted by the P^+ sinkers created all around the photodiode active area by means of a high-dose boron implantation step, in order to reduce the contact resistance of the anode and provide a low resistance path to the avalanche current. An external ring doped by a heavy $POCl_3$ diffusion, realized through an oxide mask on the topside of the wafer, provides local gettering sites to reduce the defectivity in the device active area and consequently the dark count rate. Finally thin optical trenches, filled with oxide and metal, surround the pixel active area, to avoid electro-optical coupling effects (cross-talk) between adjacent pixels in SPAD arrays [19]. The device has a thin junction depletion layer (about 1μm) and a reduced dead layer thickness above the active area in order to minimize the loss of photons in blue-near ultraviolet wavelength ranges.

5.3 SPAD Imaging Device Fabrication

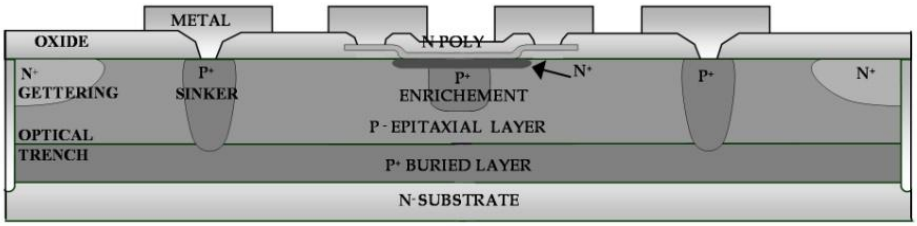

Figure 5-2: Schematic cross-section STMicroelectronics SPAD single pixel.

A schematic overall view of a 10×10 SPAD array used for imaging is shown in Figure 5-3. Single pixel active area diameter is 60µm while the separation distance between neighboring pixels is 245µm.

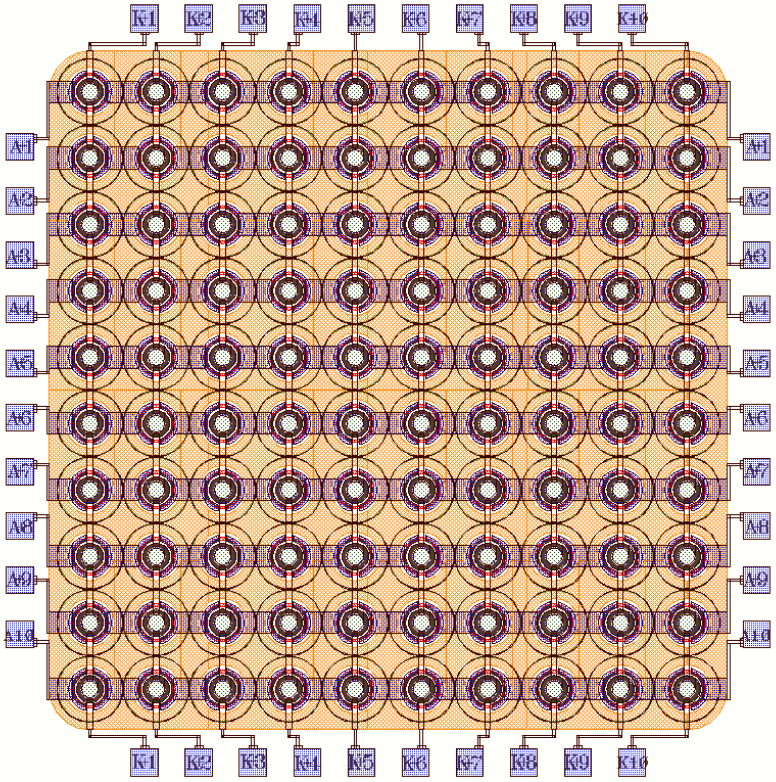

Figure 5-3: Layout of a 10×10 60µm diameter active area SPAD array.

Our strategy required common anodes contacts along rows and common ca-

thode contacts along rows. Unfortunately only one metal deposition was used in this prototype, so the metal strips used to contact the cathodes in each column are continuous while those used to contact the anodes in each row are interrupted in proximity of each cathode metal bus to avoid short-circuits with cathode metal strips. The conductivity has been guaranteed by a high doped silicon underpass. The metal strips and the underpass are shown in the Figure 5-4. This underpass, unfortunately, created a metal-HighDopedSemiconductor-metal electric device that, made only small changes in the signal propagation. The effect introduced, multiplied by the number of columns can degrade the transmission functionality. The result is that the technology process must switch on a two metallization flowchart to enable big size matrix devices fabrication. A scanning electron microscopy and an optical microscopy top view image of a 10×10 SPAD array is reported in Figure 5-4.

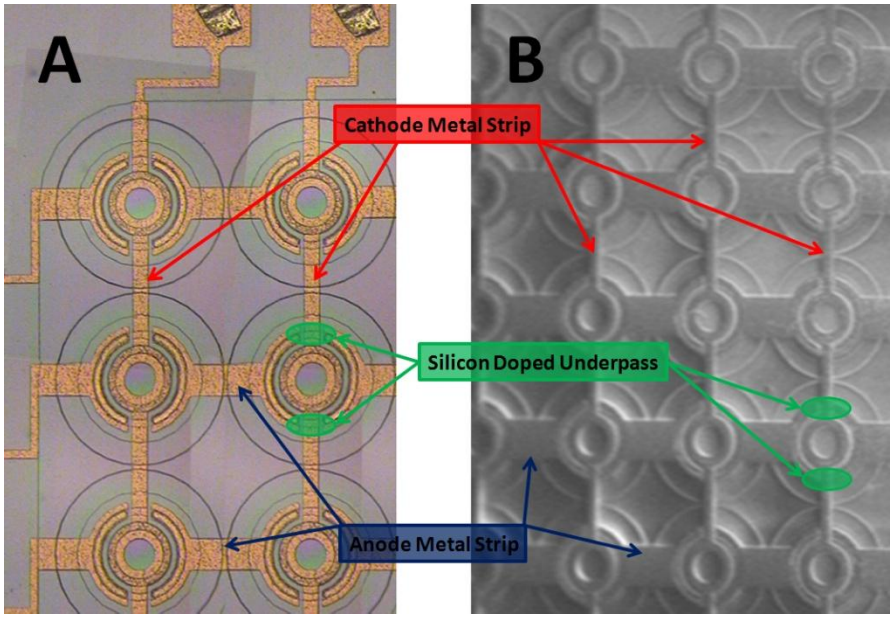

Figure 5-4: Optical Microscopy (A) and Scanning electron microscopy (B) top view image of a 10×10 SPAD array detail.

5.4 Front-End Electronics

Our approach for the read-out the SPAD-Matrix required two signals for each SPAD, one from the anode and the other from the cathode of the diode. In the Figure 5-5 there are shown the elementary circuit used for every diode of the matrix. The used power configuration set to ground level the anode and connects the cathode to the voltage supplier. For the quenching of the diodes we choose the simplest method, a passive quenching system implemented with a 300KΩ resistor connected to the cathode. As said, inside the SPAD matrix prototype used there are only the diodes, all the other elements are putted out. As shown in Figure 5-3, the matrix contain forty electric contacts, two for each anode and cathode strips. We can consider ten contact for the ten row/anode strips, and ten contact for the ten column/cathode strips. The two dots in Figure 5-5 represent the ten anode contacts and the ten cathode contacts. So anode's side there are ten 50 Ohm resistors and ten anode amplifiers, and on the other side there are ten 0.5 pF capacitors, 300K Ohm resistors and cathode amplifiers.

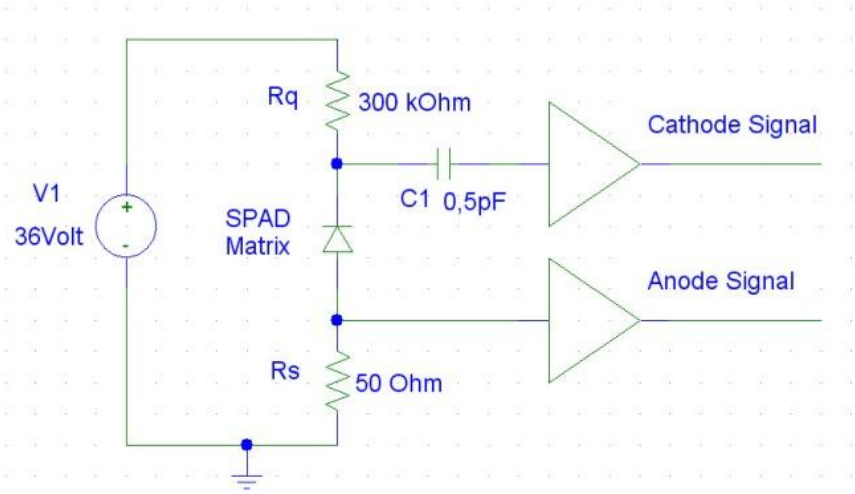

Figure 5-5: Simplified circuit connection for the diodes of the SPAD-Matrix.

The small 50Ω resistor (Rs in Figure 5-5 and Rin in Figure5-6) connected to the anode generates a signal that can be collected from the anode without modify

the diode behavior. The amplifier schema showed in Figure5-6 was developed in accordance to the anode signal characteristics and to the time requirement of the application to amplify and invert the polarity of the signal.

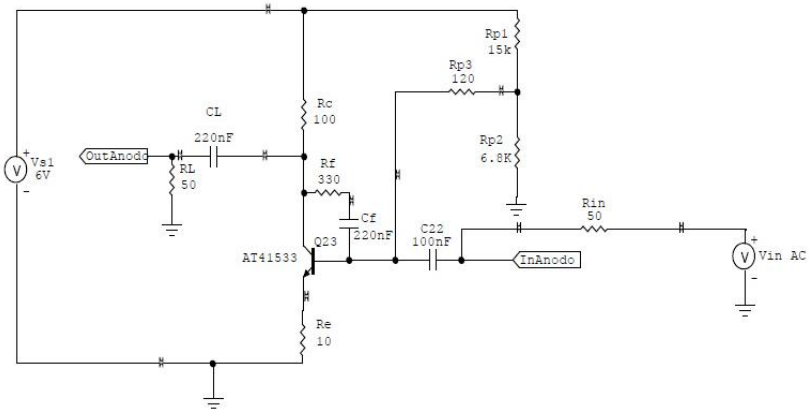

Figure5-6: Anode Amplifier Circuit used in the matrix readout board.

The capture of the cathode signal isn't simple like the anode one. We need to cut off voltage level from the power source to the ground level, with the littlest possible increasing of system capacitance, that means with the littlest degradation of timing performance. The capacity (C1 in both Figure 5-5 and Figure 5-7) used is only 0.5 pF so the out coming signal must be amplified. Figure 5-7 shows the read out cathode schema, expressly designed and performed for the purpose.

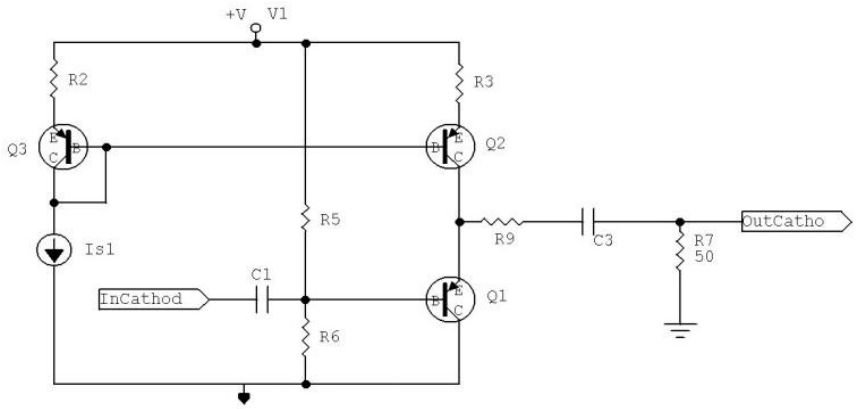

Figure 5-7: Amplifier circuit designed to extract the signal from the cathode.

Its structure is a BJT PNP emitter follower stage biased with the Is1 current by Q2 and Q3 current mirror. The PNP follower has been chosen in order to have a good tracking of the falling edge cathode pulse. The R2 and R3 resistor increase the output impedance of the mirror circuit. The R5 and R6 resistors set the operating point voltage of Q1 base. The SPAD cathode is AC coupled to the buffer thanks to the C1 capacitor. C1 has a value of 0.5pF. In this way the increase of the equivalent SPAD cathode capacitor load is negligible, and the original cathode response is preserved. Moreover the R5, R6, C1 values determine the high pass filter frequency pole of the buffer, and set the derivative voltage response of the SPAD, obtaining in this way a narrower cathode pulse at the buffer output. The output impedance is set to 50Ω.

In Figure 5-8 the comparison between the signals from anode and cathode is shown. The two signals differ both in amplitude and time constant. For the time resolved image the information of the arrival time of the photons is chipped from the anode, that show best timing performance.

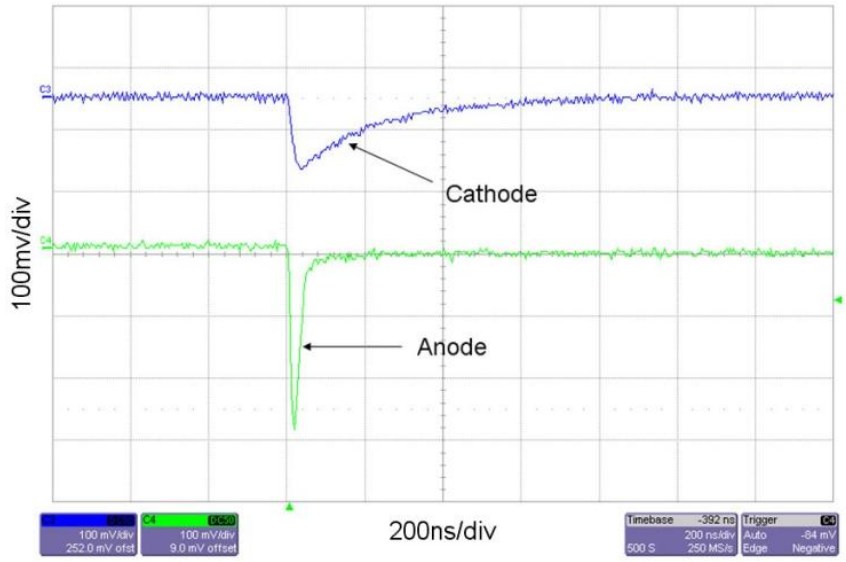

Figure 5-8: Comparison between the anode and the cathode signals extracted from the SPAD-Matrix and amplified by the designed electronics.

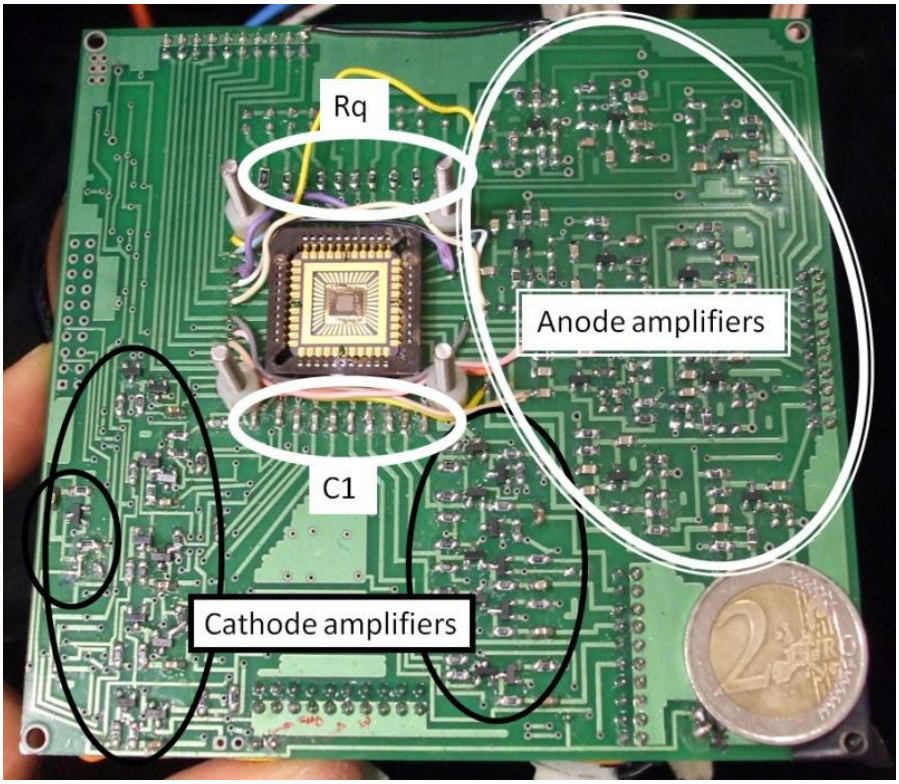

Figure 5-9: Imagine of the board that encloses the SPAD-Matrix and the amplifiers used for the reading of the anode and cathode signals.

Figure 5-9 is an image of the board that couples the SPAD matrix with the optics systems and the front-end electronics. It is possible to see the four screw for the mounting of optical system, the ten quenching resistors Rq for the ten rows, the ten capacitors C1 for the ten columns, and the amplifiers.

Standard nuclear electronics, based on VME modules Constant Fraction Discriminators (CFD) and Time to Digital Converters (TDC) have been used to analyze outgoing signals. The CFD marks the starting time of the analogical input signal and produces a digital signal with the rise time correlated with the input arriving time. The multichannel TDC measures the time distance between a reference time signal and the arriving times of the digital signal. This numerical information is send to a personal computer in which the information are elaborate to extract the time resolved single photon image.

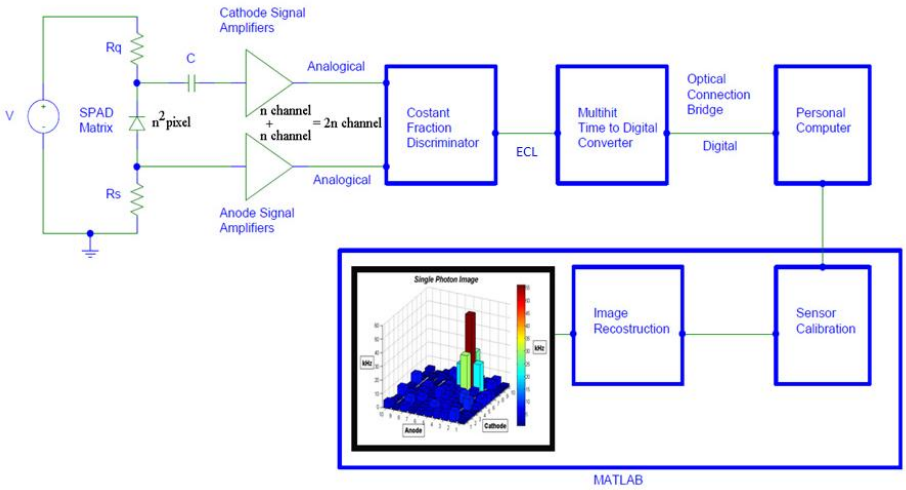

Figure 5-10: Signal acquisition chain.

5.5 Calibration Procedure and Imaging Reconstruction Technique

The crossing between cathode column signal and anode row signal is used to find the position of the arrival photon. The crucial point is the characterization of the correlation between the two signals produced by the same event. Starting from different electric cable length, different electrical processing between anode and cathode signals, different characteristic capacitance of the component used for each channel, there are many causes that produce different time shifts for the different channels mixing the arriving order of the two signals produced by each events. To reconstruct the right couple of anode and cathode signals generated by the same event we must know the right propagation delay of this two signals. This delay must be know with the maximum possible precision to distinguish from two following events, typical nanosecond precision or more. To achieve this requirement is necessary to measure the map of the delay along all the matrix diodes. Every time the sensor was used, because thermal fluctuation of the electrical component generate different time shift. We called this step “Sensor Calibration”. For that operation we decide to use the noise production,

because the events produced are distributed along the time with an appreciable time distant, the production rate satisfy the statistics needs in few minutes, but the most important reason is because do not show any spatial or time correlations. The only correlation we can find in the produced signal is the contemporary start of the two signals produced by the same avalanche. A code, developed in Matlab was done to map the correlation delay of the SPAD matrix output signals in a single software operation. The arriving time of the signals, coming from few minutes of noise, are collected. Starting for example from column 01 and the row 01, the delay between all the possible combinations of all the signals produced by this two channels is calculated. The histogram of this distribution show a correlation centered at 51.0 ns (Figure 5-11). For each of the hundred possible combinations of the ten row channels and the ten column channels an histogram was calculated and the centre and the width of the correlation were saved. The results, that we called sensor delay map, was shown in Figure 5-12.

This delay map is used for the imaging reconstruction software procedure during the sensor application measurement.

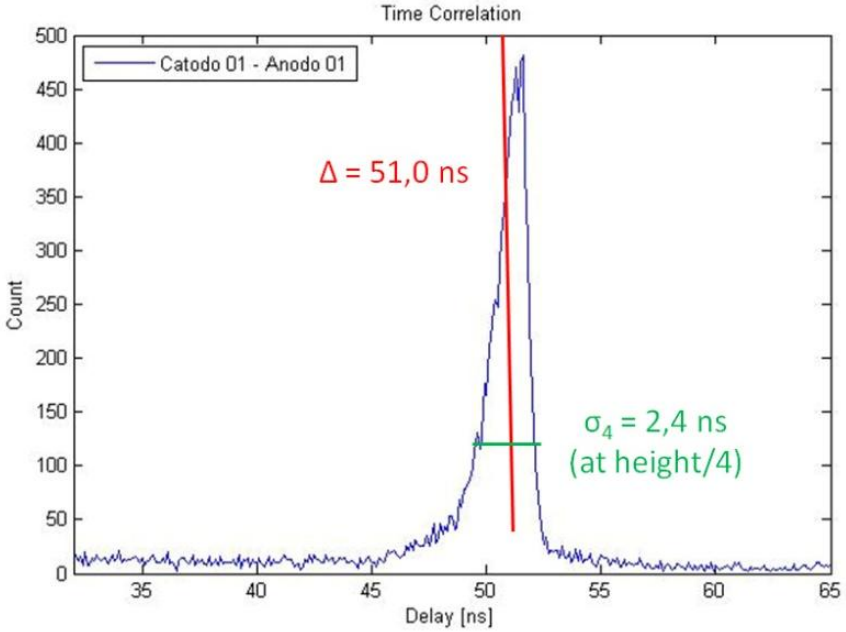

Figure 5-11: Correlation histogram between cathode 01 and anode 01.

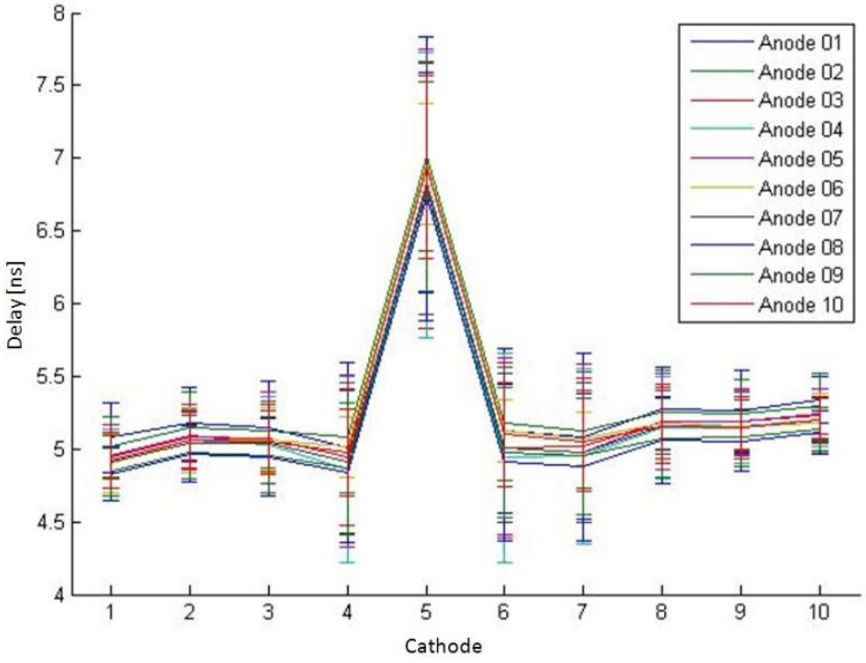

Figure 5-12: SPAD matrix delay map.

The code developed to bring out the Time Resolved Single Photon Image compares the time gap between all the possible combinations of all collected rows and columns signals with the delay map of the matrix to find the spatial positions of the true events. The time position of the true events were assumed equal to the arriving time of anodes signals, that show high time performance compared to the cathode readout system.

An example of the achievable images is the Figure 5-13 in which the subject is the head of a Light Emission Diode (LED). The image was done subtracting the dark count rate of each pixel, measured during the sensor calibration procedure. To maximize the image contrast we force to dark the color of pixels with a count rate less than 500 Hz.

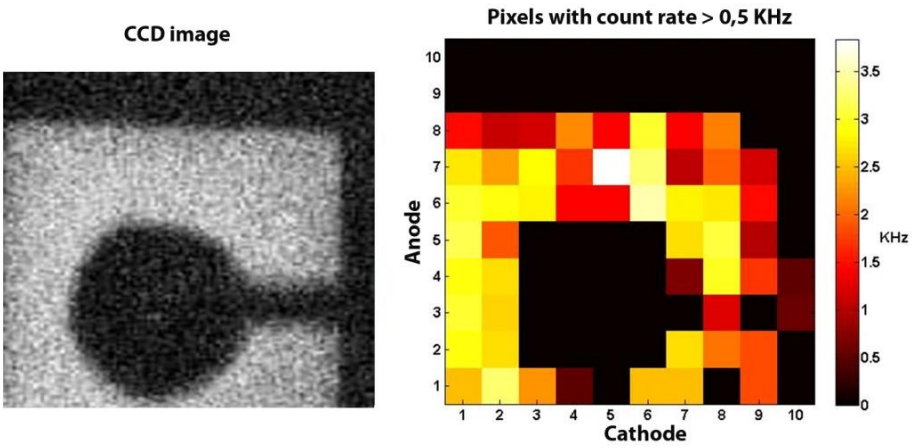

Figure 5-13: The subject of the Images is a LED head. Left: CCD image (640x480); Right: single photon time resolved image made with SPAD matrix sensor (10x10).

LED sources was chosen in this and in others tests because of the possibility to adjust the photon emission rate with fine precision limiting the current power source. With this regulation capability we were able to take a picture with a normal CCD camera at medium photon rate, and test the SPAD matrix capability in all the sensor dynamic range, from littlest measurable photon rate to the saturation level. We also achieve a modulated light source to test the time dependent characteristic of the device (section 4.4.2).

With our sensor and our imaging reconstruction technique we do not have the frame time limitations, like frame duration, frame rate, minimum time distance between frames. Every collected photons give his contribution to a continuous streaming of the photon source, the pictures can extracted putting together all the photons during a defined time, or can be collected in groups forming a sequence of video frames without any dark time between frames. The time and spatial positions of all detected photons are collected, and can be used for many correlation technique that use time and/or spatial correlation analysis. It is possible to see an example of video capability in the official home page of the Time Resolved Imaging Sensors of Laboratori Nazionali del Sud, at [40]. Inside this video there is an overview of our experimental setup and the time evolution sequence of the LED in the image of Figure 5-13 powered by a time dependent

source.

5.6 Coincidence

The main problem of our spatial recognition approach is the time coincidence between photons. The value that discern coincident events from distinct events is the error in the determination of the delay between anode and cathode signals of each pixel. For clarity reason we can examine a numerical example. Consider the arriving time of the four signals produced by two photons, for example the first photon produce the row signal in the channel 01 and the column signal in the channel 01, and the other photon produce signals in the row number 08 and in the column 05 (Table 5-1). Like in our real device, due to the columns and rows different signal processing, the delay for rows is less than for columns. The time precision with which is measured the arriving time of the signals (0,1 ns) is less than the error in the measurement of the correlation delay (about 2 ns).

Readout Channel	Arriving Time
Row 01	1200
Column 01	1700
Row 08	1240
Column 05	1710

Table 5-1

In the imaging reconstruction code we considered all the possible combination of this four signals (Table 5-2). With the values considered in the example the result is that only two couple are in accordance with the matrix delay map, so only this two positions are taken into account.

Row CH	Column CH	Measured Delay	True Delay	Delay Error	True or Not
01	01	500	510	12	True
01	05	510	475	25	Not
08	01	460	480	17	Not
08	05	470	485	20	True

Table 5-2

If we half the precision by which the delay map was measured all the four possible combinations of rows and columns are valid (Table 5-3), so we encounter a coincidence event. This time we can indifferently assume that the four signals are produced by two photons in the position (01, 01) and (08, 05), or in the others positions (01, 05) and (08, 01).

Row CH	Column CH	Measured Delay	True Delay	Delay Error	True or Not
01	01	500	510	24	True
01	05	510	475	50	True
08	01	460	480	34	True
08	05	470	485	40	True

Table 5-3

This example show how the time performance of our device is not only an application requirement that we want to satisfy, but is first of all the more important operational requirement of our readout sensor approach.

Taking into account this problem into the developing of the imaging reconstruction program, we can made different actions for the different situations. For example, if we are sure that the object picture show a circular symmetry we can decide, in the case of coincidence showed before, we can decide to preserve all four positions but each one with half weight. With this procedure the image is not damaged and the statistics do not lose this shots.

Inside the imaging reconstruction program we are able to control many events, choose what to do for each one, or simply made statistics of particular

situations. In addition to the coincidence events there is the possibility that a signal can be used in two spatial recognition events, what we call “multiple” event. This occurrence can be caused by two photons that arrive in coincidence along same row or same column.

In practice there are at list three other sources of coincident events, the optical cross correlation between diodes, the electrical influence between readout channel, and the possibility of a time coincidence between a pixel that generate a big amount of signals and an occasional event in another pixel. Therefore is very important to extract the statistics of such events.

To analyze of the matrix functionality to verify all our assumption we study a dedicated experimental setup. Into a black surface we built two holes. Behind that holes we put a dispersed LED with the light emission controlled by the applied power current. In Figure 5-14A we add another front side illumination source to better see the hole shape, Figure 5-14B is made with only the back side illumination, both of them are taken with a normal CCD camera (640x480). The image made with the SPAD matrix is reported in Figure 5-15.

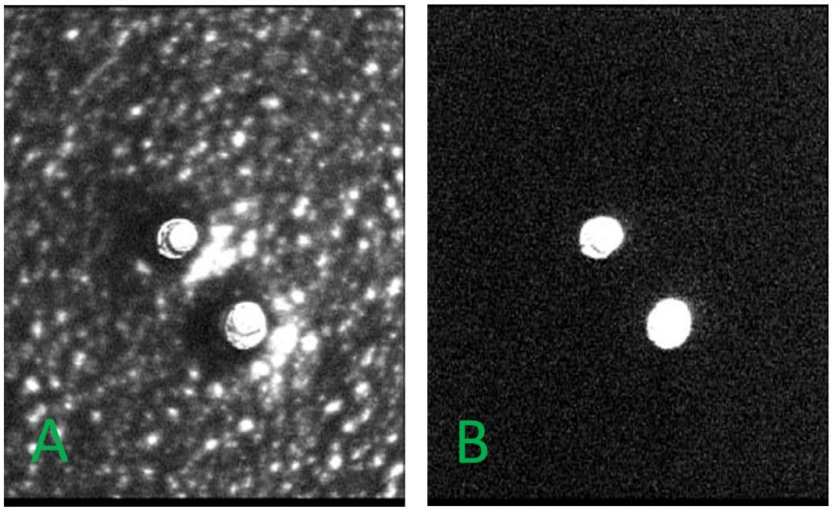

Figure 5-14: CCD image of two back lighten hole; A) with an additional front illumination to see the hole shape; B) with only the back side illumination.

Using the optics coupled with SPAD matrix we try to focus the two holes image to the littlest number of pixel. The result showed in Figure 5-15 is one

SPAD for the right spot and two SPAD for the left spot. As described above (section 5.4) in actual configuration there are ten quenching resistors, one for each column, so the dead time of the device is shared between along the SPADs of the same column, even if only one of the ten fires. So for our test is very important that the two SPADs enlighten by the left spot are in the same column because we can considered the cumulative behavior of the two diodes like the behavior of a single diode of a matrix with one integrated quenching resistor for each pixel. The Figure 5-15 shows pixels with a negative count rate, this is due to the dark count subtraction and to the sharing of the quenching resistors. The non enlightened diodes located in the same column of enlightened diodes are subjected to the dead time produced by the detected photons and are not able to produce their characteristics dark count rate, so the dark cont subtraction produce a negative value.

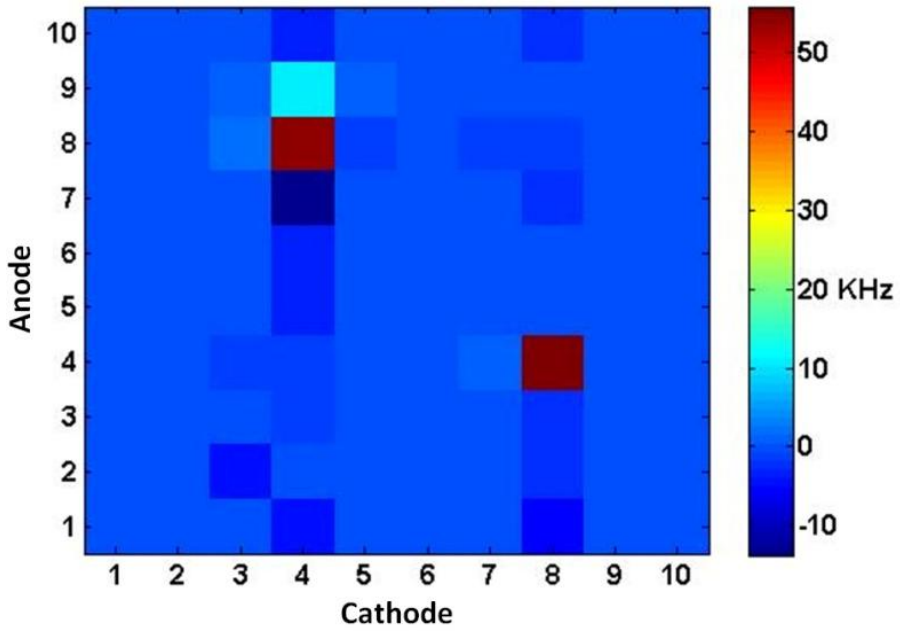

Figure 5-15: SPAD matrix image of the two back lighten hole.

As shown in Figure 5-16 the diodes object of interest are the true enlightened diodes of coordinate (9, 4) (8, 4) (4, 8) and the more probable diodes in which the coincidence must produce spurious events are (9, 8) (8, 8) (4, 4).

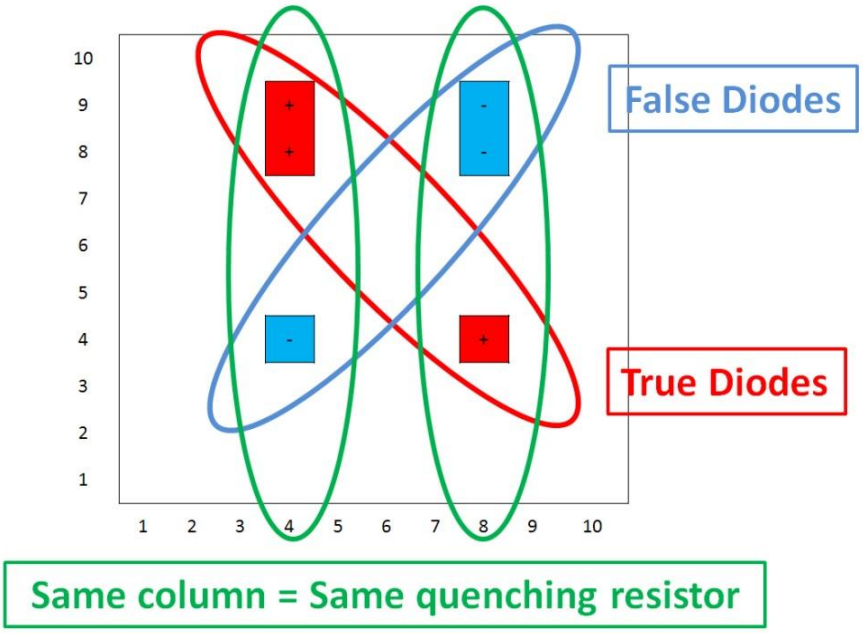

Figure 5-16: Grouping of the SPAD matrix diodes, true enlightened diodes, diodes under consideration for spurious events, diodes that share the same quenching resistor and consequently the same dead time.

The study was done at various LED power source value, to evaluate sensor behavior and the reconstruction algorithm performances along all the dynamic range of the sensor, and also in the saturation regime. With our software capability we extract three plot of three type of events, single events in which the time precision of the sensor is able to resolve the position without uncertainty (Figure 5-17), the multi events in which there is a row or a column signal that is shared for two events (Figure 5-18), and the coincidence events in which the uncertainty was founded (Figure 5-19). In the top part of the graphs there is a reminder of the color with which are addressed true enlightened diode (red) and false enlightened diode (blue). In the abscise there is reported the increase of power applied to the diode, that is proportional to the impinging photon flux. In the ordinate there are the measured events rate for the various pixels.

In the Figure 5-17 the first point is the measured dark rate, while the others points are calculated with the dark count subtraction. Pointed by the arrow there

is the high dark count rate of the pixel (9, 4). Following the output of this pixel versus the increase of photon flux it is possible to see the saturation effect, that at the end totally inhibit the signal production. So with the dark count subtraction the value measured at extreme saturation level is the inverse of the dark count rate. Like expected the three true enlightened diodes show a rapid increase of counts while the false diodes do not show any increase, on the contrary suffer of the saturation effect produced by the enlightened diodes, due to the shared resistors. Considering the total outgoing signal rate from each of the two quenching resistor, that means the two columns, we obtain a maximum measured rate of 70 Kcps. This maximum value is approximately equal between the two column and in accordance with what can be calculated with the Eq. 3-7. The powered LED point at which is reacted the maximum value depend on the relative source intensity of the two sources, due to a partial inhomogeneous illumination dispersion under the holes.

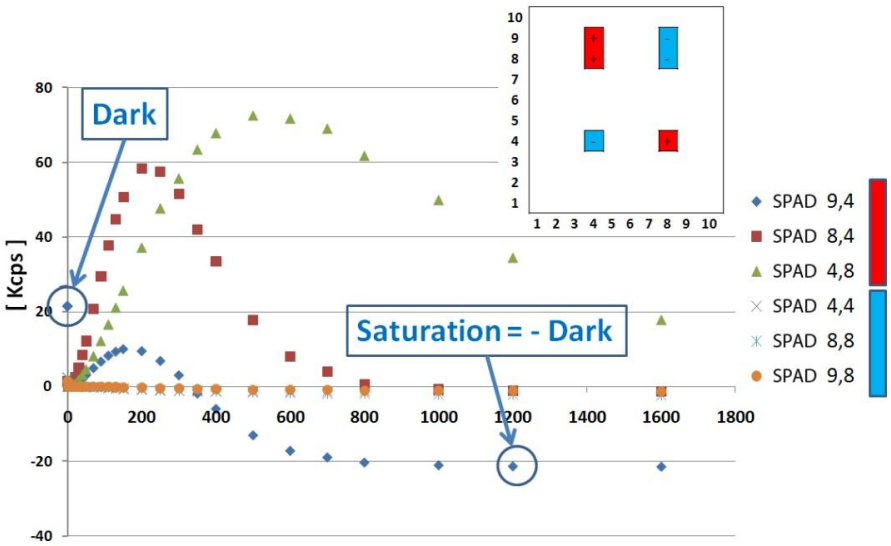

Figure 5-17: Pixel statistics of detected single events.

Figure 5-18 shows the statistics of the multiple events of the six diode under interest. Like predicted the occurrence of this event growth according to the primary single events measured by the enlightened diodes, but the maximum measured rate of this events is 0,36% of the maximum true rate of true events. The

three true enlightened diode show a maximum value four time greater than the others diodes, this is due to the high real rate produced by this pixel and the consequently highest probability to generate multi events.

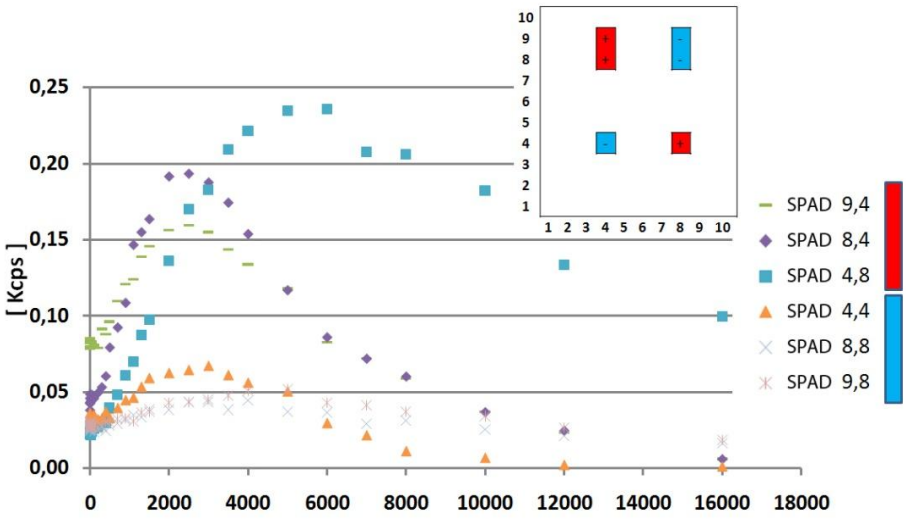

Figure 5-18: Pixel statistics of detected multi events.

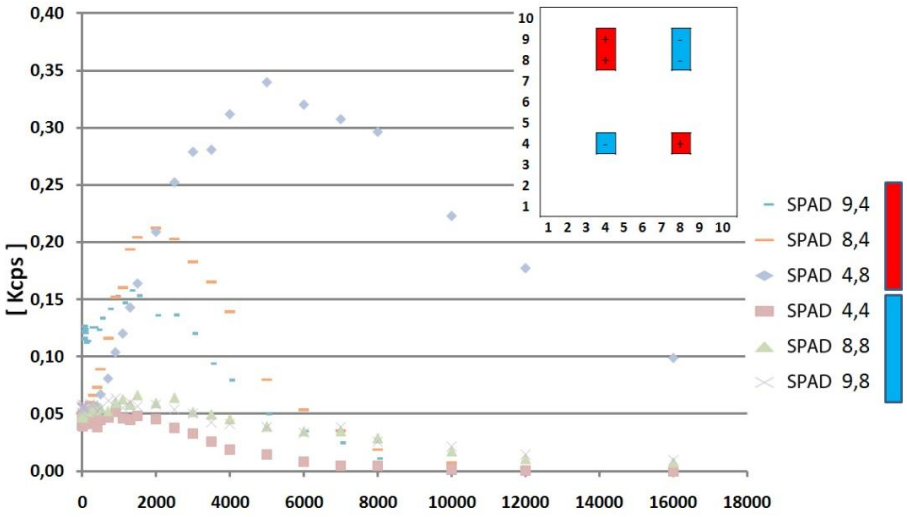

Figure 5-19: Pixel statistics of detected coincidence events.

In is important to stress that measured rate reported in Figure 5-17 and Figure 5-18 are due to event without any uncertainty, all that counts can be used for

the application analysis. Only the counts reported in Figure 5-19 represent ambiguous events which should be rejected. The occurrence of this ambiguous events are less than 0,5%.

The result of this analysis confirm our hypothesis and show how little are the amount of count that should be rejected. The image reconstruction does not suffer any statistic losses coming from the remote possibility of coincidence events. However we are always able to recognize and reject ambiguous event, and so, even if we use the device in further extreme environment, where a considerable probability of coincidence events occur, we are always able to neglect this contribute. Rejected event can be considered inside the group of photons that are not recognize because of the non perfect efficiency of the other components, like silicon PDE that is under 40% and fill factor that can't reach 100%.

5.7 Timing Performance and Matrix Design

What come out by the analysis done in this chapter is that the timing performance of all the sensor components are the main requirement for our imaging reconstruction algorithm. In principle there are not limitation in the use of our algorithm for very low photon flux. The lower is the impinging photon flux lower can be the detection time performance of the device. On the contrary, fixed the time performance of the device the maximum photon flux can be predicted. Now we want to examine all our results by the point of view of the timing performance, to predict the capability of future device.

In the analysis of the single SPAD two important thinks are emerged about timing performance, the time duration of the signal, predicted by the SPAD electrical simulation of chapter 2, and the dead time influence on the dynamic range of the device. The time duration of the produced signal is very important in our readout approach because the readout channel collect the signals of many diodes, all the SPADs of a row or a column, and we must avoid the detection loss due to a pileup event.

According to the results obtained in chapters 3 and 4 the single pixel dead

time became a very important parameter, because the dead time is able to inhibit the production of some signals but, using the time gap between produced signals it is possible to retrieve the information of photon losses. In our approach we read out of the matrix each produced signals, and a maximum acceptable output signal rate is our main limitation. The inhibited signals lowered the workload assigned to readout electronics, but the software data analysis take care to recover the right information without high computational performance requirements. AQC SPAD device, with a short dead time, and high rate capability are not suitable for our approach, because each pixel can produce a big amount of signals that can stress the readout matrix system. AQC SPAD device are used for imaging device but with a completely different readout strategy that do not perform such detailed transmission of each incoming photon information. With the PQC SPAD and the developed dead time compensation technique we react the same dynamic performance of active quenched system and do not overcome the readout possibility. The dead time limitation became a requirement for our matrix approach.

Choosing the dead time of the PQC SPAD device we select the maximum signal rate that each pixel can produce. This parameter must be chosen in accordance to the maximum workload allowed by the electronic readout system and to the maximum number of pixels in the matrix.

Another dead time that must be taken into account is the dead time of the constant fraction discriminator used in rows and columns readout. In the readout channel the arrival time of all signals must be know and any dead time correction can be adopted. Littlest is the dead time of this electronics device biggest can be the matrix signal production, and so the matrix size.

In this chapter we showed how important is the matrix delay map produced by the sensor calibration procedure. Highest is the time precision with which is reconstructed the position of impinging photons highest is the photon flux that can be collected by the matrix device. This timing features is given by the rising time constant and the jitter of the SPAD signals produced, and by the time precision of the readout channel used. In conclusion with our approach the better are the timing performance of the readout components the biggest can be the matrix

size.

Numerically speaking if T_1 is the dead time of the SPAD, T_n is the biggest value between the dead time of the readout channels and the length of the out coming signals, T_{nn} is the mean time accuracy of the system, and n is the maximum number of pixel for side of a square matrix, the littlest time performances needed to made a working SPAD matrix, that use our approach, must be in accordance with the relation:

$$1 \cdot T_1 \approx n \cdot T_n \approx n^2 \cdot T_{nn} \qquad 5\text{-}1$$

For a matrix of 10˙000 pixels and T_1 equal to 1 µs, equal to the dead time of the SPAD characterized in the chapter 3, T_n must be approximately 10 ns, and T_{nn} 0.1 ns. This solution require very high timing performances. To reduce the timing requirement, without decrease the performance, it is possible to double the number of channels, splitting the matrix in four littlest part of 50x50 elements, in such a way the T_n is doubled 20ns, and T_{nn} is quadrupled 0.4 ns. Requirements that are more near the actual commercial system capabilities. This is possible because the reading of the matrix is made at the end of a row or a column, so only two side of the matrix are needed to connect the pixel to the readout channel. Using all the side of a 100x100 matrix there is the place to put 400 electric contact for 400 readout channel, and the row and column contact can be organized like four matrix of 50x50 elements. With that numbers we obtain a 10˙000 pixel matrix able to count a maximum measurable flux of 10 mega photons per second per pixel, that means a total flux of 10^{11} photons per second.

5.8 Results

Time resolved single photon imaging sensor is a most interesting challenges of the future generation of imaging sensors. Actually two approach are distinguished CMOS and high performance SPAD fabrication process. CMOS approach use active quenching system, comparator, counter and storage of the number of counts per frame. This approach require a complex in situ electronics implementation with the consequent decreasing of fill factor and the further in-

creasing of the fabrication complexity. The arriving time information of each collected photon was relaxed to the time frame size, and matrix reading steps need an inactive time during which matrix sensibility is inhibited.

This work proof the functionality of cross reading applied to high performance SPAD technology to obtain a time resolved single photon imaging sensor. The approach is limited by the timing performance of the readout electronics and by the maximum number of pixel inside the matrix. However the timing performance of our approach is greater than CMOS approach and the absence of sensor inactive time completely distinguish this two approach for high sensibility time detection device.

Our feasibility study bring up the development of a new prototype device, in collaboration with the Bruno Kessler Foundation, which will be able to make new enhancement in photonic diagnostics.

Conclusions and Perspectives

The main achievement of this PhD work has been the project of a innovative sensor device, pursued by studying the needed elementary sensitive parts, by developing the two-dimensional configuration and the readout strategy, and by realizing a working prototype. This activity, complex and challenging not only has brought benefit to our professional experience but made us able to identify the peculiarities, the problems, and the possible improvements of the project. At the end of each developing step we founded confirmation of our assumption and unexpected results that exceeded expectations.

Studying the working principles of the SPAD device and its electrical characteristics we became able to design the double readout circuit needed for our "cross-wire" indexing strategy. To achieve this result it was very important to have understood the position of the SPAD stray capacitance and how it works for the signal production. Beyond the developing of anode and cathode reading we have designed a new multiple cathode readout circuit that enables a new readout strategy, that we named "binary indexing". While the contemporary reading of anode and cathode has been implemented in the final prototype the binary indexing will be a future test useful for passive and active quenched SPAD configuration.

The understanding of noise, afterpulse, and dead time influences on counting activity, and of their dependence on the incoming photon rate, made us able to extend of four order of magnitude the dynamic range of the passive quenched

SPAD device. Two order of magnitude were gained in the minimum measurable photon rate value, thanks to noise and afterpulse correction. Another two order of magnitude were gained in the maximum limit with a precise characterization of SPAD dead time type and its produced counting losses. The dead time correction was done also using one of the possible correlation analysis for which the device was designed. Using the Time Interval Density Distribution (TID) we were able to recognize if an output count rate value corresponds to a real value or if it is subject to saturation and must be corrected. The outstanding feature of this dead time analysis is to obtain, with simple passive quenched SPAD, the same performance reached by the active quenched one. The obtained circuital simplification makes competitive the fabrication strategy adopted by STMicroelectronics moving the complexity from the integrated circuit used in CMOS approach, to the acquisition software. This operation simplifies the sensor implementation, reduces the cost, increases the achievable fill factor, and reduces the time to market needed for the development of complex hardware. The software strategy becomes of large usability with the three new generalized equations developed for dead time losses and time dependent sources. Only thanks to such useful software analysis, the STMicroelectronics approach for Silicon Photon Multiplier can be used to develop Time Resolved Single Photon Image Sensor competitive with that obtained with CMOS technology. Beyond the benefit in our project the new developed dead time equations represent a step forward in the dead time correction for all counting devices subject to any dead time type and we expect that this correction approach will be largely used.

The final manufacturing step was to perform a working prototype, with two-dimensional SPAD array device, readout and amplification stage for anode and cathode signal, electronic acquisition chain with constant fraction discriminator and time to digital converter, and interfacing with personal computer. Cross wire readout configuration requires the developing of code for the sensor calibration procedure and an imaging reconstruction algorithm. Many tests have been done with the prototype pointing the crucial aspect of the device performances. First of all an extremely intensive test has been done for the coincidence events that can destroy the cross wire readout strategy. The result was that with our ap-

proach the coincidence problem was completely under control because of the high time performance of the device and because of the peculiarities developed in the imaging reconstruction code, that recognize and neglect faulty event. Taking the sum of all the manufacturing and electrical characteristics studied and weighing the timing performance requirement, we have numerically defined the relations between the performance needed for a specific application and the manufacturing properties of future sensors, such as the maximum number of elements per array, maximum duration of produced signals, time recognition performances, electronics readout bandwidth. With prototype tests we also showed the main feature that marks the difference between our imaging approach and the other SPAD imaging concurrent approaches, that is we were able to obtain from the sensor the arrival time information of each impinging photon without storing data into pixels and without being necessary a sensor readout step. These features make we able to increase the time accuracy of the sensor and to enable a continuous sensor reading process without sensor blind time.

During this three years project we presented our work as oral reports at five international conferences, while the results have been published in six papers on journal. In the meanwhile we also were selected as referee for three international journals.

The obtained results have been also considered of interest of the INFN, so that the V Commission of INFN funded a new project named Time Resolved Imaging Sensor (TRIS)[41] for the development of a large imaging sensor based on the experience achieved in the realization of the prototype sensor. We also extended our collaboration to the Foundation Bruno Kessler with which we have planned the manufacturing of new time resolved single photon imaging sensors.

Bibliography

[1] "Time-domain fluorescence lifetime imaging applied to biological tissue", D.Elson, J.R.Isidro, I.Munro, F.Reavell, J.Siegel, K.Suhling, P.Tadrous, R.Benninger, P.Lanigan, J.McGinty, C.Talbot, B.Treanor, S.Webb, A.Sandison, A.Wallace, D.Davis, J.Lever, M.Neil, D.Phillips, G.Stamp, P.French, Photochem. Photobiol. Sci., vol 3, 795-801 (2004)

[2] "The bh TCSPC Handbook", Third Edition, W.Becker, Becker & Hickl GmbH, (2008)

[3] "Laser light scattering", C.S.Jhonson, D.A.Gabriel, Dover Publications, INC.New York (1981)

[4] "Dynamic Light Scattering", B.Berne, R.Pecora, Dover Pubblication, INC. New York (1976- 2001)

[5] "Toward a 3-D Camera Based on Single Photon Avalanche Diodes", C.Niclass, A.Rochas, P.A.Besse, E.Charbon, IEEE J. OF SELEC. TOP. IN QUAN. EL., VOL. 10, NO. 4 (2004)

[6] "Visualization and PIV Measurements of High-Speed Flows and Other Phenomena with Novel Ultra-High-Speed CCD Camera", S. Eisenberg et al., Proc. of SPIE, Vol. 4948, pp. 671-676 (2002)

[7] "Introduction to Adaptive Optics and its History", M.Claire, Proc. of American Astronomical Society 197th Meeting

[8] "Single-photon avalanche photodiodes with integrated quenching resistor", M.Mazzillo, G.Condorelli, A.Piazza, D.Sanfilippo, G.Valvo, B.Carbone, G.Fallica, S.Billotta, M.Belluso, G.Bonanno, A.Pappalardo, L.Cosentino, P.Finocchiaro, Nucl. Instr. and Meth. A, vol. 591, 367-373 (2008)

[9] "Generalization of DT Equations for Time Dependent Sources", L.Neri, S.Tudisco, F.Musumeci, A.Scordino, G.Fallica, M.Mazzillo, M.Zimbone, Sensors, Issue "10 Years Sensors - A Decade of Publishing" doi:10.3390/s101210828, (2010)

[10] “A New Generation of SPAD Single Photon Avalanche Diodes”, S.Tudisco, F.Musumeci, L.Lanzanò, A.Scordino, S.Privitera, A.Campisi, L.Cosentino, G.Condorelli, P.Finocchiaro, G.Fallica, S.Lombardo, M.Mazzillo, D.Sanfilippo, E.Sciacca, IEEE Sensors Journal, vol. 8, n. 7, 1324 (2008).

[11] "A silicon avalanche photodiode for single optical photon counting in the Geiger mode", W.J.Kindt, N.H.Shahrjerdy, H.W.Zeijl, Sensors and Actuators A, vol 60, 98-102(1997)

[12] “Avalanche photodiodes and quenching circuits for single-photon detection”, S.Cova, M.Ghioni, A.Lacaita, C.Samori, F.Zappa, Applied Optics, vol. 35, n. 12, 1956 (1996).

[13] "A Fast Active Quenching and Recharging Circuit for Single-Photon Avalanche diodes", R.Mita, G.Palumbo, G.Fallica, proc. of Circuit Theory and Design, vol 3, 1-2 (2005)

[14] "Reduce Afterpulsing of Single Photon Avalanche Diodes Using Passive Quenching With Active Reset", M.Liu, C.Hu, J.C.Campbell, Z.Pan, M.M.Tashima, IEEE J. of Quant. El., vol 44, n 5, 430 (2008)

[15] "Afterpulsing in Geiger-mode avalanche photodiodes for 1.06 μm wavelength", K.E.Jensen, P.I.Hopman, E.K.Duerr, E.A.Dauler, J.P.Donnelly, S.H.Groves, L.J.Mahoney, K.A.McIntosh, K.M.Molvar, A.Napoleone, D.C.Oakley, S.Verghese, C.J.Vineis, R.D.Younger, Appl. Phys. Lett. 88, 133503 (2006)

[16] "A process and deep level evaluation tool: afterpulsing in avalanche junctions", A.C.Giudice, M.Ghioni, S.Cova, F.Zappa, proc. of European Solid-State Device Research, 347-350 (2003)

[17] "Silicon Photomultiplier Technology at STMicroelectronics", M.Mazzillo, G.Condorelli, D.Sanfilippo, G.Valvo, B.Carbone, G.Fallica, S.Billotta, M.Belluso, G.Bonanno, L.Cosentino, A.Pappalardo, P.Finocchiaro, IEEE Trans. on Nucl. Sci., vol 56, n 4, 2434 (2009)

[18] "Performance study of silicon photomultipliers as photondetectors for PET", R.Verheyden, H.Chagani, R.Dolenec, R.Pestotnik, P.Krizan, S.Korpar, A.Stanovnik, Nucl. Instr. and Meth. A (2010)

[19] "Optical crosstalk in single photon avalanche diode arrays: a new complete model", I.Rech, A.Ingargiola, R.Spinelli, I.Labanca, S.Marangoni, M.Ghioni, S.Cova, Optics Express, Vol.16 N.12 (2008)

[20] http://www.cadence.com/products/orcad/pages/default.aspx

[21] "Design and characterization of single photon avalanche diodes arrays", L.Neri, S.Tudisco, L.Lanzanò, F.Musumeci, S.Privitera, A.Scordino, G.Condorelli, G.Fallica, M.Mazzillo, D.Sanfilippo, G.Valvo, Nucl. Instr. and Meth. A, vol 617, 432-433 (2010)

[22] "SPID: Single Photon Imaging Device", L.Neri, S.Tudisco, L.Lanzanò, F.Musumeci, S.Privitera, A.Scordino, G.Condorelli, G.Fallica, M.Mazzillo, D.Sanfilippo, G.Valvo, Proceeding of SPIE, vol. 7021, 702129 (2008).

[23] "Bi-dimensional arrays of SPAD for time-resolved single photon imaging", S.Tudisco, L.Lanzanò, F.Musumeci, L.Neri, S.Privitera, A.Scordino, G.Condorelli, G.Fallica, M.Mazzillo, D.Sanfilippo, G.Valvo, Nuclear Instruments and Methods in Physics Research A, vol. 610, issue 1, 138 (2009).

[24] "Single Photon Avalanche Diodes: towards the large bidimensional arrays", S.Privitera, S.Tudisco, L.Lanzanò, F.Musumeci, A.Pluchino, A.Scordino, A.Campisi, L.Cosentino, P.Finocchiaro, G.Condorelli, M.Mazzillo, S.Lombardo, E.Sciacca, Sensors, vol. 8, 4636 (2008).

[25] INFN GRID https://grid.infn.it/

[26] INFN GRID Catania http://grid.ct.infn.it/

[27] "Radiation detection and measurements" second edition (1989), G.F.Knoll.

[28] "Bibliography on dead time effects", J.W.Muller, Report BIPM-81/11 (1981).

[29] "Generalized dead times", J.W.Muller, Nuclear Instruments and Methods in Physics Research A, vol. 301, 543 (1991).

[30] "Non-Poisson counting statistics of a hybrid G-M counter dead time model", S.H.Lee, M.Jae, R.P.Gadner, Nuclear Instruments and Methods in Physics Research B, vol. 263, 46 (2007).

[31] "A new G-M counter dead time model", S. H. Lee, R. P. Gardner, Applied Radiation and Isotopes, vol. 53, 731-737 (2000).

[32] "On the effect of two extended dead times in series", J.W.Muller, Report

BIPM-72/9 (1972).

[33] "Counting statistics distorted by two dead times in series which end with an extended type dead time", H.D.Choi, Nuclear Instruments and Methods in Physics Research A, vol. 599, 251 (2009).

[34] "Deadtime correction in counting rapidly decaying sources", K.G.A.Porges, A. de Volpi, International Journal of Applied Radiation and Isotopes, vol. 22, 581 (1971).

[35] "Decay effects with a generalized dead time", J.W.Muller, Rapport BIPM-88/11 (1988).

[36] "Automatic compensation of dead time effects", Y.Kawada, S.Kobayashi, K.Watanabe, T.Kawamura, Y.Hino, Applied Radiation and Isotopes, vol. 49, n. 9-11, 1123 (1998).

[37] "Dead time causes and correction method for single photon avalanche diode devices", L.neri, S.Tudisco, F.Musumeci, A.Scordino, G.Fallica, M.Mazzillo, M.Zimbone, Review of Scientific Instruments, vol. 81, Issue 8, 086102 (2010).

[38] "Dead time of single photon avalanche diodes", L.neri, S.Tudisco, F.Musumeci, A.Scordino, G.Fallica, M.Mazzillo, M.Zimbone, Nuclear Physics B (proc. suppl.).

[39] "Arrays of Geiger mode avalanche photodiodes", E.Sciacca, S.Lombardo, M.Mazzillo, G.Condorelli, D.Sanfilippo, A.Contissa, M.Belluso, F.Torrisi, S.Billotta, A.Campisi, L.Cosentino, A.Piazza, G.Fallica, P.Finocchiaro, F.Musumeci, S.Privitera, S.Tudisco, G.Bonanno, E.Rimini, IEEE Photonics Technology Letters, vol. 18, 1633-1635 (2006).

[40] http://www.lns.infn.it/index.php?option=com_content&view=article&id=381&catid=138&Itemid=116

[41] http://www.infn.it/csn5/docs/esperim_11.html

Acknowledgements

In primo luogo devo ringraziare la mia famiglia tutta per il supporto la fiducia e lo sprono che mi hanno dato durante tutto il mio corso di studi. Un grazie speciale va a mia moglie Valeria che mi ha donato mio figlio Alessio, ed ad Alessio che ad ogni mio ritorno a casa è stato in grado di farmi dimenticare ogni stanchezza. Grazie ai miei genitori ed a mio fratello che credono in me più di quanto io meriti, ai genitori di Valeria ed alle mie nonne che mi vogliono bene come un figlio, ed a Marco che non mi ha mai fatto mancare il suo affetto fraterno.

In un periodo in cui il dottorato e la carriera da ricercatore sembrano valere sempre meno devo ringraziare tutto il gruppo di ricerca del prof. Francesco Musumeci ed il reparto R&D del dott. Giorgio Fallica che hanno reso importante ogni sforzo intrapreso e sono stati riferimento per credere in quello che faccio. Un grazie particolare va al prof. Musumeci ed alla prof.ssa Scordino le cui professionalità mi sono servite da esempio e che, con la loro preparazione e disponibilità, non mi hanno mai fatto mancare tutto ciò di cui ho avuto bisogno. Grazie al dott. Salvo Tudisco che ha creduto in me e mi ha mostrato i tanti aspetti del mestiere del ricercatore. Grazie al dott. Fallica e al dott. Massimo Mazzilo che sono stati sempre fonte di sapere e sprono inventivo. Ringrazio il prof. Lattuada e tutto lo staff dei Laboratori Nazionali del Sud che mi hanno messo a disposizione le risorse umane e logistiche indispensabili per un lavoro di ricerca di alto livello.

La qualità del lavoro svolto è però anche frutto della qualità della vita trascorsa all'interno dei Laboratori Nazionali del Sud. Grazie a tutto l'Allegra Cafè

Social Club, per lo svago, il divertimento ed anche le riflessioni che in ogni pausa, pranzo, o chat avete animato. Mi auguro e vi auguro di non perdere mai la voglia di donare amicizia, sostegno e divertimento.